UC San Diego
UC San Diego Electronic Theses and Dissertations

Title
Tailoring Nanoscale Properties to Enable Advanced Energy Storage Materials

Permalink
https://escholarship.org/uc/item/14t9h52r

Author
Verde, Michael

Publication Date
2015

Peer reviewed|Thesis/dissertation

UNIVERSITY OF CALIFORNIA, SAN DIEGO

Tailoring Nanoscale Properties to Enable Advanced Energy Storage Materials

A dissertation submitted in partial satisfaction of the
requirements for the degree Doctor of Philosophy

in

NanoEngineering

by

Michael Gabriel Verde

Committee in charge:

      Professor Ying Shirley Meng, Chair
      Professor Seth Cohen
      Professor Eric Fullerton
      Professor Oleg Shpyrko
      Professor Jan Talbot

2015

The Dissertation of Michael Gabriel Verde is approved, and it is acceptable in quality and form for publication on microfilm and electronically:

_____

_____

_____

_____
Chair

University of California, San Diego

2015

DEDICATION

To my mother,

for her unending support and compassion

EPIGRAPH

It is important that students bring a certain ragamuffin, barefoot irreverence to

their studies; they are not here to worship what is known, but to question it.

- Jacob Bronowski

TABLE OF CONTENTS

LIST OF ABBREVIATIONS

AFM	Atomic Force Microscopy
c-AFM	Conductive Atomic Force Microscopy
CCP	Carbonate Co-Precipitation
EIA	United States Energy Information Administration
ESS	Energy Storage System
EV	Electric Vehicle
EXAFS	Extended X-ray Absorption Fine Structure
GIXRD	Grazing Incidence X-ray Diffraction
HCP	Hydroxide Co-Precipitation
ICP-OES	Inductively Coupled Plasma – Optical Emission Spectroscopy
ICP-MS	Inductively Coupled Plasma – Mass Spectrometry
OER	Oxygen Evolution Reaction
SEI	Solid Electrolyte Interface
SEM	Scanning Electron Microscopy
SG	Sol-Gel
SPM	Scanning Probe Microscopy
SHE	Standard Hydrogen Electrode
SLFB	Soluble Lead Flow Battery
XAFS	X-ray Absorption Fine Structure
XAS	X-ray Absorption Spectroscopy
XPS	X-ray Photoelectron Spectroscopy

XRD   X-ray Diffraction

LIST OF FIGURES

LIST OF TABLES

ACKNOWLEDGEMENTS

Chapter 3, in full, is a reprint of the article, "Effect of Morphology and Manganese Valence on the Voltage Fade and Capacity Retention of Li[Li$_{2/12}$Ni$_{3/12}$Mn$_{7/12}$]O$_2$," as it appears in ACS Applied Materials & Interfaces, Verde, M. G.; Liu, H.; Carroll, K. J.; Baggetto, L.; Veith, G. M.; Meng, Y. S., 2014, 6 (21), 18868-18877. The dissertation author was the primary investigator and author of this paper.

Chapter 4, in full, is a reprint of the article, "Elucidating the Phase Transformation of Li$_4$Ti$_5$O$_{12}$ Anode at the Nanoscale Using c-AFM," which is in preparation for submission. The dissertation author was the primary investigator and author of this paper.

VITA

2015   Ph.D. in NanoEngineering, University of California, San Diego

2013   M.S. in NanoEngineering, University of California, San Diego

2010   B.S. in Chemistry, University of New England, Biddeford

PUBLICATIONS

Verde, M.G.; Baggetto, L; Wisinger, N.; Veith, G.M.; Seo, J.K.; Wang, Z.; Meng, Y.S.; Elucidating the Phase Transformation of $Li_4Ti_5O_{12}$ Lithiation at the Nanoscale Using c-AFM. In preparation.

Verde, M.G.; Carroll, K.J.; Meyer III, H.M.; Nguyen, H.; Tang, M.T.; Meng, Y.S. Elucidating Major Side Reactions in Soluble Lead Flow Batteries. In Preparation.

Liu, H.; Qian, D.; **Verde, M. G.;** Zhang, M.; Baggetto, L. c.; An, K.; Chen, Y.; Carroll, K. J.; Lau, D.; Chi, M.; Veith, G. M.; Meng, Y. S. Understanding the Role of NH_4F and Al_2O_3 Surface Co-modification on Lithium-Excess Layered Oxide $Li_{1.2}Ni_{0.2}Mn_{0.6}O_2$. *ACS Appl. Mater. Interfaces* **2015**.

Zhang, Q.; **Verde, M. G**.; Seo, J. K.; Li, X.; Meng, Y. S. Structural and electrochemical properties of Gd-doped $Li_4Ti_5O_{12}$ as anode material with improved rate capability for lithium-ion batteries. *J. Power Sources* **2015,** *280* (0), 355-362.

Verde, M. G.; Liu, H.; Carroll, K. J.; Baggetto, L.; Veith, G. M.; Meng, Y. S. Effect of Morphology and Manganese Valence on the Voltage Fade and Capacity Retention of Li $Li_{2/12}Ni_{3/12}Mn_{7/12}O_2$. *ACS Appl. Mater. Interfaces* **2014,** *6* (21), 18868-18877.

Verde, M. G.; Carroll, K. J.; Wang, Z.; Sathrum, A.; Meng, Y. S. Achieving high efficiency and cyclability in inexpensive soluble lead flow batteries. *Energy Environ. Sci.* **2013,** *6* (5), 1573-1581.

Bozeman, T. C.; Edwards, K. A.; Fecteau, K. M.; **Verde, M. G**.; Blanchard, A.; Woodall, D. L.; Benfaremo, N.; Ford, J. R.; Mullin, J. L.; Prudente, C. K.; Tracy, H. J. Tolyl-Substituted Siloles: Synthesis, Substituent Effects, and Aggregation-Induced Emission. *J. Inorg. Organomet. Polym. Mater.* **2011,** *21* (2), 316-326.

ABSTRACT OF THE DISSERTATION

Tailoring Nanoscale Properties to Enable Advanced Energy Storage Materials

by

Michael Gabriel Verde

Doctor of Philosophy in NanoEngineering

University of California, San Diego, 2015

Professor Ying Shirley Meng, Chair

The work described herein revolves around two main themes. The first is the object of study – batteries. Diverse forms of energy storage continue to evolve as humans aim to maximize convenience, efficiency, and sustainability in the progress of modern society. Batteries in particular have become entrenched in our day-to-day lives due to the proliferation of mobile electronics. The array of potential battery applications, such as backup power, electric vehicles, and smart-grids, however, has lead to the development

of many different chemistries and systems, all of which involve highly distinct phenomena. This thesis provides an in-depth analysis of two such systems – the lithium-ion battery and the soluble lead flow battery – to highlight the difficulties in choosing one technology for all energy storage needs.

The second theme aims to challenge the gratuitously positive public perception of nanotechnology. An explosion in nanoscience as a distinct field or focus of study has occurred with the turn of the century. Many major research institutes now boast having a department or center dedicated to the topic. Reputable publishers have created high-impact journals around the theme. Conferences and funding organizations aim to specifically attract scientists contributing towards the subject. Prior to the 21st century, however, the buzz around *nano* hardly existed. Searching Thomson Reuters' Web of Science for titles using the word *nano*, during the entire 20th century, leads to only a few thousand results. In the first fifteen years since, the same search criteria leads to an increase of two orders of magnitude more results.

The high profile garnered by nano-related themes has in large part taken root because of the general assumption that untapped and advantageous properties exist at the nanoscale. Such properties are relatively overgeneralized, however, and are typically only presented in benefiting light. In the case of batteries, the specific nanoscale phenomena occurring in each system are distinct; what may be desirable in one electrochemical environment may be undesirable in another. This thesis aims to carefully identify and characterize the nanoscale processes occurring in the batteries described, to contribute more science and less hype to the budding field of nanoscience.

Chapter 1

Introduction

1.1 Energy consumption

As the human population continues to balloon, finding ways to sustainably harvest and distribute the resources of this planet has become a paramount issue. Resources able to provide us with energy are particularly important, as it has been suggested that the quality of one's life and evolution of culture in general is directly proportional to the degree of energy consumption.[1] The desire for and importance of energy to our growth has been manifest by the rapid rise in global energy consumption. This rate has even exceeded our population growth in the last fifty years.[2] Furthermore, its pace is set to quicken, as the U.S. Energy Information Administration (EIA) predicts that it will increase an additional 56% by 2040.[3] The sheer magnitude of consumption is staggering. In 2012, 153.6 petawatt-hours were consumed globally.[4] The US alone consumed 18.1% of that total.

Figure 1.1 depicts how the U.S. uses that energy, as categorized by source and end-use sector. Only 8.1% of this total is generated from renewable sources, such as wind and solar. None are utilized by the country's second largest sector, transportation, which consumes 27% of our total. The abundance of petroleum, natural gas, and coal are limited. Though technological advancements such as fracking may delay Marion King Hubbart's original Peak Oil predictions, the abundance of these resources are clearly

waning.[5] In addition, their use leads to forms of pollution, such as CO_2, that may accelerate global warming. There is great incentive, therefore, to make use of sustainable energy storage systems (ESS) in the transportation industry.

To effectively do so, potential ESSs need to be comprised of inexpensive and abundant materials – preferably those that can be recycled.[6] They also need to compete with the energy density of petroleum, which cannot currently be achieved.[7] Lastly, a renewable energy infrastructure needs to be implemented in the electric power sector, to sustainably charge ESSs used in transportation. This more so enhances the demand for ESSs, as they are necessary to optimize the use of intermittent sources such as wind and solar on the electric grid.[8] Because the functions of ESSs performing on the grid are very different than those in an automobile, the ESSs ideal for each sector may not be the same.
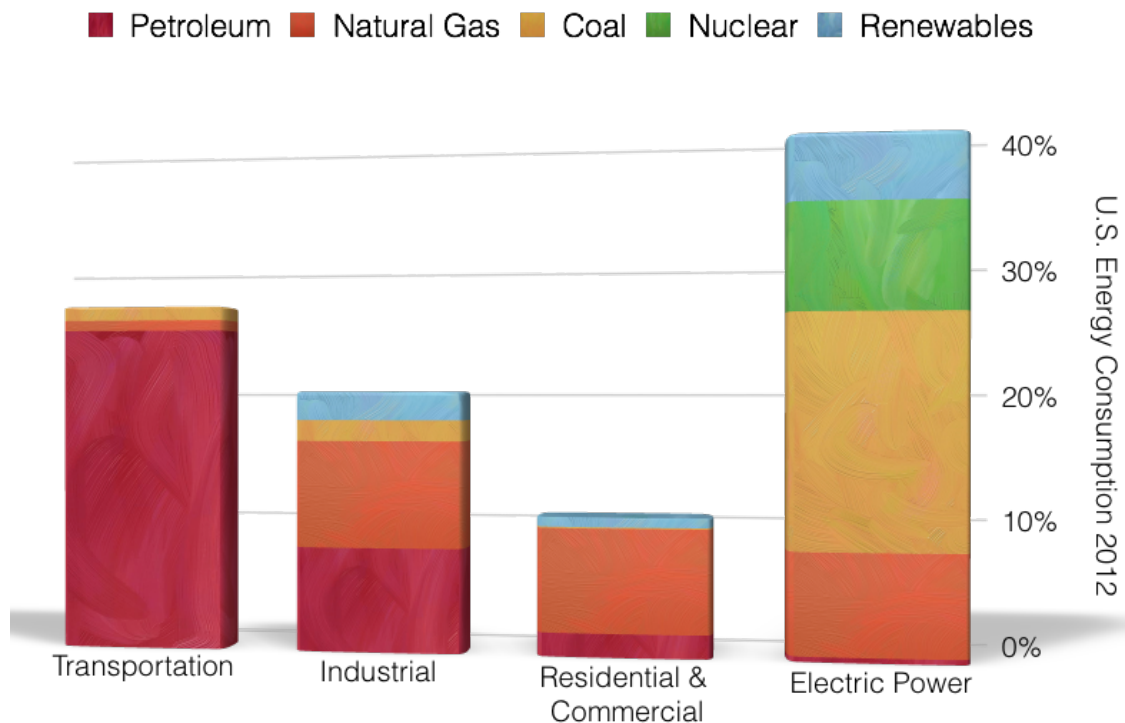
Figure 1.1 U.S. energy consumption in 2012 categorized by end-use sector.

1.2 Energy storage systems

There exist a wide array of ESSs proposed for use in energy applications. For use in electric vehicles (EVs), a primary criterion for the ESS is to possess very high energy density. The theoretical energy density of gasoline is 13 kWh·kg^{-1}. Due to tank-to-wheel efficiency of about 12.6%, however, the useable or practical energy density of gasoline is closer to 1.7 kWh·kg^{-1}.[9] Despite the inefficiency, no ESS can currently match this. Supercapacitors can reach competitive power densities, upwards of 10^4 W·kg^{-1}, but cannot deliver the energy for an extended period of time.[10] Batteries cannot match the power of supercapacitors, but reach more comparable energy densities. Electric propulsion systems for EVs are able to achieve 90% efficiency, however, state of the art commercially available batteries still only exhibit energy densities of 150-200 Wh·kg^{-1}.[11] For these reason, research has been heavily dedicated towards finding materials that enable higher power and higher energy density batteries.[12] Furthermore, research dedicated towards improving the cost and safety of high energy density batteries is also being hotly pursued.[13]

For grid applications, the energy density of an ESS is considerably less critical. It does not need to be mobile or located in a populated area, so its weight and volume are relatively trivial. The applications for an ESS on the grid is to assist in operations such as electric energy time-shift, area regulation, congestion relief, demand charge management, fast ramping, and frequency regulation. Since it may be used to perform a number of distinct functions, its durability and flexibility in design and operation are more essential. A number of technologies have been proposed, such as flywheels, supercapacitors,

compressed air, and hydrogen – each having their own advantages and disadvantages.[14-16] None are as quite as flexible, however, as flow batteries.[17]

Flow batteries are unique because they share characteristics of both conventional batteries and fuel cells. Figure 1.2 demonstrates the defining difference between each electrochemical system. The electrodes themselves compose the electroactive species of a conventional battery. Ions formed during redox diffuse into the electrolyte to maintain charge balance, but those ions do not have to be the oxidized (O) or reduced (R) species. In an MnO_2 electrode, for example, Mn^{4+} is the redox active species being reduced, and hydrogen ions (H^+) diffuse into the structure upon discharge, to form MnOOH during the single electron process.[18] A fuel cell, on the other hand, makes use of an electrode as current collector only. The oxidized (O) and reduced (R) species are flowed across the electrodes, which serve as a substrate for the redox reaction to occur. The system is typically open, as the redox species are often not reversible, and are composed of gaseous elements such as hydrogen (H_2) and oxygen (O_2). In addition, the electrodes often contain catalysts to lower the activation barrier of the redox reactions.[19] The redox active species of a flow battery are also not housed within the electrode. They exclusively exist in the electrolyte. To overcome diffusion limiting phenomena, they must be continuously flowed across the electrodes to undergo redox. They do not leave the system, however, as they are stored in tanks, which comprise the flow battery system. This effectively separates energy (electrolyte) and power (electrodes) components to provide flexibility in design. The energy densities of these systems are inherently low, but their cost and durability are quite high.

5
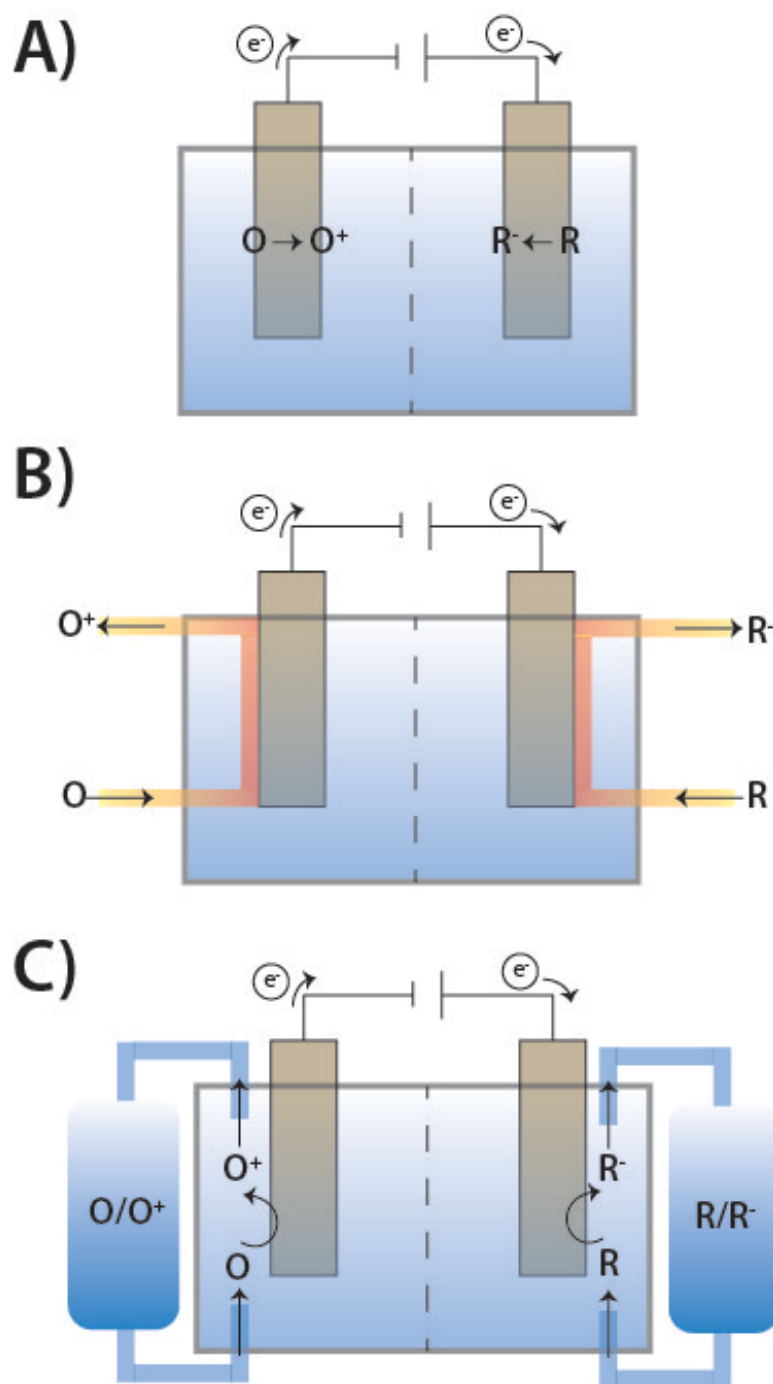
Figure 1.2 Schematic differentiating the basic principle between A) a conventional battery, B) a fuel cell, and C) a flow battery.

1.3 Lithium-ion batteries

The lithium-ion (Li-ion) battery was first proposed in the 1970's, by Stanley Whittingham, but did not achieve the high energy density it is known for today until John Goodenough introduced the $LiCoO_2$ cathode in 1980.[20] The incorporation of graphitic anode by Akira Yoshino in 1985 was the next major milestone in the development of the modern day Li-ion battery.[21] Though lithium metal would be the ideal anode candidate in terms of energy density, exhibiting a specific capacity of 3.86 Ah·g^{-1} and low working voltage of -3.01 V vs SHE, the formation of dendrites creates a serious shorting hazard.[22] The electrodes and specific reactions occurring within Li-ion batteries can be extremely diverse. What they all have in common, however, is that lithium ions (Li^+) diffuse out of the cathode and into the anode upon charge, and back out of the anode and into the cathode upon discharge. Figure 1.3 illustrates this general working principle.

Most commercially available Li-ion batteries make use of intercalation electrodes. For these materials, Li^+ intercalates into and out of a host structure, without drastic reorganization of the original bonding framework. For example, the cathode shown in Figure 1.3 depicts Li^+ layers separated by transition metal ion layers, propagating along the c-axis. Upon cycling, Li^+ diffuses into and out of the 2D layered arrangement along the a-b plane. Carbonate-based electrolytes containing $LiPF_6$ salt are commonly used as electrolyte, as they provide the best combination of desirable properties – namely, a high dielectric constant, low viscosity, a relatively wide temperature range, and a wide electrochemical window.[23] Essentially no electrolyte is fully stable at the high operating voltages of Li-ion batteries, but their continued operation is made possible by the formation of stable solid-electrolyte interface (SEI) layers at the boundary of each

electrode and electrolyte.[24] To highlight the fact that Li^+ may undergo 1D, 2D, and even 3D diffusion through an electrode host structure, the anode shown in Figure 1.3 represents $Li_4Ti_5O_{12}$ spinel, which undergoes 3D diffusion. The cathode is based upon the hexagonal $Li[Li_{2/12}Ni_{3/12}Mn_{7/12}]O_2$ structure. Both of these compounds are discussed in greater detail later in this thesis.
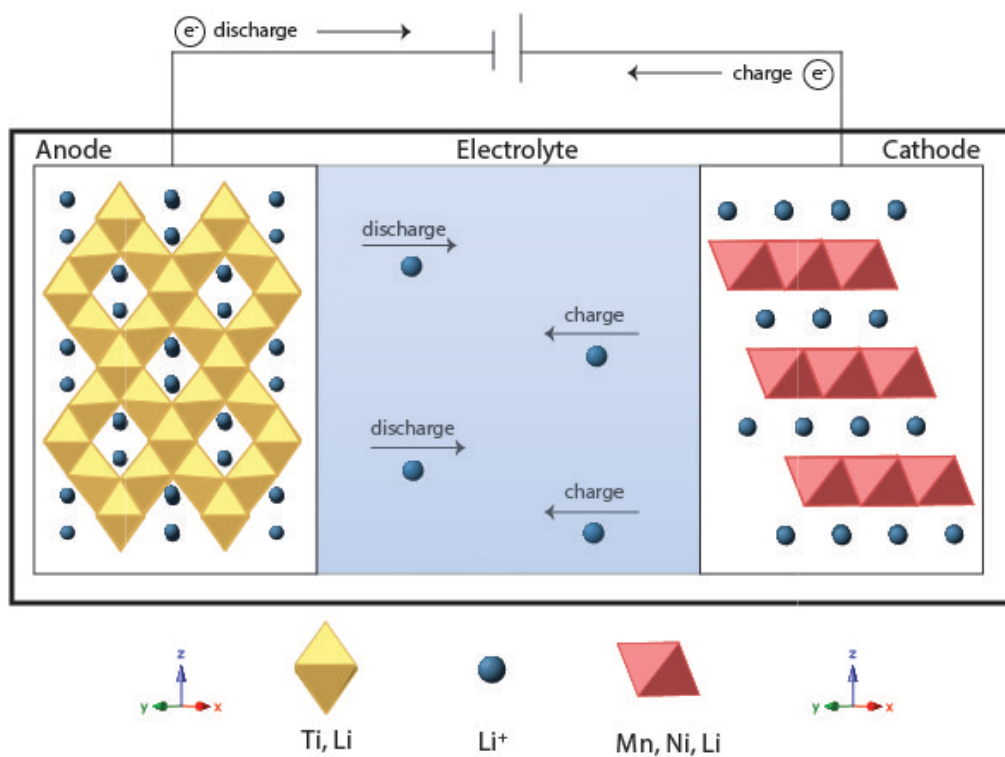
Figure 1.3 Illustration of Li-ion battery operation.

1.4 Soluble lead flow batteries

A particularly attractive flow battery system for large-scale applications is the soluble lead flow battery (SLFB). This is mainly due to the simplicity in its design, leading to quite inexpensive architectures. In typical flow batteries, the electroactive species are dissolved in electrolyte, as opposed to existing in the electrodes themselves. Due to the incompatible redox chemistry occurring at each electrode, however, most flow batteries require two distinct electrolyte solutions, the catholyte and anolyte, being isolated from one another by a separator.[25] These ion-selective separators are not only costly, but are often responsible for eventual flow battery failure, as they are susceptible to cross-contamination.[26] The SLFB provides a considerable advantage, therefore, by not requiring one.

A general schematic of a SLFB is shown in Figure 1.4. It shows a single electrolyte solution, typically composed of lead methanesulfonate and methanesulfonic acid, being pumped from a reservoir and through housing possessing the electrodes. This modular design, separating electroactive material from the electrodes and thereby separating energy and power components, respectively, is an advantage of flow batteries in general, making them highly flexible. The fact that SLFBs possess only one electrolyte is significantly more advantageous, however, because in addition to eliminating the need for an ion-selective membrane, it eliminates the need for a second pump and all other housing and electronics that a second electrolyte would require. The balance of plant for a SLFB is, therefore, considerably cheaper than other flow battery designs, which are already less expensive than alternatives such as lithium-ion.[15]

The reason SLFBs are uniquely apt to operate using a single electrolyte is because

a single species, lead (II) ion (Pb^{2+}), is both oxidized and reduced upon charging the battery. The half-cell and full-cell reactions are:

Negative electrode reaction – (E^0 = -0.13 V/SHE)

$$Pb^{2+} \;+\; 2e^- \;\underset{discharge}{\overset{charge}{\rightleftharpoons}}\; Pb$$
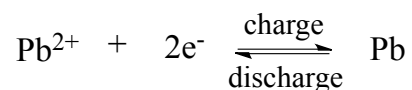
Positive electrode reaction – (E^0 = 1.46 V/SHE)

$$Pb^{2+} \;+\; 2H_2O \;\underset{discharge}{\overset{charge}{\rightleftharpoons}}\; PbO_2 \;+\; 4H^+ \;+\; 2e^-$$
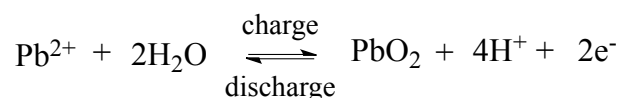
Full cell reaction – (E^0 = 1.59 V/SHE)

$$2Pb^{2+} \;+\; 2H_2O \;\underset{discharge}{\overset{charge}{\rightleftharpoons}}\; PbO_2 \;+\; Pb \;+\; 4H^+$$
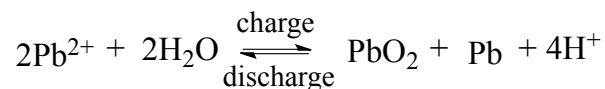
Upon charge, Pb^{2+} dissolved in solution is oxidized into solid lead (IV) oxide (PbO_2) at the positive electrode and reduced to metallic lead (Pb) at the negative electrode. Upon discharge, PbO_2 and Pb undergo the reverse redox reaction to dissociate back into, Pb^{2+}. This reaction chemistry is distinct from the traditional lead-acid battery, which proceeds via a solid-solid redox between lead (II) sulfate ($PbSO_4$) and PbO_2/Pb, at the positive and negative electrodes, respectively.[27] The use of methanesulfonic acid acts to both prevent the formation of $PbSO_4$, which can be problematic, as well as provide a "greener" alternative to sulfuric acid based electrolyte.[28]

Chapter 1, Section 1.4, contains reprinted material from the article, "Achieving high efficiency and cyclability in inexpensive soluble lead flow batteries," as it appears in Energy and Environmental Science, Verde, M. G.; Carroll, K. J.; Wang, Z.; Sathrum, A.; Meng, Y. S. 2013, 6 (5), 1573-1581.The dissertation author was the primary investigator and author of this paper.
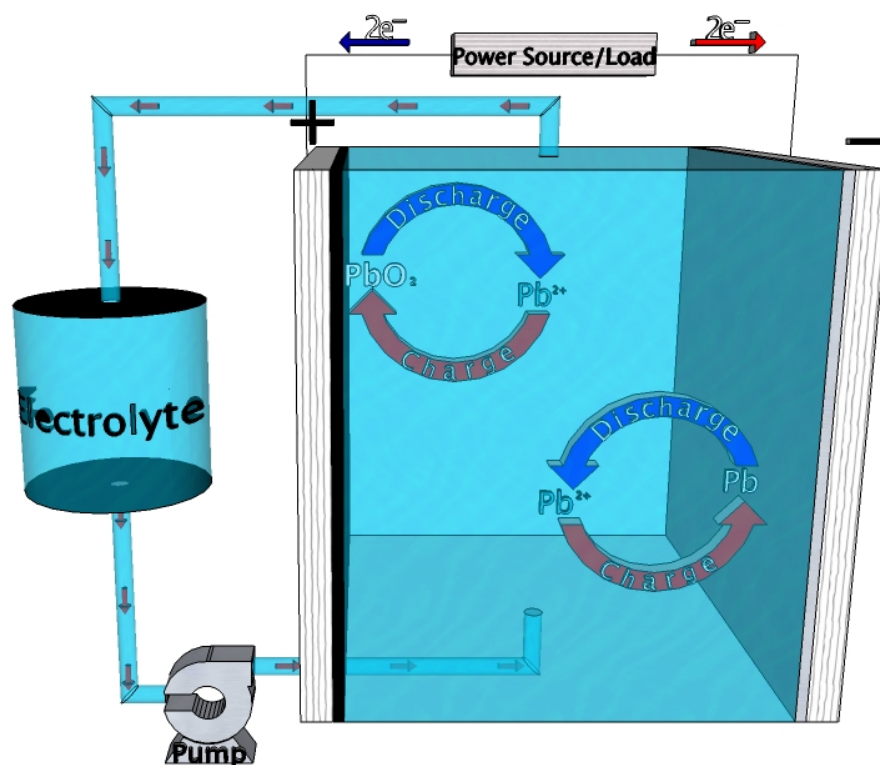
Figure 1.4 General schematic of a soluble lead flow battery (SLFB), consisting of an electrolyte reservoir, pump, and electrode housing.

Chapter 2

Achieving High Efficiency and Cyclability in Inexpensive Soluble Lead Flow Batteries

Here we report significant improvements made in the energy efficiency and cycle life of full-cell soluble lead flow batteries (SLFBs). We describe energy efficiency loss mechanisms, particularly in context to the deposition of PbO_2 at the positive electrode. The morphology and crystal structure of deposits formed at the positive electrode, under galvanostatic and potentiostatic conditions were characterized using both powder x-ray diffraction (XRD) and scanning electron microscopy (SEM). Rietveld refinements were performed to quantitatively determine the phase fraction of α- and β-PbO_2 formed. In addition, electrochemical impedance spectroscopy (EIS) was used to describe the charge-transfer reaction occurring at the positive electrode during conditions that promote the formation of various PbO_2 morphologies. These features were used to evaluate and predict the long-term cycling stability of SLFBs as well as to diagnose potential problems arising during battery operation. We demonstrate that conditions optimized to preferentially deposit nanoscale PbO_2 leads to long battery lifetimes, exceeding 2,000 cycles at 79% energetic efficiency.

2.1 Broader context

Motivated by booms in the electronics industry and the increased demand of hybrid and electric vehicles, the development of high energy density storage systems has

been hotly pursued in recent years. In addition, the economic and geopolitical instability of oil, has also accelerated demand in large-scale energy storage systems for use in smart grids, to assist in load leveling, peak shaving and frequency regulation for renewable energy systems such as solar and wind. For these applications, however, high energy density is not necessarily the most determining feature for an energy storage system to possess. Considerations such as cost, durability, longevity and flexibility in design and operation take precedence since their size and weight in large-scale applications are not as restricted. For these reasons, flow batteries have begun to garner a great deal of attention. Perhaps the most simple and inexpensive of these is the soluble lead flow battery (SLFB). Here we describe critical conditions necessary to achieve extended lifetimes, greater than 2,000 cycles, in these batteries.

2.2 Introduction

In a series of recent papers, Pletcher et. al. established much of the work leading to SLFBs as they exist today.[29-37] Those studies provide a very thorough analysis of Pb and PbO_2 deposition under an array of conditions, such as electrolyte composition, electrode substrate, temperature, and current density. While optimized full-cells operating at a current density of 10mA/cm^2 could achieve 100-200 cycles, lifetimes dropped below 100 cycles at 20mA/cm^2, with energetic efficiencies between 60-65%.[36, 38] Those are relatively poor statistics compared to other flow battery technologies, such as vanadium redox, however, which are able to boast energetic efficiencies of 80% for over 1,000 cycles.[39] It has been determined that the two major problems associated with SLFBs are dendrite growth of Pb at the negative electrode and the partial irreversibility of PbO_2 at

the positive electrode.[30] The use of leveling agents such as sodium lignosulfonate and hexadecyltrimethylammonium cation ($C_{16}H_{33}(CH_3)_3N^+$) have been shown to mitigate Pb dendrite formation,[31, 33] but overcoming inefficiency at the positive electrode continues to be a problem.

Optimization of the Pb^{2+}/PbO_2 couple at the positive electrode has been a more challenging task than of the $Pb^{2+/}Pb$ couple at the negative electrode because of the complexity of reactions occurring at the former. This is reflected in the overpotential of each half-reaction – being only ~90mV at the negative electrode, but ~450mV at the positive electrode. The considerably higher overpotential resulting at the positive electrode has been explained in terms of a high concentration polarization by reaction intermediates formed there.[40] In addition to voltaic inefficiency, current inefficiencies partially prevail due to a competing oxygen evolution reaction (OER), at even moderately high current densities, typically greater than $50mA/cm^2$, depending upon the electrolyte composition.[34] Several possible mechanisms have been put forth as to the nature of the OER in this system,[40-41] but the most general form is:

(E^0 = 1.23 V/SHE)

$$2H_2O \longrightarrow O_2 + 4H^+ + 4e^-$$
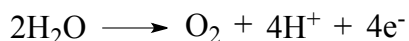
This undesirable side reaction can be minimized by low current density charging, but a considerable degree of current efficiency is still lost because of the incomplete reduction of PbO_2, upon discharge.[29] In many cases, nearly all the lost current efficiency can be accounted for by the PbO_2 mass left behind on the positive electrode after discharge.[36]

The critical nature of this incomplete reduction and the factors contributing to it are the focus of this chapter. Previous studies have discussed the likely formation of oxygen deficient PbO_x species, upon discharge.[42] The exact stoichiometry of such species are unclear, however, as only qualitative studies suggest $1 \leq x \leq 2$.[32] Oxygen deficiency in PbO_2 is prevalent[43] and the formation of such species is likely, as models incorporating them accurately predict the unique voltage profile of SLFBs.[44] In addition to the formation of PbO_x, two distinct polymorphs of PbO_2 are known to form at the positive electrode; they are the orthorhombic α-PbO_2 and tetragonal β-PbO_2. Using XRD, Walsh et. al. have described the preferential formation of one polymorph over the other, under a variety of conditions.[35, 45] They concluded that pure α-PbO_2 forms during initial SLFB cycling, but a mixture of each polymorph forms upon later cycles, leading to battery failure. We offer an alternative hypothesis, however, by performing Rietveld refinement on PbO_2 XRD and considering effects such as preferred crystallite orientation, size, and strain. We propose that efficient and long cycle life is not dependent upon the formation of α-PbO_2, as has been suggested, but relies much more heavily on the morphology of PbO_2 formed. We show that both polymorphs are present upon initial cycling and that their nanoscale morphology is a more critical and determining feature for battery success. We carefully analyze the relation between long-term performance and battery charging potential – specifically highlighting the relationship between that potential and the morphology of PbO_2 formed. In optimizing conditions to preferentially form nanoscale PbO_2 we show that SLFBs can achieve more than 2000 cycles at 79% energetic efficiency

2.3 Experimental

2.3.1 Materials and reagents

Electrolyte used in all electrochemical cells were prepared using water from a Millipore ICW-3000 system (18MΩcm resistivity), reagent grade lead methanesulfonate ($Pb(CH_3SO_3)_2$), Aldrich 50wt.% in H_2O, and ≥99.5% methanesulfonic acid (CH_3SO_3H), Sigma-Aldrich. Electrolyte compositions always consisted of 0.7M $Pb(CH_3SO_3)_2$ and 1.0M CH_3SO_3H, which was chosen to optimize Pb^{2+} solubility and pH during the 1hr charge/discharge windows that batteries were subject to. The solubility and, therefore, energy density of SLFBs are intimately related to the electrolyte pH, which can fluctuate considerably during cycling; according to reaction (3) it is shown that the concentration of H^+ in solution increases twice as fast as the oxidation and reduction of Pb^{2+} into PbO_2 and Pb, respectively.

2.3.2 Electrochemical testing

All full-cell SLFBs were assembled and electrochemically tested by submerging graphite electrodes, spread ¼'' apart, in stirred cylindrical vessels filled with 140mL of electrolyte; each electrode had an exposed surface area of 2.5cm x 3.5cm. Both galvanostatic and potentiostatic cycling tests were performed using an Arbin BT2000 battery testing system. Electrodes were consistently subject to a current density of 20mA/cm^2 and discharged to 1.1V. The electrochemical performances of batteries were evaluated by three main criteria: 1) Coulombic efficiency (η_C), the ratio of the average discharge capacity ($Q_{discharge}$) to the average charge capacity (Q_{charge}); 2) voltaic efficiency (η_V), the ratio of the average discharge voltage ($V_{discharge}$) to the average charge voltage

(V_{charge}); 3) energetic efficiency (η_e), the average discharge energy ($E_{discharge}$) to the average charge energy (E_{charge}).

$$\eta_C = \frac{Q_{discharge}}{Q_{charge}}$$

$$\eta_V = \frac{V_{discharge}}{V_{charge}}$$

$$\eta_e = \frac{E_{discharge}}{E_{charge}}$$

2.3.3 Scanning electron microscopy

Following electrochemical cycling and prior to other forms of characterization, deposited anode and cathode materials were rinsed with deionized H_2O while still adhered to each electrode. Deposits were dried in vacuum at room temperature. Scanning electron microscopy (SEM) was performed on material still adhered to electrodes, with no further treatment besides washing with water. Images were collected using a Phillips XL30 ESEM at an accelerating voltage of 20kV.

2.3.4 X-ray diffraction

X-ray diffraction (XRD) measurements were performed using a Bruker D8 advance diffractometer with a Bragg-Brentano θ-2θ geometry and a Cu Kα source (λ=1.54Å). Samples were scanned from 10° to 80° with a scan rate of 0.025^o per second. XRD was performed on deposits that had been scraped off of the electrode and ground into a fine powder. A reflection peak for graphite, space group R-3m R, is present in all XRD spectra, as it was unavoidable to completely exclude graphite from scraped off PbO_2 deposits. Removing and grinding PbO_2 was necessary in order to quantitatively

determine the relative abundance of various PbO_2 phases deposited on the positive electrode; otherwise, due to texturing of as deposited PbO_2, preferred growth orientations of specific crystal planes skew XRD peak intensities.[46] Rietveld refinement was performed using GSAS/EXPGUI software.[47]

2.3.5 Electrochemical impedance spectroscopy

Electrochemical impedance spectroscopy (EIS) was performed using a Solartron 1287 system coupled with a Solartron 1260 frequency response analyzer. The full-cell SLFBs described above were analyzed using EIS, in conjunction with a third, Ag/AgCl, reference electrode. Graphite was, therefore, used as both working and counter electrodes. The surface area of exposed electrodes was 2.5 cm x 3.5 cm. The impedance of the positive electrode was measured at various fixed potentials, using AC amplitude of 10mV. Fixed potentials of 1.44, 1.54, and 1.64V vs. Ag/AgCl were applied during EIS measurements, without allowing the cell to equilibrate at OCV. Spectra were obtained in the frequency range of 10^{-2} Hz to 10^5 Hz. Equivalent circuit modeling was performed using the ZView impedance software package.

2.4 Results and discussion

2.4.1 Electrochemical indications of failure

A common deterioration mechanism of SLFBs is represented by their electrochemical efficiencies (Figure 2.1a). The critical feature in the plot of Figure 2.1a, highlighted in green, occurs when the battery nears 90 cycles. At that point there is

simultaneous rise in voltaic efficiency and decline of Coulombic efficiency. The rapid drop in Coulombic efficiency is not offset by the small increase in voltaic efficiency, therefore resulting in an overall decrease in energetic efficiency. This marked "inflection" or, simultaneous increase in voltaic efficiency and decrease in Coulombic efficiency, is a unique characteristic of SLFBs. It indicates a dramatic decrease in cell performance and accelerated failure.

To more thoroughly describe the electrochemical characteristics of the battery during this sudden change in efficiency, we highlight three points within the green box and inset of Figure 2.1a: 1) before the inflection, at the 80th cycle; 2) during the inflection, at the 90th cycle; 3) after the inflection, at the 95th cycle. The charge/discharge voltage of each of these cycles is plotted in Figure 2.1b. This figure shows that before the efficiency inflection, the charge voltage profile consists of a major plateau at ~2.0V. Preceding that plateau, but during the same cycle, there exists a sloping region beginning ~1.75V and a smaller plateau ~100mV higher. The shape of the voltage profile at the 80th cycle is fairly representative of previous cycles. Upon approaching the efficiency inflection, however, the higher voltage plateau becomes shorter and the sloping region becomes longer, as seen in the 90th charge voltage profile. After the inflection, the high voltage plateau is no longer met. A major voltage plateau still occurs in the 95th cycle, but it has reduced by ~75mV, as indicated by the vertical arrow in Figure 2.2b.

The horizontal arrow in Figure 2.1b indicates that the discharge time of the 95th cycle has decreased. Before the efficiency inflection, the duration of discharge is relatively constant. After the inflection, however, it is consistently lower. The charge time and therefore, amount of Pb and PbO_2 being deposited on each electrode remains

constant in all cycles. The decrease in both discharge time and Coulombic efficiency suggests that an increasing amount of unreacted deposit remains on the electrodes after each cycle. The accelerated accumulation of these deposits can be physically observed after the efficiency inflection. The major feature associated with this capacity loss is the depression of the high voltage plateau. Extension of the sloping region during charge results in slightly lower discharge overpotentials, as shown by the black and red dotted regions in Figure 2.1b. Only when the original position of the high voltage plateau fails to be met, however, does the capacity begin to considerably fade. We hypothesize that the major problem associated with the depression or elimination of the original voltage plateau is a change in PbO_2 morphology, which is not conducive to efficient dissolution.

We specify formation of PbO_2 at the positive electrode because the shape of the full-cell voltage is a reflection of the Pb^{2+}/PbO_2 half-cell potential. The distinct low and high voltage charging regimes are exclusively present in Pb^{2+}/PbO_2 half-cell measurements.[29] In addition, the low voltage regime arises only after PbO_2 reduction. Several groups have suggested that the reduction of PbO_2 into Pb^{2+} does not reach completion.[42, 45] It has been proposed that PbO_2 is partially reduced into an oxygen deficient form of PbO_2 (PbO_x, $1 \leq x \leq 2$.). The low sloping portion of subsequent charge voltages may, therefore, be due to more easily oxidized PbO_x species into PbO_2. The mechanism and characterization of incomplete PbO_2 reduction has been qualitatively explored using electrochemical[48] and energy dispersive x-ray spectroscopy (EDS)[32] measurements, but quantitative analysis has yet to be performed. An alternative hypothesis proposed by Oury et.al suggests that the low voltage regime is instead due to a change in electrode surface area.[49] They suggest that the morphology of PbO_2 left behind

upon discharge increases surface area and effectively decreases the current density and resulting over-potential. In either case, further characterization of material deposited at low voltage would be invaluable, since extension of the low charging voltage or any other mechanism resulting in depression of the initial plateau, leads to very poor energetic efficiency.
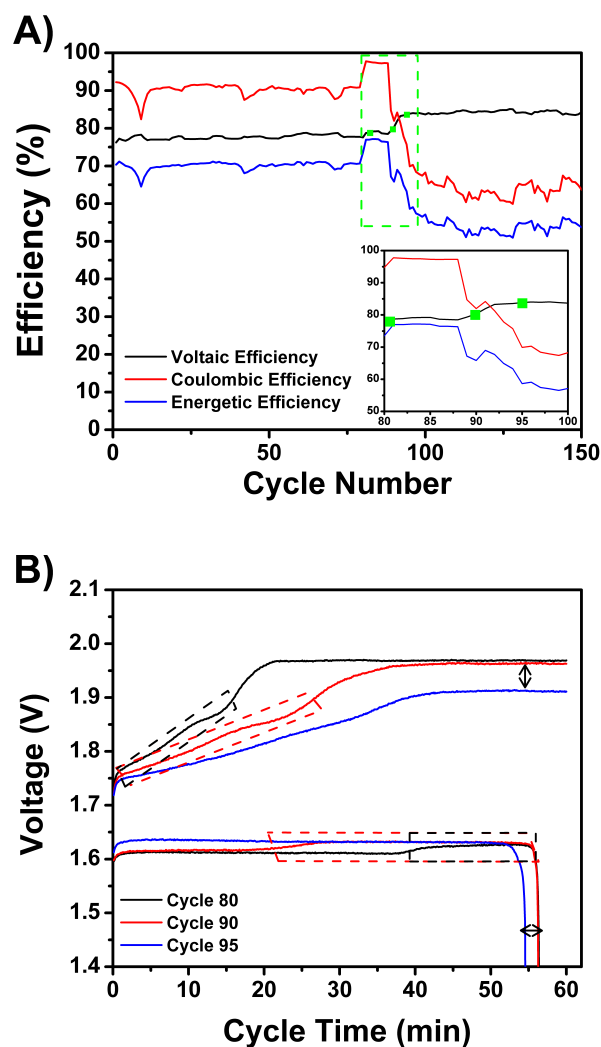
Figure 2.1 SLFB electrochemistry. (A) Electrochemical efficiencies of SLFB. Dotted region highlights inset, which focuses on 3 specific cycles. (B) Charge/discharge profiles of the 3 cycles indicated by inset on left.

2.4.2 Characterization of potentiostatically charged cells

In order to more directly elucidate the morphological and phase characteristics associated with the different voltage regimes, batteries were potentiostatically charged at 1.8, 1.9, and 2.0V. Figure 2.2 shows the electrochemical characteristics of three batteries charged at these fixed potentials, for 1hr. This figure shows both the charging voltage and corresponding potentiostatic current-time transients. Following the initial double-layer charging current, the current of the battery charged at 1.9V increases exponentially, suggesting progressive nucleation.[50] The current of the battery charged at 2.0V increases very rapidly and linearly, however, suggesting instantaneous nucleation. Comparing the time required to reach maximum current, it is shown how long it takes nuclei to fully overlap one another and completely cover the electrode surface.[51] This occurs at ~2 minutes into charging at 2.0V, ~9 minutes after charging at 1.9V, and never happens during the 1-hour charging period at 1.8V. These results suggest that at 2.0V, a large number of nuclei quickly form and coalesce to create layers of nanoparticles. At lower voltages, however, fewer nuclei form and grow, as new nuclei continue to form on the electrode surface. This follows a first order approximation of the nucleation law for a uniform probability with time.[51]

Interpretations of the potentiostatic current-time transients are supported by positive electrode SEM images shown in Figure 2.3. The latter represents particle morphologies of PbO_2 deposited after the 1hr potentiostatic charge conditions. They show that at 1.8V charging, growth is favored, as large *pyramidal* PbO_2 structures were

formed. In addition, nuclei have not completely overlapped, as graphite substrate is still visible. Particle sizes decreased at 1.9V charging, however, and resulted in a more *cubic* morphology. This specific trend in the shape and morphology of electrodeposited materials, as a function of applied overpotential has been demonstrated in similar electrolyte and crystal systems.[52] At 2.0V charging, a uniform, nanoscale morphology, consisting of ellipsoid nanoparticles or "nanorice",[53] was formed. These results are consistent with galvanostatically charged batteries as shown in Figures 2.4 and 2.5. Those figures show that when a charging potential of 2.0V is met, nanoscale PbO_2 is consistently formed. Even upon cycling, when larger PbO_2 particles are initially formed at lower voltages, nanoscale PbO_2 is immediately formed on top when 2.0V charging resumes.

Figure 2.3 shows that trends in particle shape and morphology at each voltage is maintained over extended charge periods as well. Longer charge times were necessary at low voltages to deposit an appreciable amount of PbO_2 for XRD analysis. Whereas a capacity of 1.37×10^{-1}Ah is achieved after a 1hr charge at 2.0V, only 2.3×10^{-3}Ah is met after 1hr charge at 1.8V. The XRD of PbO_2 deposited at each potential is shown in Figure 2.6. Vertical dotted lines indicate reflections of pure α- and β-PbO_2 according to the International Crystal Structure Database (ICSD). These two polymorphs are very similar to one another, as both are comprised of Pb^{4+} within distorted octahedral, possess similar Pb-O bond lengths, and differ in standard reduction potential by less than 10mV.[54]

Figure 2.6 shows that upon a single charge at 1.8, 1.9, or 2.0V, a mixture of α- and β-PbO_2 is always formed. Several groups have reported qualitative analyses suggesting that β-PbO_2 preferentially forms at low charging current densities.[35, 45] We

performed Rietveld refinement to quantitatively determine that the ratio of α- to β-PbO$_2$

deposited at 1.8V is 41:59, respectively. At the comparatively higher current density

applied during 1.9V charging, the ratio of α- to β-PbO$_2$ was determined to be 97:3,

respectively. Rietveld refined phase fractions, as well as fitted lattice parameters and

reliability factors, are shown in Table 2.1. It is generally rare, however, to form such a

high percentage of α-PbO$_2$ in acidic solutions.[55] Despite this, literature commonly

suggests that α-PbO$_2$ forms in equal and to often-greater degrees than β-PbO$_2$ in the

acidic electrolyte of SLFBs.[45] At 2.0V charging, however, it is clear that XRD peaks have

become significantly broadened. Considering the very small particle sizes formed at 2.0V

(Figure 2.3), it is not surprising that decreased crystallite dimension and/or strain exist.

Using FWHM parameters, an estimation of crystallite sizes, based on the Scherrer

equation, was determined to be 9nm. Due to the slightly lower reduction potential of β-

PbO$_2$, it is possible that it forms smaller nuclei and crystallite sizes before α-PbO$_2$. A

decrease in β-PbO$_2$ peak intensity does not necessarily imply, therefore, less β-PbO$_2$

exists – it could mean that β-PbO$_2$ crystallite sizes have simply decreased, relative to α-

PbO$_2$. Indeed when the XRD peaks of α-PbO$_2$ have broadened during 2.0V charging, the

relative peak intensities are much more proportional to β-PbO$_2$. The largest reflections, at

~32.0, 36.5, and 49.0° result from the overlap of α- and β-PbO$_2$ peaks. Figure 2.7 shows

that β-PbO$_2$ is clearly present during initial cycles of galvanostatically charged cells as

well. These results suggest that maintaining the initial voltage plateau ~2.0V is critical to

ensure the deposition of nanoscale PbO$_2$, at the same time it is important to point out that

α-PbO$_2$ is not exclusively present.
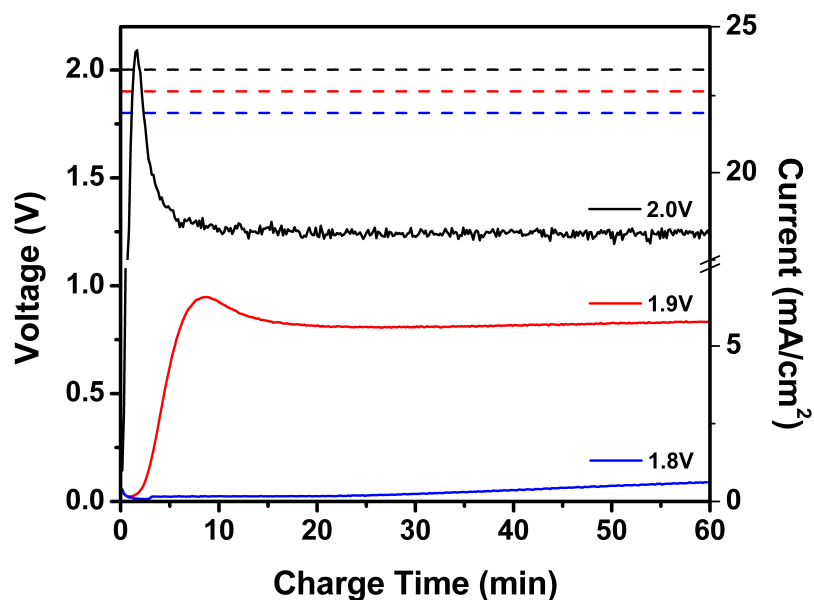
Figure 2.2 SLFB current-time transients. Voltage (dotted lines) and current-time transients (solid lines) of three SLFBs potentiostatically charged at 1.8V (blue), 1.9V (red), and 2.0V (black) for 1 hr.
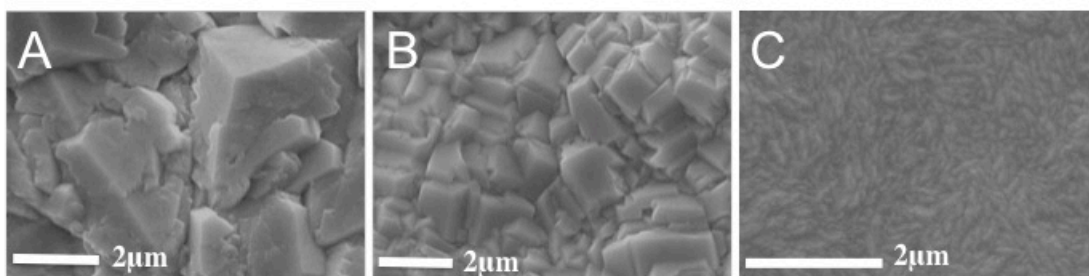
Figure 2.3 SEM images of positive electrode deposits from SLFBs potentiostatically charged at (A) 1.8 , (B) 1.9 V, and (C) 2.0V.
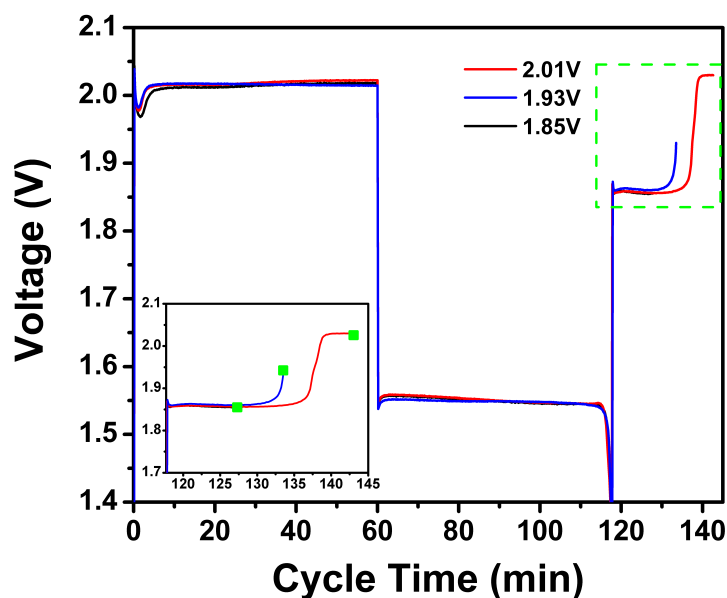
Figure 2.4 Voltage profile of SLFBs. Three were galvanostatically charged, but stopped during their second charge cycled at three different points – 1.85 V, 1.93 V, and 2.01 V, highlighted by the inset.
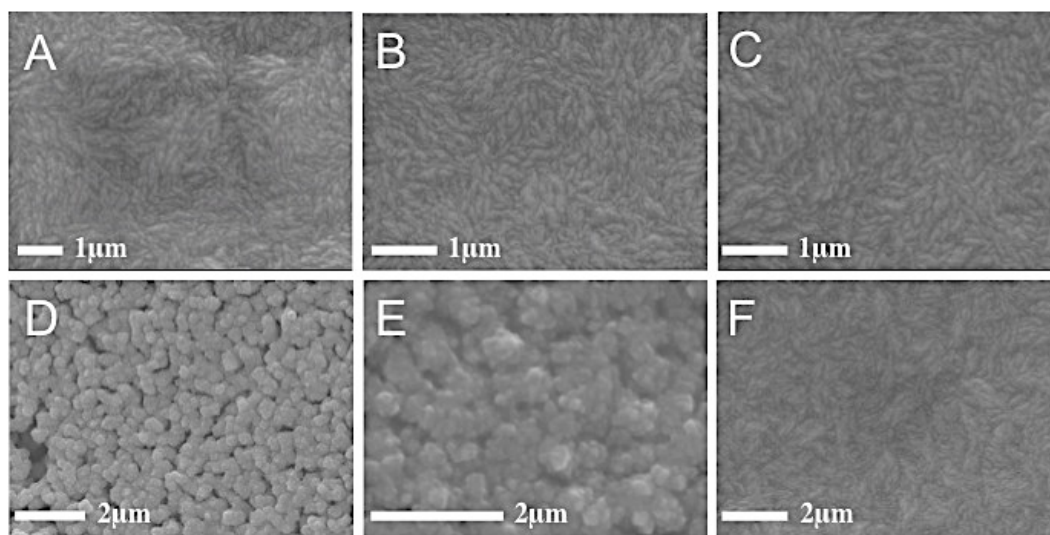
Figure 2.5 SEM images of positive electrode deposits from galvanostatic cycling. They were formed during the 1st cycle at (A) 10 minutes, (B) 15 minutes, and (C) 20 minutes into charge, as well as deposits formed during the 2nd charge cycle at the (D) 1.85V plateau, (E) 1.93V inflection, and (F) 2.01 V plateau, from SLFBs, galvanostatically charged.
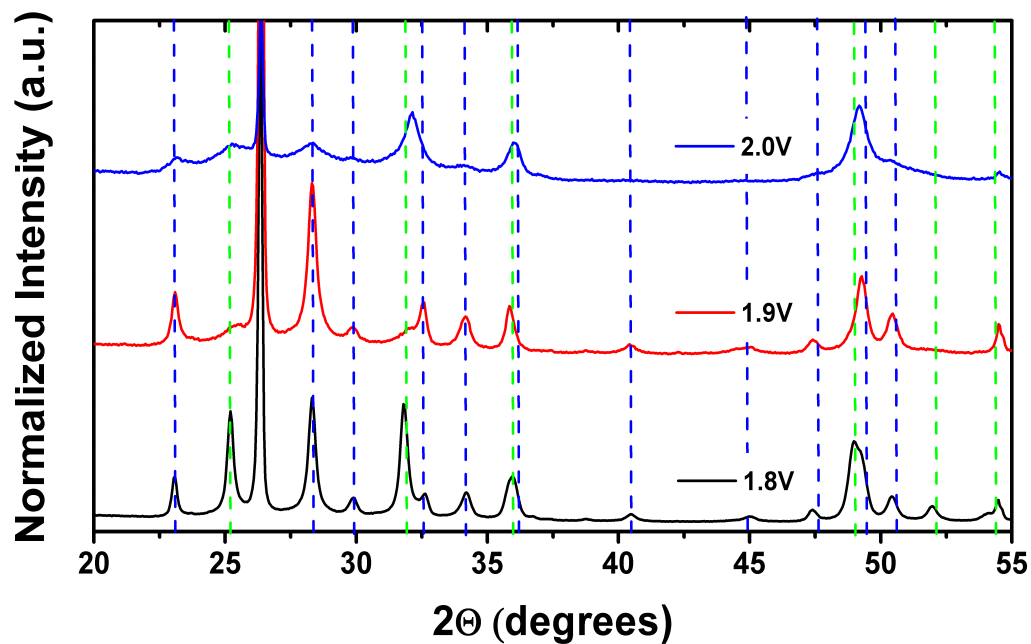
Figure 2.6 XRD patterns of positive electrode deposits from potentiostatically charged SLFBs. They were charged at 1.8V (black), 1.9V (red), and 2.0V (blue), for 1hr. Dotted lines represent standard XRD reflections of α-PbO$_2$ (blue) and β-PbO$_2$ (green). Peak at 26° corresponds to graphite substrate.
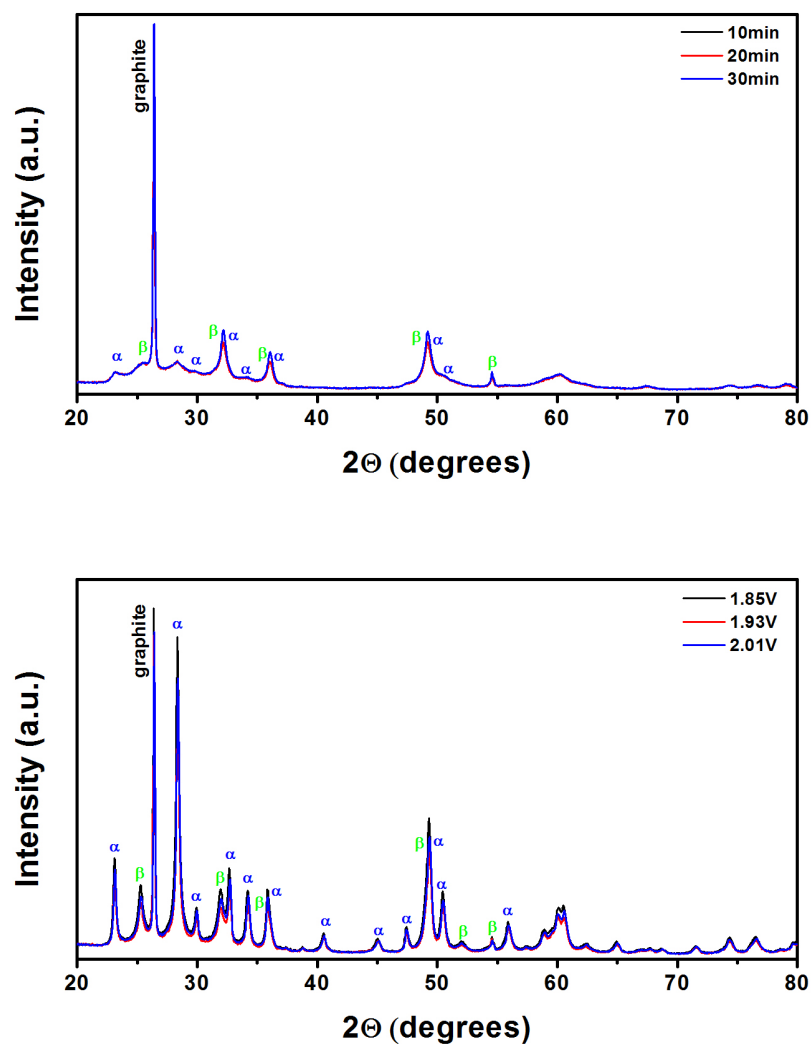
Figure 2.7 XRD patterns of positive electrode deposits from galvanostatically charged SLFBs Top corresponds to spectra of positive electrode deposits from SLFBs 10 (black), 20 (red), and 30 (blue) minutes into the 1st cycle, charged at 20mA/cm². Bottom corresponds to spectra of positive electrode deposits formed during the 2nd cycle at the 1.85V plateau (black), 1.93V inflection (red), and 2.01V plateau (blue).

Table 2.1 Rietveld refined fit parameters of positive electrode deposits from SLFBs potentiostatically charged at 1.8 V and 1.9 V.

Charge Voltage	Phase Fraction		Reliability Factors		α-PbO$_2$ Lattice Parameters (P 42/m n m)			β-PbO$_2$ Lattice Parameters (P b c n)		
	α	β	Rwp	Rp	a	b	c	a	b	c
1.8V	41.(8)	59.(2)	9.78	6.70	4.97(8)	5.92(3)	5.44(0)	4.95(4)	4.95(5)	3.38(1)
1.9V	96.(6)	3.(4)	12.70	8.75	4.99(3)	5.93(3)	5.44(8)	4.93(5)	4.93(4)	3.36(7)

2.4.3 Electrochemical impedance spectroscopy

To further describe and gain insight into the electrochemical deposition of PbO$_2$, as it relates to the applied overpotential, we performed electrochemical impedance spectroscopy (EIS) on full-cells. Using the positive electrode as the working electrode, impedance was measured at 1.44, 1.54, and 1.64V vs. Ag/AgCl. These voltages were chosen as they correspond to the full-cell potentials described previously – 1.8, 1.9, and 2.0V. Figure 2.8 represents the Nyquist plots obtained from those measurements, which were fit to a base equivalent circuit model, shown in the inset. The equivalent circuit used in fitting contains a resistor (R1 – solution resistance) followed by an RC circuit in parallel. The RC circuit corresponds to a resistor (R2 – charge transfer resistance) and a constant phase element (CPE), which was used in place of an ideal capacitor to incorporate changes in the electrode such as surface area. Other groups have reported the use of a second RC circuit to incorporate effects of the OER occurring at the positive electrode.[41] We did not, however, because evidence suggests the OER is a minor side-reaction occurring in our solution composition and with the relatively low current densities applied in our study.[34]

Figure 2.8a shows that at each voltage applied, a single semicircle ensues,

indicating a single charge-transfer event. As the voltage is increased, the semicircle becomes shorter and more depressed. Electron transfer due to the Pb^{2+}/PbO_2 half-reaction proceeds faster, as the semicircles develop at higher frequencies; at similar positions along the semicircles formed by each 100mV increase in overpotential, the AC frequencies highlighted are shown to increase by more than an order of magnitude. The enhanced reaction kinetics is quantitatively shown in Figure 2.8b, which represents the charge-transfer resistance at each voltage.

The charge-transfer resistance (R2) is shown to drop off rapidly with increasing overpotential, at a rate described by the Bulter-Volmer equation. The SEM images shown in Figure 2.8b lend support to the interpretation of nucleation and growth described previously, in terms of the relationship between R2 and overpotential. With slow charge-transfer kinetics and low overpotential, 1.46V vs. Ag/AgCl, nucleation occurs slowly, favoring growth before the entire electrode surface is covered with PbO_2. At high overpotential, 1.64V vs. Ag/AgCl, charge-transfer is two orders of magnitude higher; nucleation occurs very fast, as a multitude of small particles form and coalesce before growth becomes favorable.
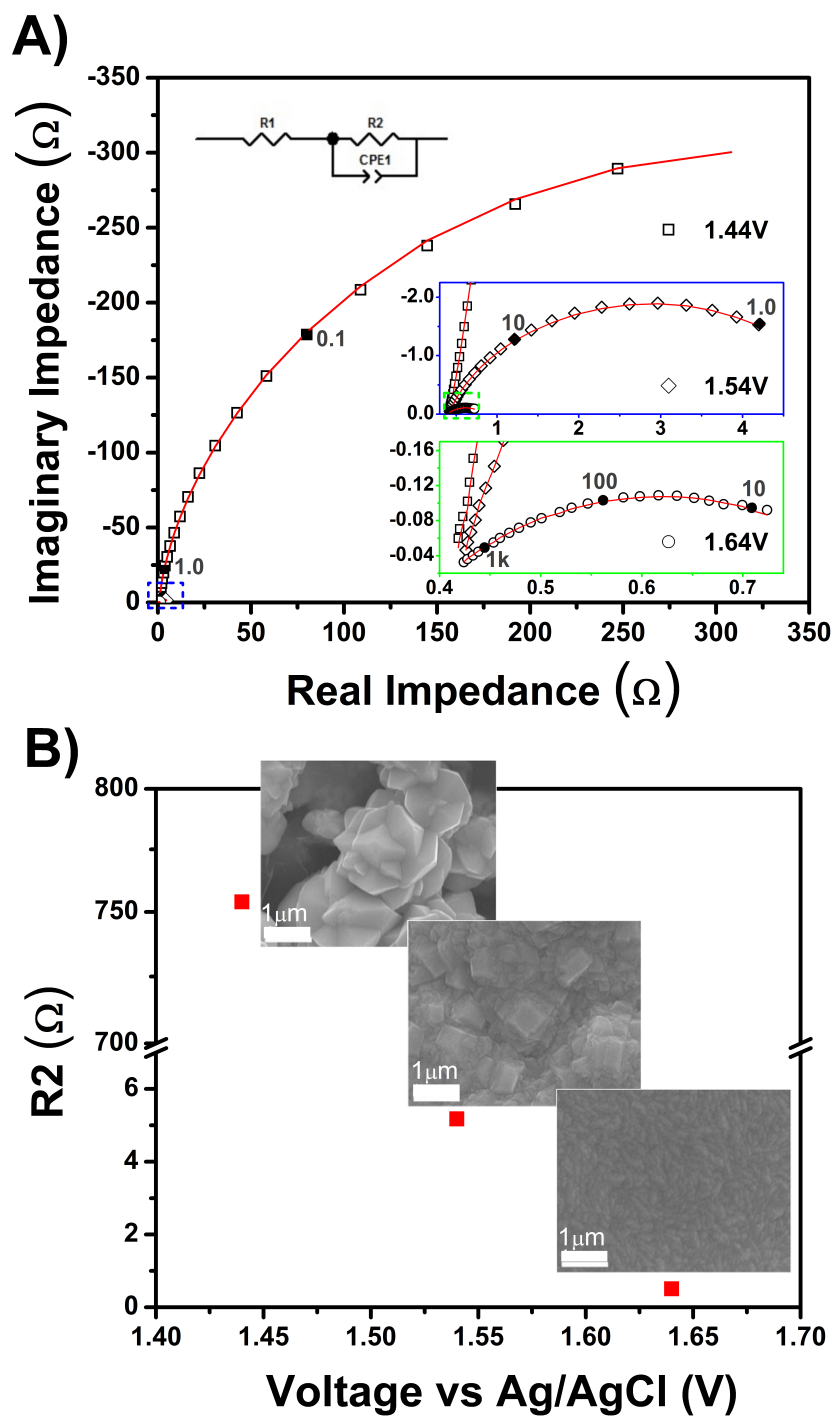
Figure 2.8 SLFB EIS plots. (A) Nyquist plots from SLFBs charged at 1.44V, 1.54V (blue inset), and 1.64V (green inset) vs Ag/AgCl reference electrode. Select AC frequencies indicated by shaded points. Red line indicates equivalent circuit fit using model shown by inset. (B) Charge transfer resistance (R2) from fits and associated SEM images of PbO_2 formed at those voltages.

2.4.4 Morphology and efficiency

Controlling the size of particles electrochemically deposited on a surface is commonly described in terms of their critical radius, which is inversely proportional to overpotential.[51] Figure 2.9 shows the voltage profile of two batteries potentiostatically charged at 1.8V and 2.0V. They were both charged to a capacity of 1.37×10^{-1}Ah and, therefore, had the same mass of PbO_2 deposited upon charge. As described previously, however, the different overpotentials resulted in large particle growth in the former and nanoparticle growth in the latter. Each battery was then galvanostatically discharged at 20mA/cm^2. Figure 2.9 shows that the battery initially charged at 2.0V exhibited much better discharge capacity than the one charged at 1.8V. While the Coulombic efficiency of the former was 95.1%, it was only 57.8% for the latter. This lost capacity resulted from the incomplete dissolution of PbO_2 into solvated Pb^{2+}. Indeed, the inset of Figure 2.9 shows that a great deal more mass of PbO_2 was left behind on the positive electrode initially charged at 1.8V. Of the mass deposited upon charge, 45.0% remained on the positive electrode charged at 1.8V, compared to only 2.6% on the battery charged at 2.0V. These results suggest that by tailoring reaction conditions to specifically form nanoparticle PbO_2, its dissolution at the positive electrode upon discharge is greatly enhanced. In forming larger PbO_2 particles, as is the case in conditions encouraging low overpotential or poor Pb^{2+} diffusion, reduction of PbO_2 into solvated Pb^{2+} is severely impeded.

One condition that is extremely influential to the morphology of PbO_2 deposited, is flow rate. By submerging graphite electrodes in stirred cylindrical vessels, flow can be easily altered by adjusting the stir rate. Figure 2.10 shows the 17th charge profile of three

batteries subject to different stir rates. This figure demonstrates that with slow flow, the low charge voltage regime is extended. Under high flow rate conditions, however, the voltage profile primarily consists of its original plateau at ~2.0V. The SEM images in Figure 2.10 show the specific morphology of PbO_2 deposited at the end of each 17th charge. These images show that the slow flow associated with longer periods of low overpotential leads to larger particle formations. Since these large particles do not undergo PbO_2/Pb^{2+} dissolution as efficiently, this eventually leads to battery failure. One mechanism to prolong battery life and efficiency, therefore, is to increase and optimize flow. Indeed, Figure 2.11 shows that batteries operating in this manner, stirred at 700rpm, can achieve very impressive performances. This figure shows a SLFB galvanostatically charged at 20mA/cm^2 for 1hr and discharged to 1.1V, incorporating no additives, which cycled more than 2,000 times at an average 79% energetic efficiency. The classic lead-acid battery has been known to achieve comparable numbers of cycles.[39] To our knowledge, however, this is the first time soluble lead flow batteries have successfully undergone so many cycles at such high efficiency. Recent reports describing "extended" cycle lives in SLFBs charged at 10mA/cm^2 typically range between 100-200 cycles at 65% efficiency.[36-37] Furthermore, additives such as hexadecyltrimethylammonium cation ($C_{16}H_{33}(CH_3)_3N^+$ or H_2O_2 have been commonly employed to reach even those modest numbers. Our work suggests that the reduction and dissolution of PbO_2 into solvated Pb^{2+} is the major hurdle to overcome in achieving long cycle lifetimes. In comparison, the dissolution of metallic Pb at the negative electrode is a much more kinetically favorable process.[29]
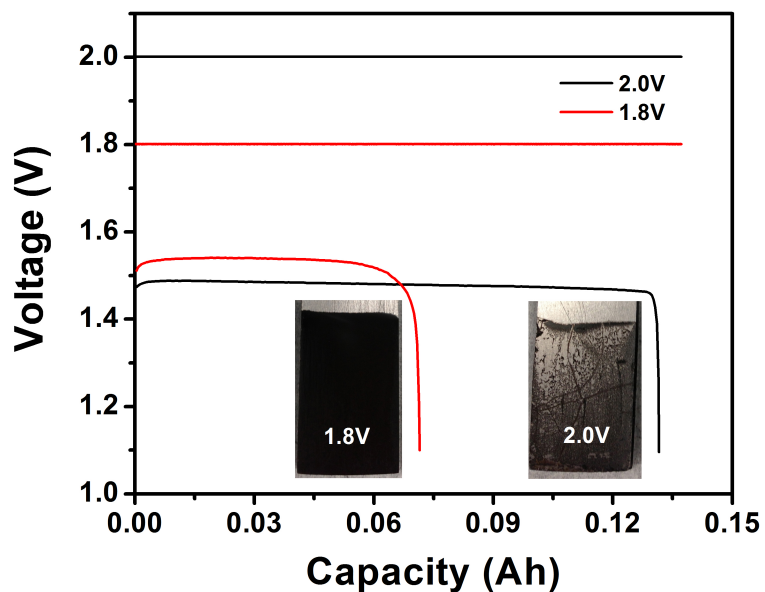
Figure 2.9 SLFB voltages and capacities. Voltage of battery charged at 2.0V (black) and 1.8V (red) to capacity of 1.37×10^{-1}Ah and discharged to 1.1V at 20mA/cm^2. Inset shows optical image of electrodes after full discharge – 45% and 2.6% of PbO$_2$ mass remaining on left and right electrode, respectively.
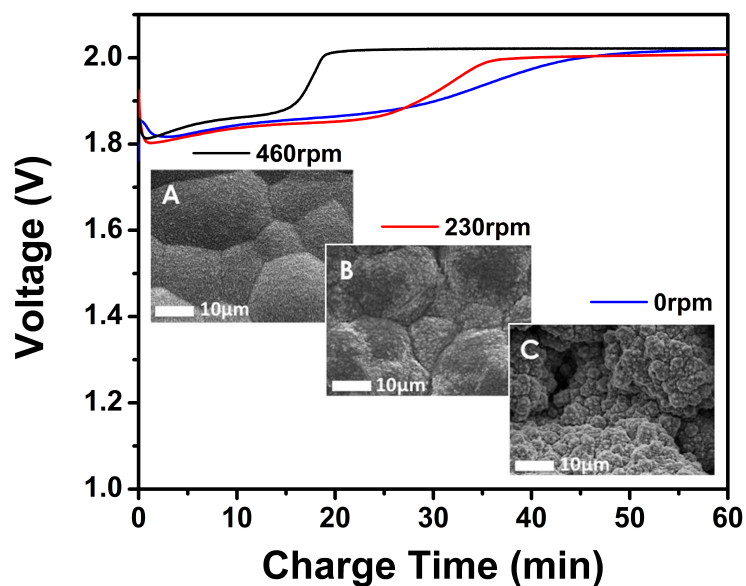
Figure 2.10 Charge voltage of SLFBs during the 17th cycle. Their electrolytes were stirred at 460rpm (black), 230rpm (red), and 0rpm (blue). Inset shows deposit formed at the positive electrode of those batteries, A, B, and C, respectively.
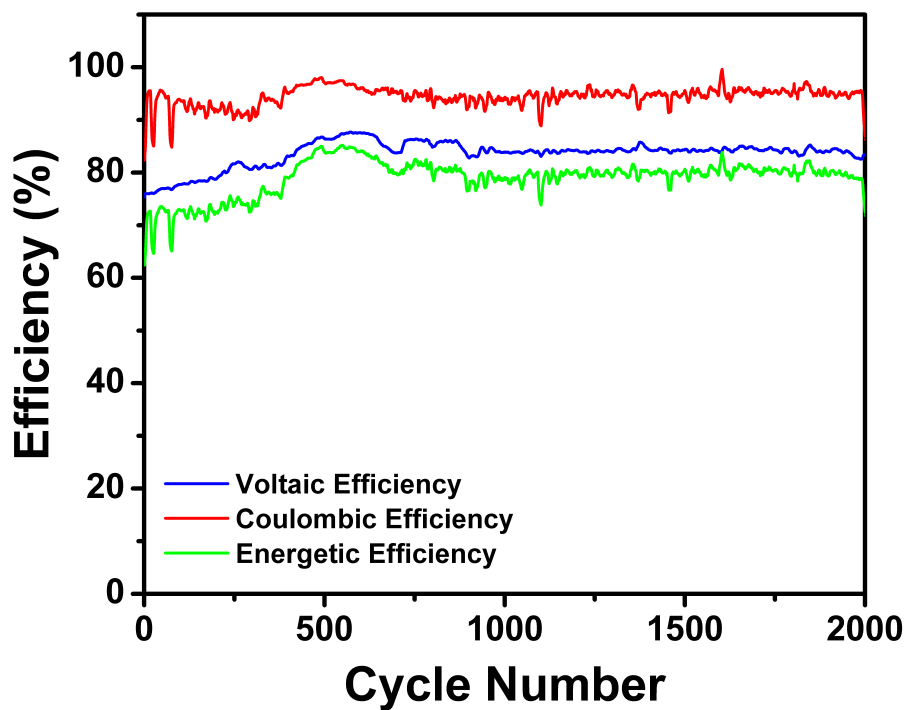
Figure 2.11 Electrochemical efficiencies of a SLFB. It was charged at 20mA/cm^2 for 1hr and discharged at the same current density to 1.1V, 2,000 times at an average 79% energetic efficiency.

2.5 Conclusions

Several features associated with SLFB degradation have been reported here. The onset of electrochemical failure is marked by a simultaneous increase in voltaic efficiency and decrease in Coulombic efficiency. Low Coulombic efficiency leads to both reduced cell capacity as well as build up of electrode deposits, which eventually leads to shorting. The increase in voltaic efficiency is due to the extension of a low charge voltage moiety following the first cycle, as well as a depression of the major charge voltage plateau. This has been attributed to the Pb^{2+}/PbO_2 redox reaction occurring at the positive electrode. Characterization of PbO_2 deposits formed under low and high voltage charging conditions were performed, therefore, to elucidate the mechanism of efficiency loss.

A slightly greater proportion of β-PbO_2 was determined to form under low voltage conditions, compared to α-PbO_2 (in ratio of 59:41). When not taking into account the broadening of XRD peaks due to the formation of nanoparticles possessing small crystallite size and/or strain, α-PbO_2 appears to be formed in excess. At 2.0V charging, however, when PbO_2 nanoparticles are uniformly distributed across the positive electrode, peak broadening in both α- and β-PbO_2 phases dominate, and each phase is clearly present. Large PbO_2 particles were consistently formed at low voltages, in contrast to the formation of nanoparticles at higher voltages. We attribute this to the faster and lower energy formation of small nuclei during conditions of high overpotential. High voltage charging was shown to increase charge-transfer kinetics and lead to instantaneous nucleation, as opposed to progressive nucleation and slow kinetics at lower charge voltages. The problem associated with depositing large particles is the difficulty in achieving efficient dissolution of PbO_2 back into solvated Pb^{2+} upon battery discharge.

Nanoparticles are much better suited to accomplish this dissolution reaction. In order for SLFBs to emerge as a viable candidate for use in large-scale storage applications and compete with alternative technologies such as halogen-halide or vanadium redox batteries, they must be able to demonstrate extended cycle life capability. Here we demonstrate the conditions necessary to achieve that goal, as we have successfully cycled a SLFB more than 2000 times at 79% energetic efficiency. This breakthrough brings the low-cost SLFB back on the chart with other flow battery technologies for large-scale energy storage.

Chapter 2, in full, is a reprint of the article from Energy and Environmental Science, Verde, M. G.; Carroll, K. J.; Wang, Z.; Sathrum, A.; Meng, Y. S. 2013**,** 6 (5), 1573-1581. As described, part of the original introduction was included in Chapter 1. The dissertation author was the primary investigator and author of this paper.

Chapter 3

Effect of Morphology and Manganese Valence on the Voltage

Fade and Capacity Retention of Li[Li$_{2/12}$Ni$_{3/12}$Mn$_{7/12}$]O$_2$

This chapter describes the electrochemical characteristics of the high voltage, high capacity Li-ion battery cathode material Li[Li$_{2/12}$Ni$_{3/12}$Mn$_{7/12}$]O$_2$ prepared using three different synthesis routes: sol-gel, hydroxide co-precipitation, and carbonate co-precipitation. Each route leads to distinct morphologies and surface areas while maintaining the same crystal structures. X-ray photoelectron spectroscopy (XPS) measurements reveal differences in their surface chemistries upon cycling, which correlate with voltage fading. Indeed, we observe the valence state of Mn on the surface to decrease upon lithiation, and this reduction is specifically correlated to discharging below 3.6V. Furthermore, the data shows a correlation of the formation of Li$_2$CO$_3$ with Mn oxidation state from the decomposition of electrolyte. These phenomena are related to each material's electrochemistry in order to expand upon the reaction mechanisms taking place – specifically in terms of the particle morphology produced by each synthetic approach.

3.1 Introduction

The Li-excess class of cathode materials exhibit high average voltages (3.6 - 3.8V, reversibly) and capacities nearly twice that of commercially available cathode materials (e.g. $LiFePO_4$, $LiCoO_2$, or $LiMn_2O_4$).[56-57] Despite their fantastic initial properties, the cathode suffers from an irreversible degradation process that limits cycle life. This degradation has been the subject of extensive investigations in the hopes of identifying methods to mitigate these losses.[58-62] Lu et. al. first studied in detail the nickel-manganese Li-excess materials in 2001.[63-64] They described them as being isostructural to $LiCoO_2$, which crystallizes in a hexagonal structure ($R\overline{3}m$). In addition to Li occupying its own layer in 3a sites, it occupied some 3b sites of the transition metal layer as a solid solution. In this way, the family can be represented as $Li[Li_{1/3 - 2x/3}Ni_xMn_{2/3-x/3}]O_2$ for $0 < x \leq \frac{1}{2}$. Other groups prefer to describe the family as a composite, consisting of two components $(x)Li_2MnO_3 \cdot (1-x)LiNi_{0.5}Mn_{0.5}O_2$.[65] The fundamental composition of the pristine material is still being debated, as evidence to support both the solid solution and two-component models exist.[66-67]

While it is well accepted that in either case Ni is redox active between Ni^{4+} and Ni^{2+}, the role of Mn is subject to greater debate. A variety of X-ray techniques, especially X-ray absorption spectroscopy (XAS), have been used to identify and characterize the active species within batteries. Park et. al. concluded from the Mn K-edge of Li-excess that bulk Mn remained in the Mn^{4+} state during all states of charge.[68] More recently, Koga et. al. drew the same conclusion using an operando XAS study.[69] The shape of the K-edge irreversibly changes upon charge past 4.5V, suggesting that structural rearrangement occurs, and complicates the interpretation of a shift. Shifts in certain

regions of the edge have therefore been used to imply Mn is indeed redox active.[70-71] Ito et. al. specifically analyzed the pre-edge to suggest that some Mn was reversibly reduced during discharge.[72] Carroll et. al. combined transmission mode with total electron yield to suggest differences in Mn-valence exist in the bulk and surface.[73] In these cases, however, it is not clear whether enough Mn is being reduced to explain the large reversible discharge capacities observed in these materials. Some species other than Ni must be electrochemically active because stoichiometries possessing between ⅓ and ⅕ Ni routinely obtain discharge capacities between $200 - 250$ mAh g^{-1}; this is significantly higher than the theoretical capacity of Ni$^{2+/4+}$ ($128 - 195$ mAh g^{-1}).[74] Armstrong et al. demonstrated the loss of O$_2$ during charge, suggesting lattice oxygen may be oxidized.[75] Yabuuchi et. al. even more thoroughly described oxygen loss, or removal of Li$_2$O, and detailed the mechanism of its possible reduction by formation of a superoxide and Li$_2$CO$_3$.[70]

In the present paper we aim to correlate the degree of Mn activity within the Li-excess material Li[Li$_{2/12}$Ni$_{3/12}$Mn$_{7/12}$]O$_2$ with different morphologies and surface areas. We also aim to elucidate how changes in Mn valence relate to the possible redox of oxygen in the bulk and at the surface – the latter of which has been associated with electrolyte decomposition.[76] To do so, we synthesized the electrode material following three different precursor methods. All were solution-based and include: 1) sol-gel, "SG"; 2) hydroxide co-precipitation, "HCP"; and 3) carbonate co-precipitation, "CCP". The natures of these methods are quite different from one another, as the intermediates formed during their preparation are distinct. Several groups have compared materials produced from a given reaction by altering a narrow parameter – for instance, by

comparing different calcination temperatures of sol-gel synthesized material,[77] different concentrations of chelating agent in a carbonate co-precipitation method,[78] or by adjusting the pH in a hydroxide co-precipitation procedure.[79] Those results show that even for a given synthetic method, the physical and electrochemical properties of a material can differ appreciably. We offer a comparison across fundamentally different synthetic approaches, in order to highlight materials possessing consistent phase and stoichiometry, but very different surface compositions and morphologies. Understanding these differences enables us to elucidate the role of Mn in the reaction mechanism during cycling and predict ways to optimize the electrode properties.

3.2 Experimental

3.2.1 Sol-gel synthesis

All synthesis routes employed deionized water from a Millipore ICW-3000 system (18MΩ-cm resistivity). Sol-gel (SG) synthesis was adapted using aqueous methods previously described for similar transition metal oxides.[80] Reagents consisted of lithium acetate – $Li(CH_3COO)$ $2H_2O$ (99.999%, Sigma-Aldrich), nickel acetate – $Ni(CH_3COO)_2$ $4H_2O$ (99+%, Acros Organics), and manganese acetate – $Mn(CH_3COO)_2$ $4H_2O$ (99+%, Acros Organics). Stoichiometric concentrations of each metal acetate, $^{14}/_{12}$:$^{3}/_{12}$:$^{7}/_{12}$ Li:Ni:Mn, were dissolved in separate beakers containing a 1:1 mole ratio of citric acid (99%, Acros Organics), which served as the chelating agent. An extra 5mol% Li-acetate was added to its beaker, to account for Li-loss during calcination. The concentrations of Li- Ni- & Mn-acetates were kept just below their water solubility

limits, 408 g L^{-1}, 182 g L^{-1}, and 773 g L^{-1}, respectively. Ni- & Mn-solutions were dripped into a reaction flask, heated to 60˚C using a water bath. The pH of the reaction flask was brought to 7 by slowly adding ammonium hydroxide, NH$_4$OH (25%, Acros Organics). The metal polymerization reaction was controlled by separately dripping both Li-acetate and NH$_4$OH into the reaction flask at a rate necessary to maintain a pH of 7. After roughly 6 hrs, the light green sol turned into a dark green gel, which was dried in vacuum at 120°C for 24hrs. The dried gel was ground and subject to pre-calcination at 450°C for 12 hours, using 2°C/min heating rates. The recovered powder was finely ground, compressed into pellets, and calcined at 900°C for 9 hours, at 2°C/min heating rates. These pellets were furnace-cooled, i.e. brought to room temperature within the furnace by turning off heat and waiting for room temperature to be reached naturally. After being ground, the sample served as the final SG product.

3.2.2 Hydroxide co-precipitation synthesis

The hydroxide co-precipitation (HCP) method was followed directly from Fell et. al.[74] Double hydroxide precursor was prepared from transition metal reagents, nickel (II) nitrate – Ni(NO$_3$)$_2$ 6H$_2$O (99%, Acros Organics) and manganese (II) nitrate – Mn(NO$_3$)$_2$ 4H$_2$O (99%, Acros Organics). Ni- & Mn-nitrates were dissolved in water at a mole ratio of 3:7 and concentration of ca. 0.27:0.62M, respectively. This metal nitrate solution was slowly dripped, over the course of 2.5hrs, into a basic solution containing 0.23M lithium hydroxide, LiOH H$_2$O (98%, Sigma-Aldrich). The concentration of LiOH was chosen in mole ratio of 2.1:1, with respect to the desired Ni$_{3/10}$Mn$_{7/10}$(OH)$_2$ double hydroxide. The reaction was allowed to age for 3 hours after all reagents were

combined. The pH of this reaction was not controlled beyond start conditions. Additionally, this reaction took place at room temperature. The precipitate was filtered, rinsed with water, and dried in air for 10hrs at 180°C. After drying, a stoichiometric amount of LiOH ($^{14}/_{12}$:$^{10}/_{12}$ LiOH to $Ni_{3/10}Mn_{7/10}(OH)_2$) was ground into the precipitate. This ground powder was subject to pre-calcination at 480°C for 12 hours, using a 5°C/min ramp rate. The powder was ground, compressed into pellets, and calcined at 900°C for 12 hours, at a 5°C/min ramp rate. These pellets were furnace cooled and ground, serving as the final HCP product.

3.2.3 Carbonate co-precipitation synthesis

Carbonate co-precipitation (CCP) method was drawn from Zhang et. al.[81] and Wang et. al.[82] CCP precursor was prepared from nickel (II) sulfate – $NiSO_4 \cdot 6H_2O$ (99%, Sigma-Aldrich) and manganese (II) sulfate – $MnSO_4 \cdot H_2O$ (99%, Sigma-Aldrich). Ni- & Mn sulfates were dissolved in water at a mole ratio 3:7 and concentration of 0.21:0.48M, respectively. A second solution composed of sodium carbonate – Na_2CO_3 (99.5% Sigma-Aldrich), in 1:1 mole ratio with Ni & Mn, and 0.3M NH_4OH, was also prepared. Both solutions were slowly dripped, over the course of 3.0hrs, into a reaction flask heated to 60˚C using a water bath. The relative rates of each solution were combined so that a pH of 7.5 was maintained. The reaction was stirred for 12 hours after all reagents were combined. The $Ni_{3/10}Mn_{7/10}CO_3$ precipitate was filtered, washed with water, and dried under vacuum at 80°C for 24hrs. After drying, a stoichiometric amount of LiOH ($^{14}/_{12}$:$^{10}/_{12}$ LiOH to $Ni_{3/10}Mn_{7/10}CO_3$) was ground into the precipitate. This ground powder was subject to a pre-calcination at 600°C for 15 hours, using a 5°C/min ramp rate. The

powder was again ground, compressed into pellets, and calcined at 900°C for 15 hours, at a 5°C/min ramp rate. Once furnace cooled, these ground pellets served as the final CCP product.

3.2.4 Bulk characterization

Calcination temperatures were based upon mass-loss profiles, generated using thermogravimetric and differential thermal analysis, via a Perkin-Elmer Diamond TG/DTA instrument. The particle morphology of pristine Li-excess was determined using a Philips XL30 environmental scanning electron microscope (ESEM), with an accelerating voltage of 20 kV. The crystal structure of materials was identified by X-ray diffraction (XRD), acquired using a Bruker D8 advance diffractometer with a Bragg-Brentano θ-2θ geometry and a Cu Kα source (λ = 1.54 Å). Samples were scanned from 10° to 80° at a scan rate of $0.025°$ s^{-1}. Rietveld refinement was performed using FullProf software.[83] Both inductively coupled plasma –mass spectrometry & –optical emission spectroscopy were used to determine the stoichiometry of Li, Ni, and Mn in the synthesized materials. ICP-MS was performed using a Thermo Finnigan Element 2 plasma mass spectrometer, while ICP-OES was performed using a PerkinElmer 3700 optical emission plasma spectrometer. ICP-MS Li, Ni, and Mn standards consisted of 1 mg mL^{-1} in 2% HCl, Acros Organics. Nitrogen physisorption was used to determine surface areas by incorporating the Brunauer-Emmett-Teller (BET) method. Measurements were performed using a Quantachrome Instruments Autosorb 1C physisorption analyzer. Approximately 1 grams of material was dried at 300°C under vacuum for 4 hours prior to BET measurements.

3.2.5 Electrochemical characterization

Electrochemical properties were measured using Li-excess composite cathodes assembled into 2016 coin cells. Composite electrodes consisted of Li[Li$_{2/12}$Ni$_{3/12}$Mn$_{7/12}$]O$_2$ active material, acetylene carbon black, and polyvinylidene fluoride (PVDF), in weight ratio of 80:10:10, respectively. Slurries were prepared by extensively mixing the three components in 1-methyl-2-pyrrolidone (NMP, 99% extra pure, Acros Organics). Slurries were cast on Al-foil using a doctor blade and dried in vacuum at 80˚C for 12hrs. Disc electrodes, 1 cm^2, were punched out and dried again for 6hrs (in air) before being brought into an Ar-filled glove box (O$_2$,H$_2$O < 1 ppm). The mass of active material cast was between 4 and 5 mg. Li-metal discs were used as anode and 1M LiPF$_6$ in ethylene carbonate and dimethyl carbonate, EC:DMC in 1:1vol ratio, was used as electrolyte (3-4 drops from a 3mL plastic transfer pipette). Two sheets of Celgard polymer film (C480, Celgard Inc.) were used as separator. The added thickness of an extra sheet provides improved electrochemical stability.

Coin cells were allowed to rest and equilibrate for 1.5 hrs before electrochemical tests were performed. Galvanostatic experiments were carried out using an Arbin BT2000 battery testing system. The voltage range was maintained between 2.0 – 4.8 V. C-rates were calculated by assuming a theoretical specific capacity of 250 mAh g^{-1}; more regarding the theoretical capacity is described in the results and discussion below. Cycling was conducted at constant current charge and discharge rates of C/20. Rate studies were performed by charging at C/20 to 4.8V and subsequently discharging at C/20, C/10, C/5, C/2, or 1C to 2.0V. In order to avoid contributions from capacity fade upon cycling, only the first discharge capacity at each rate is reported.

3.2.6 Surface characterization

The chemical compositions of Li-excess composite electrode surfaces were analyzed before and after cycling, using X-ray photoelectron spectroscopy (XPS). Cathodes measured before cycling were assembled into coin cells and exposed to electrolyte for 2-3 days prior to analysis. These soaked cathodes are referred to as "0 cycles" in the analysis and figures that follow. Cycled samples were charged and discharged 10 times, at a rate of C/20. All samples were measured in the discharge state. Cells were disassembled in an Ar-filled glove box, with precaution not to short them. Cathodes were rinsed several times with DMC, and once dry, were loaded into a custom airtight chamber for direct transfer into the spectrometer; samples were never exposed to air. The XPS chamber was maintained at $< 10^{-8}$ Torr during measurement. A PHI 3056 spectrometer possessing a hemispherical detector 54.7° off normal and dual Mg and Al anode source, operating at 15 kV and 350 W, was used for all analyses. High-resolution scans of the Ni2p region are reported using the Mg source; all other regions were derived from the Al source. High-resolution scans were acquired using pass energy of 23.5 eV and a step size of either 0.05 or 0.075eV. Each high-resolution scan was preceded by a high resolution C1s scan, to account for charge build up. The main C1s peak was calibrated to carbon black, 284.6 eV, as was the following high resolution scan. Peaks were deconvoluted using Gaussian-Lorentzian line shapes and Shirley background subtractions, using CasaXPS processing software.

3.3 Results and discussion

3.3.1 Bulk characterization

There are dramatic differences in each material's energy and reaction steps, as the TG/DTA data show in Figure 3.1, indicating significantly different processes occurring during $Li[Li_{2/12}Ni_{3/12}Mn_{7/12}]O_2$ formation. For example, between 200°C and 400°C, about 80% by mass of gel synthesized via SG was lost. This drastic mass-loss is due to the high concentration of large molar mass reagents such as acetate anion and citric acid, which are evaporated in that respective order. There is a large exothermic peak associated with these two mass-loss events, Figure 3.1a. In comparison there is only a 5% mass loss for the HCP precursor after the initial loss of H_2O (<100 ^{o}C). This reflects the fact that the elemental composition of precursor is very similar to the final Li-excess layered product. The XRD pattern of this precursor, Figure 3.2a, shows that it is primarily composed of spinel, similar to Mn_3O_4. This is consistent with results from Zhao et. al. who showed that as x decreases in $Ni_xMn_{1-x}(OH)_2$, particularly when $x < \frac{1}{2}$, the structure of dried precursor adopts a spinel phase.[83] The TG/DTA data collected for the CCP precursor mixed with stoichiometric LiOH shows a larger mass-loss event after H_2O removal, relative to HCP precursor, Figure 3.1c. This event, between 300°C and 400°C, is due to reaction and removal of the CCP precursor's carbonate moiety. Another possible contribution may be due to incorporated reagent salts, which have greater molar mass for CCP compared to HCP, $-SO_4$ vs $-NO_3$, respectively. XRD data collected for CCP precursor, Figure 3.2b, shows its phase corresponds well with trigonal ($R\overline{3}c$) $MnCO_3$. This is consistent with results reported by Wang et. al.[84]

Despite undergoing markedly different phase transformations, the final crystal

structure of SG, HCP, and CCP products were quite similar to one another. Figure 3.3 shows that after calcination, each material can be indexed to the hexagonal crystal system α-NaFeO$_2$. The peak separation and shape of 006/012 and 018/110 reflections, highlighted in Figure 3.3, indicate the formation of well-ordered layered structure.[81] Though the major reflections are routinely associated with rhombohedral LiMO$_2$ (M = Ni, Co, Mn, Cr, etc.) structure, space group R$\overline{3}$m, this cannot account for the small peaks observed between 20 – 30° 2θ. This region has been commonly attributed to Li and Mn/Ni ordering of √3a x √3a superstructure within the transition metal layers. Proponents of the two-component system suggest these reflections arise from discrete domains of Li$_2$MnO$_3$ possessing C2/m symmetry;[85] those Miller indices are highlighted in the enlarged insets of Figure 3.2a.   Regardless of its fundamental composition, Figure 3.3 shows that through the use of standard XRD, no difference between SG, HCP, and CCP products can be detected. All peak positions are well aligned and their relative intensities are quite similar.

Table 3.1 confirms that qualitative interpretation of the similarity in these XRD spectra are supported quantitatively by Rietveld refinement. The *a*- and *c*-lattice parameters for each material were determined to be within 0.1% of one another. The refined doping of Ni^{2+} on the Li$^+$ site (3a) were similar, 4.2%, 3.5%, and 3.6% for the SG, HCP, and CCP materials, respectively. Since XRD were fit to space group R$\overline{3}$m, the region between 20.0° – 22.5° 2θ was excluded in order to reduce the conventional Rietveld R-factor, R$_{wp}$,. Bragg factors, R$_B$, were all below 7.

Despite their similar crystal structures, the three materials adopt significantly different morphologies. Figure 3.4a shows that SG product consists of a highly

homogenous network of nanoparticles, about 200nm in diameter. HCP product on the other hand (Figure 3.4b) is composed of irregular particle morphology. Though its primary particles typically have diameters around 250nm, its secondary morphology vastly ranges in shape and size. CCP material predominantly consists of spherical 4 – 5 μm secondary morphologies, which are composed of 400 – 500 nm primary particles. The morphological differences between SG, HCP, and CCP products led to quite different surface areas as well. Those values (Table 3.2) show that SG material had a surface area twice as large (17.33 m^2/g) as material produced from HCP and CCP methods (8.27 and 8.13 m^2/g, respectively). Experimentally determined stoichiometries of each material, Table 3.2, are the same as one another, and to the theoretically desired ratio of Li[$Li_{2/12}Ni_{3/12}Mn_{7/12}$]$O_2$. While XRD, Rietveld refinement, and ICP results suggest the crystallinity and stoichiometry of these materials are highly similar, their morphologies and surface areas are clearly not. These differences may, therefore, strongly correspond to electrochemical differences between the three compounds.
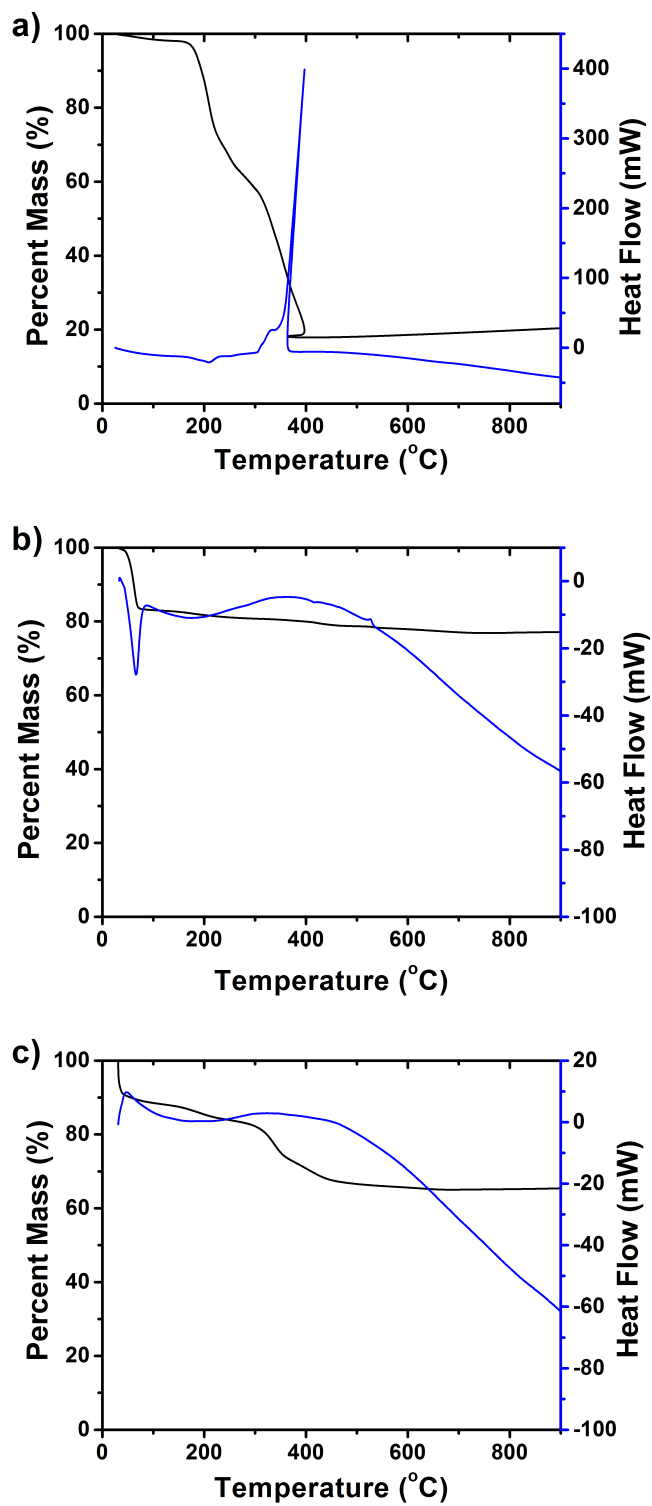
Figure 3.1 TG (left axes, black) and DTA (right axes, blue) curves of precursors synthesized by (a) SG, (b) HCP, and (c) CCP methods.
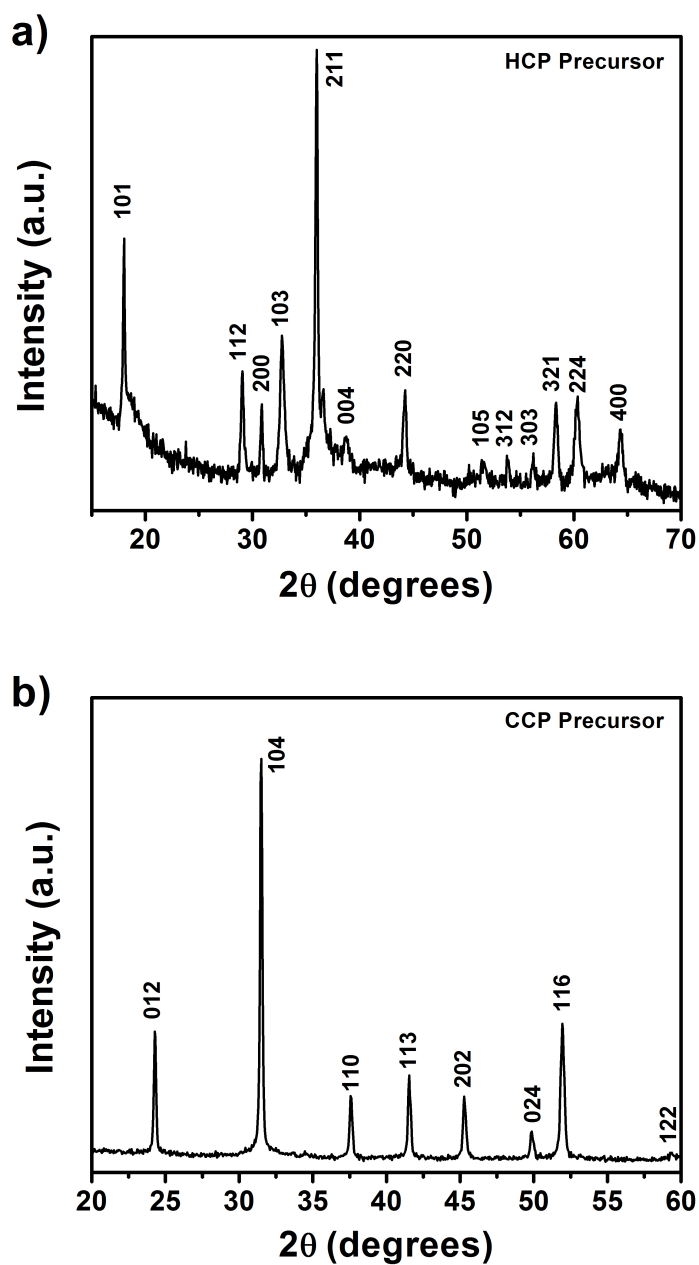
Figure 3.2 XRD patterns of (a) HCP and (b) CCP precursors, prior to calcination and Li-addition. HCP peaks indexed to I 41/a m d phase Mn_3O_4 and CCP peaks indexed to $R\overline{3}c$ phase $MnCO_3$.
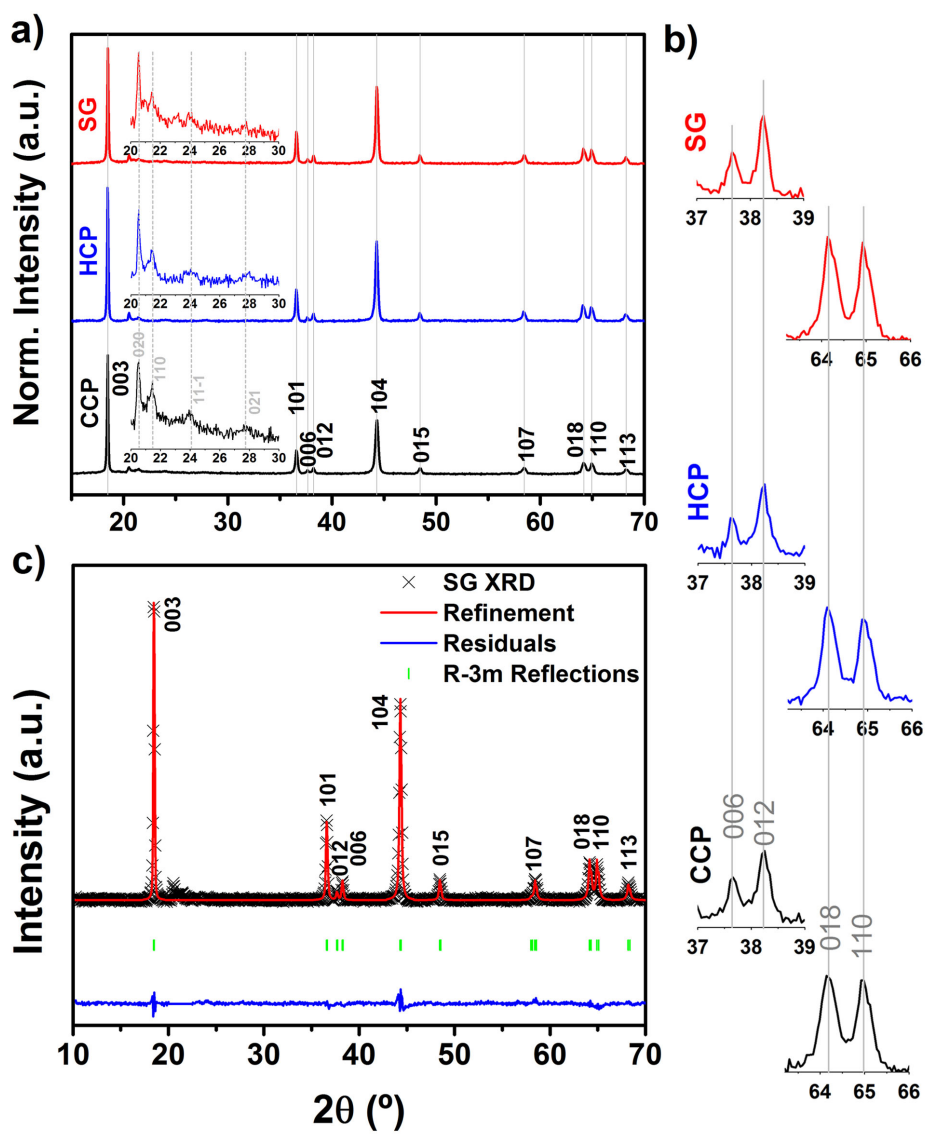
Figure 3.3 (a) Normalized XRD spectra of Li[Li$_{2/12}$Ni$_{3/12}$Mn$_{7/12}$]O$_2$ prepared by SG, HCP, and CCP methods. Solid and dotted gray lines correspond to R$\overline{3}$m and C2/m reflections, respectively. (b) Enhanced view showing separation and shape of each material's 006/012 and 018/110 peaks. (c) Representative Rietveld refinement of SG material fit to space group R$\overline{3}$m.
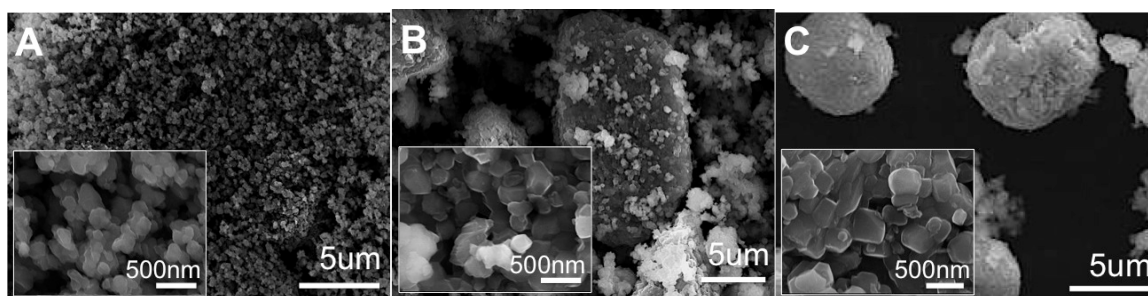
Figure 3.4. SEM images of Li[Li$_{2/12}$Ni$_{3/12}$Mn$_{7/12}$]O$_2$ prepared by (a) SG, (b) HCP, and (c) CCP methods.

Table 3.1 Rietveld fit parameters of Li[Li$_{2/12}$Ni$_{3/12}$Mn$_{7/12}$]O$_2$ prepared by SG, HCP, and CCP methods.

Material	*a (Å)*	*c (Å)*	*c/a*	*z(O)*	*n Ni in Li layer*	*R$_{wp}$*	*R$_B$*
SG	2.863(0)	14.255(2)	4.979	0.243(6)	0.04(2)	1.98	6.09
HCP	2.859(8)	14.255(8)	4.985	0.242(6)	0.03(5)	2.16	6.47
CCP	2.861(5)	14.253(9)	4.981	0.243(6)	0.03(6)	2.40	5.47

Table 3.2 Surface area and stoichiometry of Li[Li$_{2/12}$Ni$_{3/12}$Mn$_{7/12}$]O$_2$ determined by BET analysis and ICP-OES/MS, respectively.

Material		Stoichiometry	
	Surface Area (m^2 g^{-1})	*Mn:Ni*	*Li:(Mn+Ni)*
Theoretical		2.33	1.40
SG	17.33	2.3(5)	1.4(1)
HCP	8.27	2.3(7)	1.4(8)
CCP	8.13	2.3(3)	1.4(5)

3.3.2 Electrochemical characterization

The first cycle voltage profiles of $Li[Li_{2/12}Ni_{3/12}Mn_{7/12}]O_2$ prepared by SG, HCP, and CCP methods are compared in Figure 3.5a. All charge potentials consist of an initial sloping region, followed by a plateau at about 4.5V vs Li/Li^+. The inset of differential capacity, dQ/dV, highlights the plateau at this potential (largest peak). The first region has been commonly ascribed to the oxidation of Ni^{2+} to Ni^{4+}, while the origin of the plateau has been the subject of much greater debate.[86] Mn^{4+} present in the pristine compound is not thought to undergo oxidation to higher valence states.[87] The high capacities of layered Li-excess are not possible by redox of Ni alone, however, so an O^{2-}/O_2 or O^{2-}/O^- redox couple has been proposed to account for the additional capacity.[75] Theoretical capacity from the removal of 100% Li^+ within the pristine structure is 360.1 mAh g^{-1}. Figure 3.5a shows that SG material nearly reaches this capacity, but suffers from high retention loss as a consequence – exhibiting first charge and discharge capacities of 358.5 and 257.9 mAh g^{-1}, respectively. CCP material could accommodate less charge capacity, but delivered a nearly equivalent discharge capacity, resulting in much higher Coulombic efficiency overall. While the charge capacity of HCP material was nearly equal to that of CCP, its discharge capacity was much lower, resulting in the lowest among the three.

In order to pinpoint which reactions are responsible for these differences, we first define them more explicitly. As mentioned previously, the initial charge proceeds by Ni oxidation (up to 4.5V). Using solid-solution notation the following may be used to describe *reaction 1*:

$$Li[Li_{2/12}Ni^{2+}_{3/12}Mn^{4+}_{7/12}]O_2 \rightarrow Li_{1/2}[Li_{2/12}Ni^{4+}_{3/12}Mn^{4+}_{7/12}]O_2 + 0.5Li^+ + 0.5e^- \qquad (1)$$
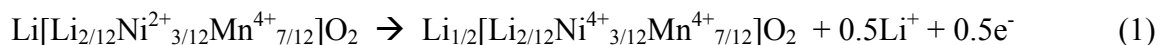
This step yields a theoretical capacity of 154.3 mAh g^{-1}. Deintercalation of all remaining Li results in a theoretical capacity of 205.8 mAh g^{-1}. If we assume that this second step proceeds by oxidation of O^{2-} to O_2, not excluding the possibility that O^{2-} oxidizes to O^- as an intermediate species, then *reaction 2* may be written:

$$Li_{1/2}[Li_{2/12}Ni^{4+}_{3/12}Mn^{4+}_{7/12}]O_2 \rightarrow Ni_{3/12}Mn_{7/12}O_{2-(0.34)} + 0.67Li^+ + 0.67e^- + 0.17O_2 \qquad (2)$$
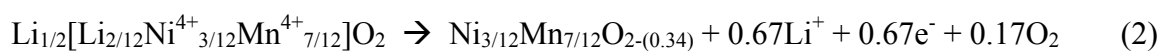
The theoretical capacities of each reaction are depicted by dotted lines in Figure 3.5b. Figure 3.5b provides an analysis of each material's first cycle capacity in terms of the specific reactions contributing to them. The experimentally determined capacity resulting from Ni-redox in reaction *1* is taken to be the capacity up to the local minimum voltage of the dQ/dV plot, 4.38V, preceding the plateau peak. The remaining capacity is attributed to reaction *2*, plotted as the upper bar in Figure 3.5b. Therefore the capacity from reaction *2* corresponds to 205.1, 155.7, and 187.3 mAh g^{-1} for SG, HCP, and CCP materials, respectively. Recalling the morphology of each, the length of plateau or degree of reaction *2* was greatest when particle size and surface area was smallest, in SG. When very large particles were present, as in HCP, reaction *2* was inhibited, compared to reaction *1*.

While the distinctions between reactions *1 & 2* are quite obvious in the 1st charge they are not as evident during discharge. Three peaks are observed in the dQ/dV discharge profile (inset), implying several unique reduction reactions occur. XAS studies

of Li-excess by Park et al. indicates that by 3.6V during the discharge, the Ni^{4+} has already been completely reduced to Ni^{2+}.[68] Discharge capacity of pure $LiNi_{0.5}Mn_{0.5}O_2$, by reduction of Ni^{4+} to Ni^{2+}, is not typically observed below 3.6V, as well. Due to this significance, we differentiate discharge capacity occurring above and below the inflection near 3.6V, by the lower and upper blue bars in Figure 3.5b, respectively. Reduction of a species besides Ni^{4+} must occur above this voltage, however, because it is possible for the discharge capacity above 3.6V to be greater than the charge capacity resulting from reaction *1*. For example, CCP material exhibited 115.2 mAh g^{-1} prior to the 4.5V charge plateau, but 140.6 mAh g^{-1} prior to 3.6V upon discharge. We therefore designate the lower blue bar in Figure 3b as originating from products formed by *reactions 1* and *2* (Rxn 1' & 2'), while the upper blue bar results solely from reduction of *reaction 2* products (Rxn 2').

Figure 3.6 demonstrates changes in capacity and voltage during the initial 10 cycles of each material. It is clear from this figure that SG material experiences the worst capacity fading, followed by CCP and then HCP. Figure 3.6d differentiates the two discharge regimes during the first 10 cycles. It shows that all the capacity fade occurs before the inflection around 3.6V. Below this voltage, the capacity actually increases, which is more explicitly demonstrated in Figure 3.7. The position of the inflection also changes, which is demonstrated by the shift in the lowest voltage dQ/dV peak to even lower values. The first two dQ/dV peaks, near 4.30V and 3.75V, do not shift appreciably – reflecting the fact that there is almost no voltage drop in the 1st discharge region. The entire voltage drop is present in the 2nd, low voltage regime. The degree of this drop is highlighted (gold) in Figure 4d, and was 105, 50, and 130mV for SG, HCP, and CCP

materials, respectively. The amount of voltage fading for SG was twice that of HCP, therefore, and for CCP was nearly three times that of HCP. The decrease in voltage is proportional to the magnitude in capacity of the second region. CCP material exhibited the highest capacity in the second region, followed by SG and then HCP materials. In other words, the larger the discharge capacity below 3.6V, the greater was the voltage drop. This suggests that product generated in *reaction 2* is responsible for voltage fading in this material.

Figure 3.8 compares the overall capacity retention and Coulombic efficiency of each material. It is shown that CCP material exhibits the best overall retention and efficiency. Among the three materials, it also shows the highest proportion of low voltage capacity. Reduction of electrolyte to Li_2CO_3 may partially contribute to this discharge capacity, as is further described below. Though there is some degree of capacity fading within the Ni-redox regime, the comparatively large activation of *reaction 2* components leads to much higher retention and Coulombic efficiencies. SG material, on the other hand, allows for higher overall charge capacities, but worse fading and efficiency. While SG nanoparticles may lead to relatively poor cyclability, its first discharge rate capability is still superior to larger particles, as shown by Figure 3.8.
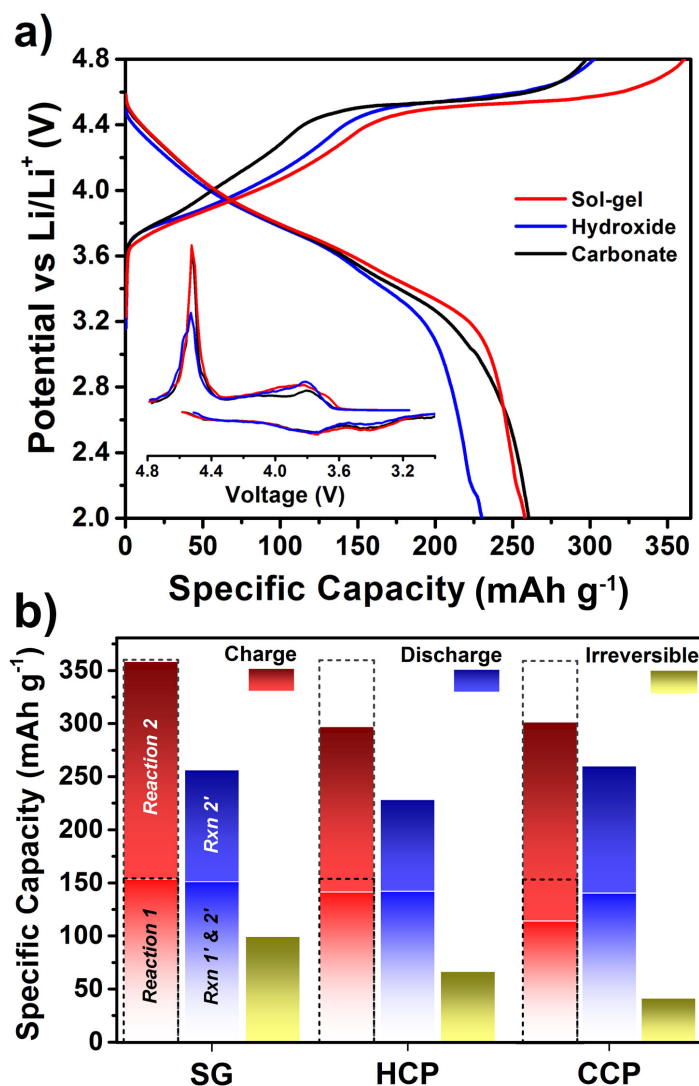
Figure 3.5 First cycle electrochemical performance of Li[Li$_{2/12}$Ni$_{3/12}$Mn$_{7/12}$]O$_2$ (a) First cycle voltage profiles of Li[Li$_{2/12}$Ni$_{3/12}$Mn$_{7/12}$]O$_2$ prepared by SG, HCP, and CCP methods; inset represents dQ/dV (y-axis) of those same profiles. (b) Breakdown of each material's first cycle capacity; bottom and top dotted regions of each bar correspond to theoretical capacities possible from reactions described in text.
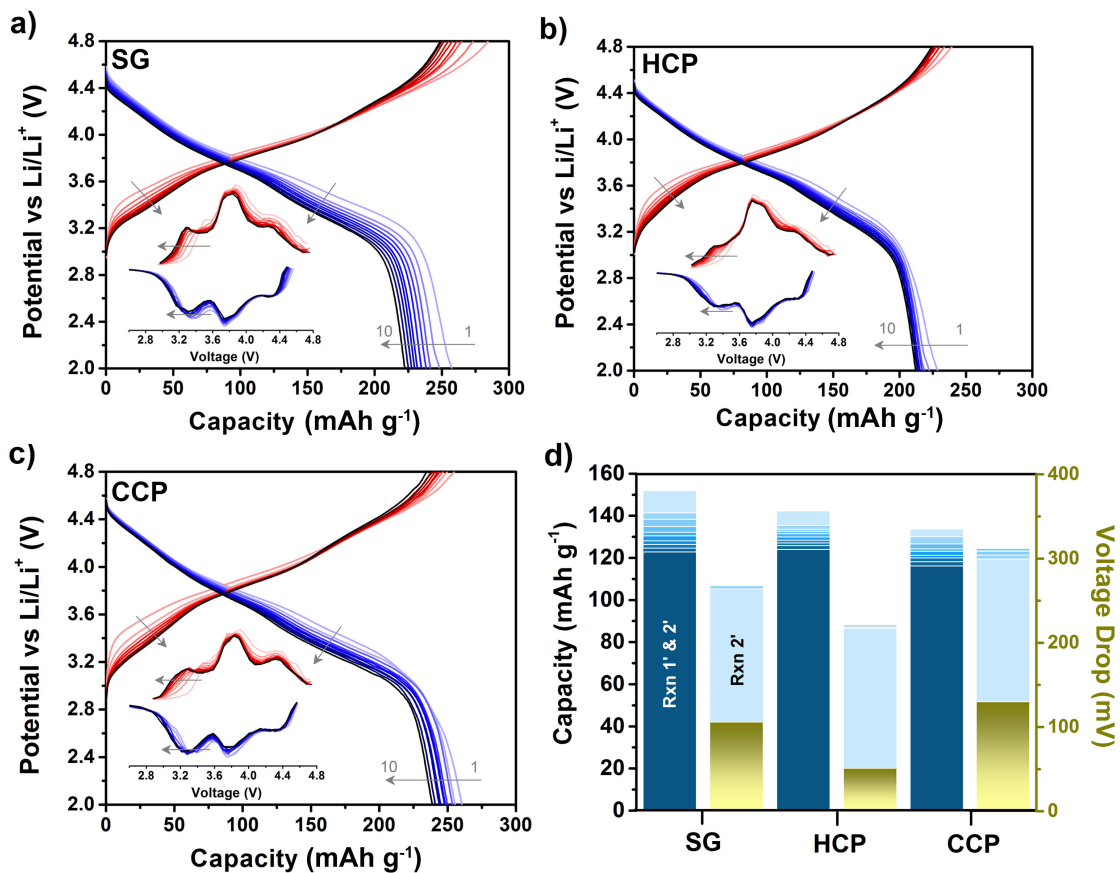
Figure 3.6. First 10 electrochemical profiles (minus 1st charge) of Li[Li$_{2/12}$Ni$_{3/12}$Mn$_{7/12}$]O$_2$ prepared by (a) SG, (b) HCP, and (c) CCP methods; insets represent dQ/dV (y-axis) of those same profiles. Arrows indicate increasing cycle number, from light to dark shading. (d) First 10 discharge capacities, with same color scheme (i.e. 1st discharge, lightest blue and 10th discharge, darkest blue), broken down by capacity contributing above (Rxn 1' & 2') and below (Rxn 2') the ~3.6V inflection point; right axis (gold) corresponds to voltage drop within each specific regime.
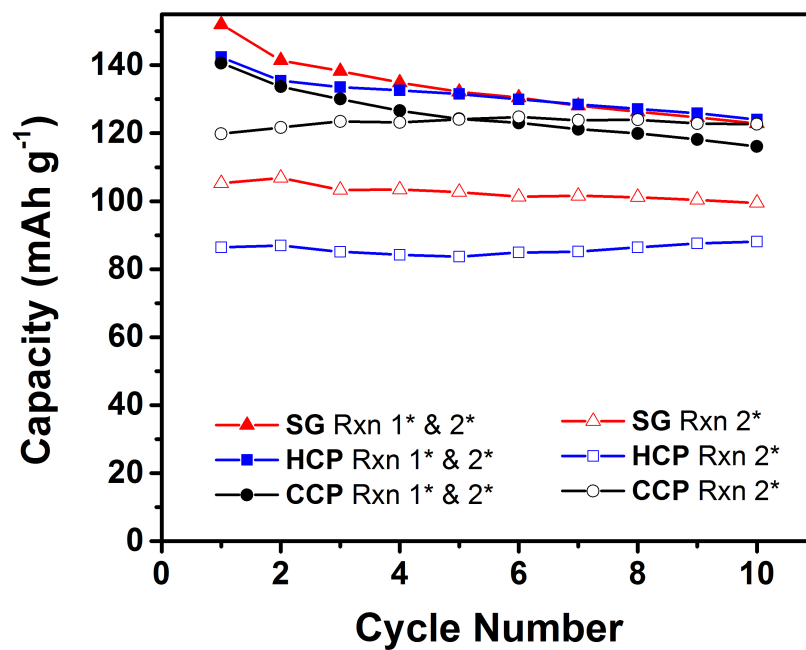
Figure 3.7 First 10 cycle discharge capacities of Li[Li$_{2/12}$Ni$_{3/12}$Mn$_{7/12}$]O$_2$ prepared by SG, HCP, and CCP methods. Capacities separated by the voltage inflection ~3.6V vs Li/Li$^+$, referred to within inset as "Rxn 1* & 2*" (above ~3.6V) and "Rxn 2*" (below ~3.6V).
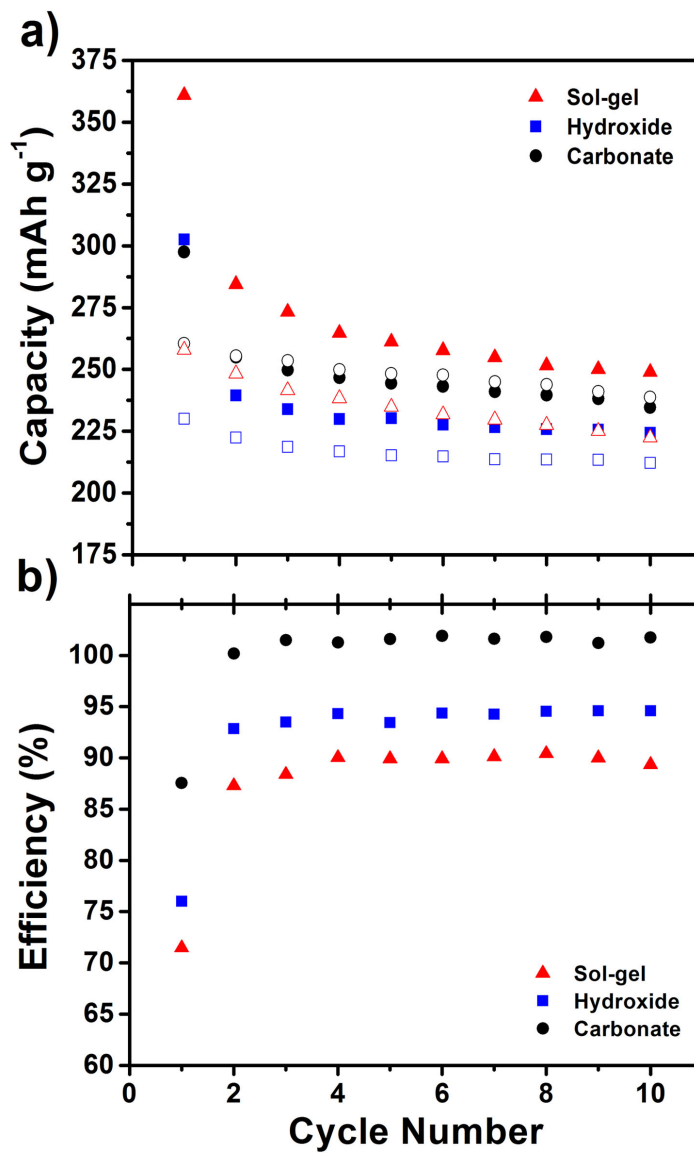
Figure 3.8 Retention and efficiency of Li[Li$_{2/12}$Ni$_{3/12}$Mn$_{7/12}$]O$_2$. (a) Charge (solid symbols) and discharge (open symbols) capacity retention of Li[Li$_{2/12}$Ni$_{3/12}$Mn$_{7/12}$]O$_2$ prepared by SG, HCP, and CCP methods, over the first 10 cycles. (b) Coulombic efficiency of each material over the course of the same 10 cycles.

3.3.3 Surface characterization

The surface of each material was analyzed before and after 10 cycles using XPS, without exposure to air, as described in the experimental section above. Figure 3.9 shows that the C1s spectra of all materials are largely dominated by carbon black, at 284.6 eV. Before cycling, contributions from -CH$_2$- polymer in PVDF binder at 285.7 eV are clearly defined. After 10 cycles, however, the peak is broadened by the formation of C-O (286 eV), C=O (287.7 eV), and C-H (284.9 eV) species, formed due to reaction with electrolyte.[88] The peak at highest binding energy, 290.5 eV, is associated with C-F in PVDF. It likely broadens upon cycling due to the formation of Li$_2$CO$_3$ (290.0 eV) upon discharge.[89] Even before cycling, this peak is relatively broad for the HCP material, which may be due to interaction between the active material and PVDF. Li on the surface of LiNi$_{0.5}$Mn$_{0.5}$O$_2$ has been shown to interact with PVDF to form LiF.[90] This is supported by the F1s spectra of Figure 3.10, which shows that its intensity of LiF is relatively high, compared to PVDF.

Figure 3.11 shows each material's Mn3s regions. Galakhov et. al. demonstrated that splitting between the main Mn3s peak and its satellite are highly sensitive to the Mn valence state – in general, the larger the splitting, the lower its oxidation state.[91] Splitting of transition metal 3s XPS spectra occurs due to exchange coupling between the 3s hole and 3d electrons. Analysis of this region is attractive because it is not subject to overall binding energy shifts, due to phenomena such as charge build up. The difference in binding energy between those peaks (ΔE) has been used to approximate the average Mn oxidation state (AOS) by the equation, AOS = $8.956 - 1.126 \Delta E$.[92] Figure 3.11 shows that the peak separations of SG, HCP, and CCP materials before cycling are identical to

one another. After 10 cycles, however, the splitting increases from HCP to SG and CCP. Those values, 4.87, 5.07, and 5.29 eV, correspond to average oxidation states of $Mn^{3.5+}$, $Mn^{3.2+}$, and Mn^{3+}, respectively. The Mn3p region shown in Figure 3.12 also supports this trend. Before cycling, the major peak comprised of both $Mn3p_{3/2}$ and $Mn3p_{1/2}$ are all in line with one another, and correspond to Mn^{4+}.[93] After 10 cycles, however, the peaks of HCP, SG, and CCP progressively shift to lower binding energy – the latter of which corresponds to Mn^{3+}.[93]

Figure 3.12 also highlights the Li1s region, which is composed of two distinct peaks. The one at lower binding energy (54.5 eV) is indexed to Li in $Li[Li_{2/12}Ni_{3/12}Mn_{7/12}]O_2$ lattice, while the higher binding energy peak (56.5 eV) is commonly associated with $LiPF_6$ electrolyte salt and LiF.[94] Shifts in the $LiPF_6$ peak to lower energies upon cycling indicates the generation of its decomposition products, such as $Li_xPF_yO_z$.[90] The fact that SG material shows this shift before cycling suggests its surface promotes these reactions, which could contribute to its poor Coulombic efficiency. CCP material on the other hand shows the smallest shift and exhibits the best cycling efficiency. The relative intensity of its Li1s peaks is the only among the three materials, which does not decrease significantly. This may be due to greater formation of Li_2CO_3 there, which the O1s XPS spectra in Figure 3.13 also support. The single peak found at 529.7 eV is indexed to $Li[Li_{2/12}Ni_{3/12}Mn_{7/12}]O_2$ lattice oxygen. The broad peak at higher binding energy is comprised of several oxygen-containing groups, however, including Li_2CO_3 at 532.2 eV.[70] Its intensity relative to lattice oxygen is shown to disproportionately increase in CCP material. Furthermore, it is slightly more shifted towards Li_2CO_3, than HCP and SG materials.

To summarize, Mn reduction is shown to occur to a larger extent in order of HCP, SG, and then CCP materials. Shifts in Mn2p XPS spectra due to valence state changes are notoriously subtle, which is why analysis of the Mn3p and Mn3s regions were performed.[95] Those small shifts in the Mn2p region are also shown, however, in Figure 3.14. A greater extent of Li_2CO_3 is formed in this same order as well; the O1s peak area containing Li_2CO_3 increases upon cycling by 8.1, 8.8, and 11.4%, in HCP, SG, and CCP materials, respectively. The relatively high degree of these reduction reactions in CCP material appears to also have influenced the valence of Ni. Figure 3.15 shows that the Ni2p peak of each material corresponds to Ni^{2+} before cycling. After 10 cycles, however, the $Ni2p_{3/2}$ and $Ni2p_{1/2}$ peaks are very slightly shifted to higher binding energy, suggesting that Ni at the surface may not have been fully reduced upon discharge. The Ni3p regions in Figure 3.16 also support the lack of full reduction.

Figure 3.9 XPS C1s regions of $Li[Li_{2/12}Ni_{3/12}Mn_{7/12}]O_2$ prepared by SG (bottom), HCP (middle), and CCP (top) methods, before (left) and after 10 cycles (right).
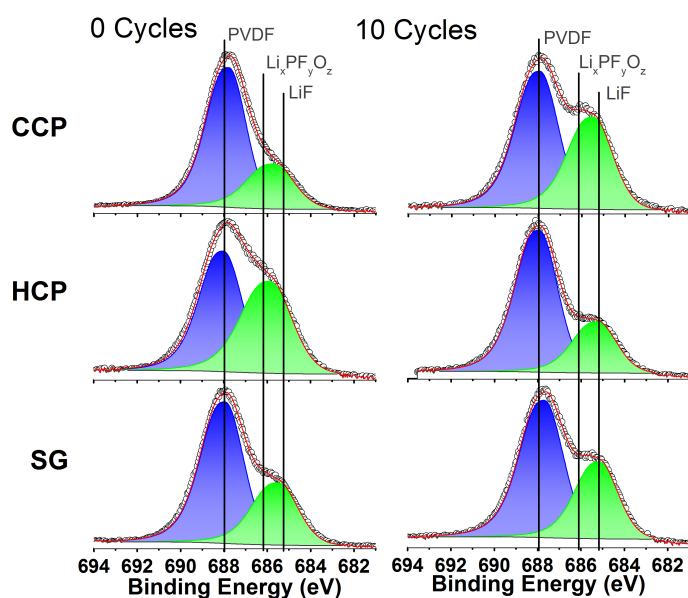
Figure 3.10 XPS F1s regions of Li[Li$_{2/12}$Ni$_{3/12}$Mn$_{7/12}$]O$_2$ prepared by SG (bottom), HCP (middle), and CCP (top) methods, before (left) and after 10 cycles (right).
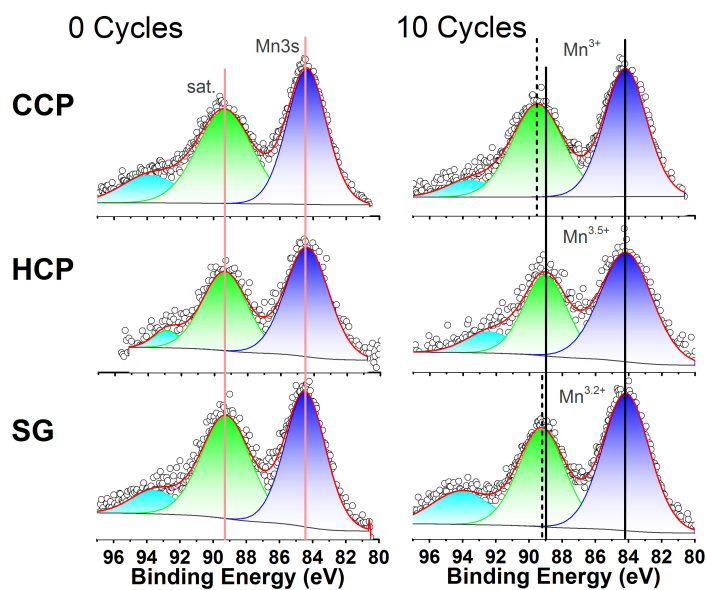
Figure 3.11 XPS Mn3s regions of Li[Li$_{2/12}$Ni$_{3/12}$Mn$_{7/12}$]O$_2$ prepared by SG (bottom), HCP (middle), and CCP (top) methods, before (left) and after 10 cycles (right). Cyan peak is a satellite due to final-state screening of the excited photoelectron.[96]
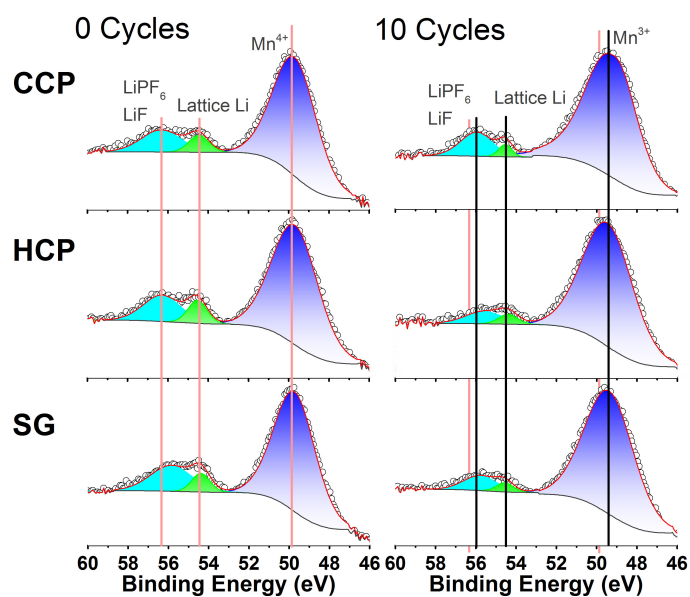
Figure 3.12 XPS Mn3p and Li1s regions of Li[Li$_{2/12}$Ni$_{3/12}$Mn$_{7/12}$]O$_2$ prepared by SG (bottom), HCP (middle), and CCP (top) methods, before (left) and after 10 cycles (right). Red line corresponds to peak positions before cycling.
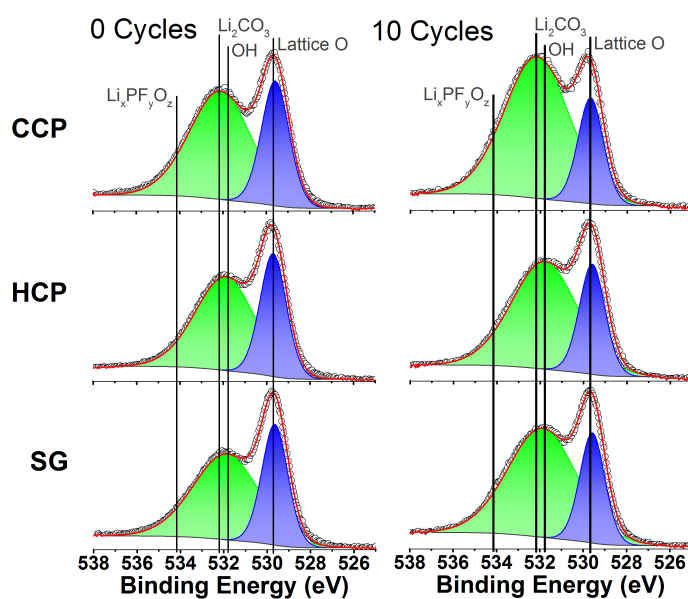
Figure 3.13 XPS O1s regions of Li[Li$_{2/12}$Ni$_{3/12}$Mn$_{7/12}$]O$_2$ prepared by SG (bottom), HCP (middle), and CCP (top) methods, before (left) and after 10 cycles (right).
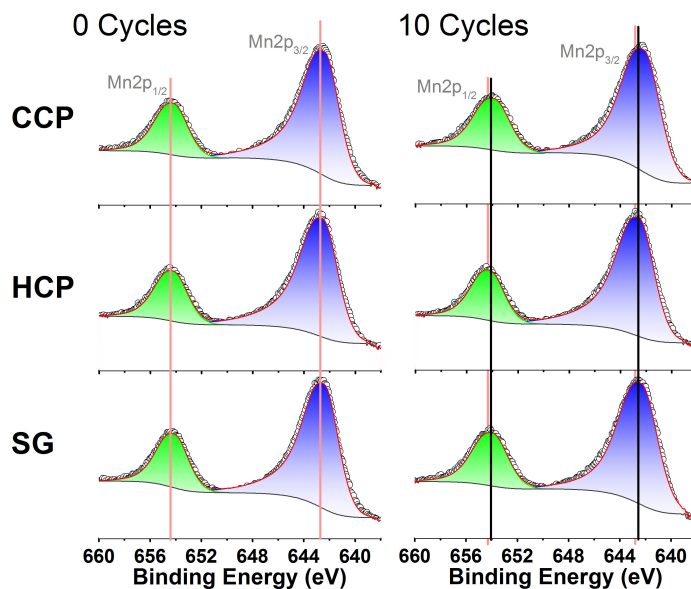
Figure 3.14 XPS Mn2p regions of Li[Li$_{2/12}$Ni$_{3/12}$Mn$_{7/12}$]O$_2$ prepared by SG (bottom), HCP (middle), and CCP (top) methods, before (left) and after 10 cycles (right).
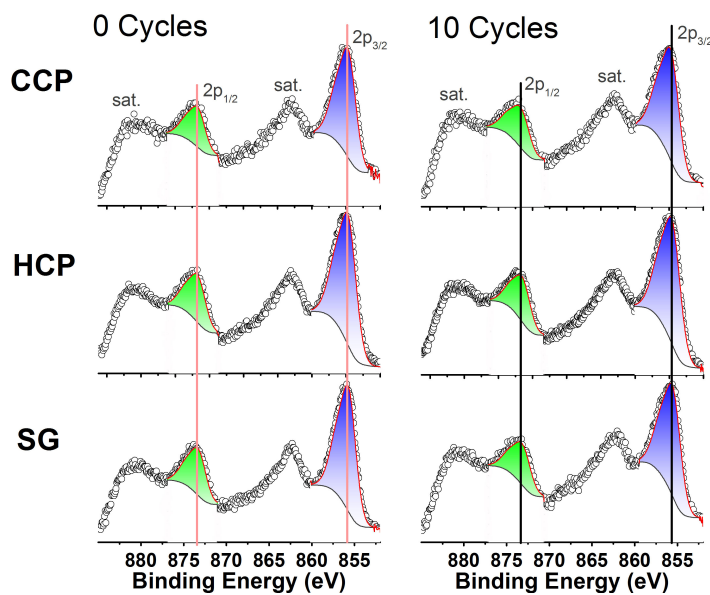
Figure 3.15 XPS Ni2p regions of Li[Li$_{2/12}$Ni$_{3/12}$Mn$_{7/12}$]O$_2$ prepared by SG (bottom), HCP (middle), and CCP (top) methods, before (left) and after 10 cycles (right).

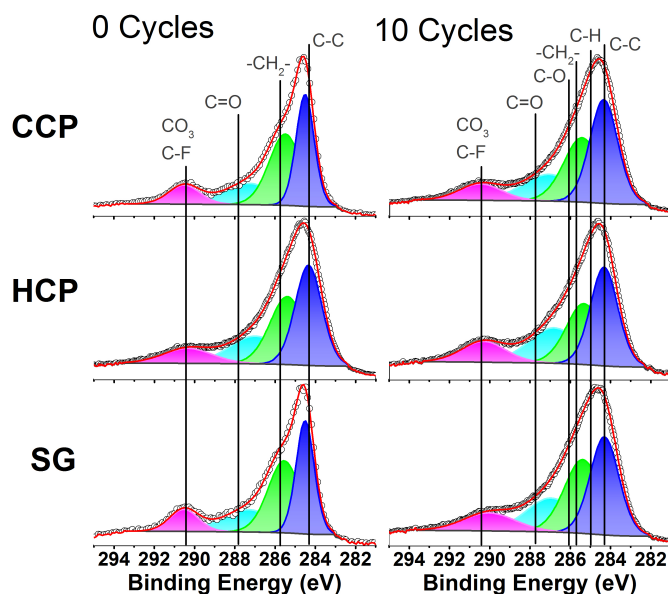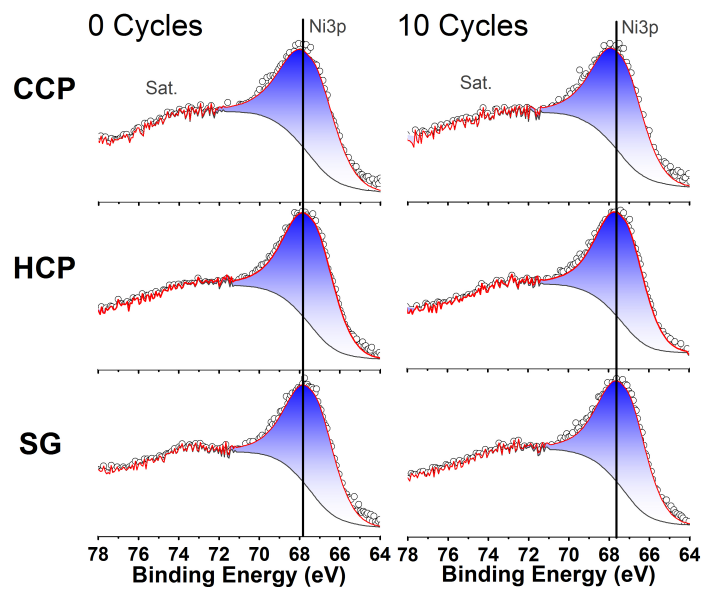**Figure 3.16** XPS Ni3p regions of Li[Li$_{2/12}$Ni$_{3/12}$Mn$_{7/12}$]O$_2$ prepared by SG (bottom), HCP (middle), and CCP (top) methods, before (left) and after 10 cycles (right).

3.3.4 Capacity and voltage fading

Oxygen evolution upon the initial charge was described in *reaction 2* to result in lattice oxygen vacancy. Owing to the high instability of MO_5 environments (M = Ni^{4+}, Mn^{4+}), however, Tran et. al. have proposed that oxygen loss may preferentially occur at the surface, followed by transition metal migration into Li-ion vacancies, which results in densification at the surface to maintain overall charge balance.[97] Filled Li sites prevent full Li-reintercalation upon discharge, thus contributing to the 1st cycle irreversible capacity. Xu et. al. has shown that the surface of Li-excess materials undergo structural rearrangement to a spinel-like phase and Fell et. al. described microstrain and cation rearrangement at the surface of these materials as well.[98-100] These results agree with the fact that SG synthesized material had the highest surface area, longest initial charge plateau, and worst 1st cycle irreversibility. The very large secondary particles distributed throughout the bulk of HCP material may have inhibited oxygen release, because of their comparatively low surface area. Its capacity was specifically low during the 4.5V charge plateau and below 3.6V during discharge.

Hong et. al. described the partially reversible formation and decomposition of Li_2CO_3 upon cycling Li-excess materials.[76] We demonstrate evidence for its formation in Figure 10 as well. Its generation has been associated with capacity fading, as is the case in the Li-air system.[101] Decomposition of Li_2CO_3 results in a series of reactions with the electrolyte to form CO_2 and H_2O among other species deleterious to Li-ion battery performance. Yabuuchi et. al. has shown that Li_2CO_3 is predominantly formed below 3.0V during the discharge of Li-excess.[70] We show in Figure 3.6, however, that capacity fading occurs prior to the 3.6V inflection during discharge. Since Ni is the predominant

redox species in this regime, we propose that changes in its environment are more likely responsible for capacity fading. This also agrees with the fact that SG had the highest surface area, which likely underwent the greatest degree of structural rearrangement, and exhibited the worst capacity fading among the three materials synthesized.

Since Figure 3.6 demonstrates that voltage fading primarily occurs below the 3.6V inflection during discharge, its origin may be more closely related to the redox process resulting from *reaction 2*, which did not involved Ni-redox. Koga et. al. have shown that O^{2-} anion, without removal from the lattice, may participate in the reversible redox of Li-excess materials.[102-103] Rana et. al. have shown that this is the case for pure Li_2MnO_3 as well.[104] While Li_2MnO_3 has been traditionally believed to be electrochemically inactive, several groups have recently demonstrated otherwise.[105-106] Sufficiently small particle sizes result in reversible capacities of ~180 mAh g^{-1}, after 30 cycles.[107] The electrochemical mechanism and voltage profile of Li_2MnO_3, including the initial voltage plateau and inflection near 3.6V during discharge, highly resembles that of Li-excess. Higher electrochemical testing temperatures have been shown to extend its discharge capacity, with concomitant release of CO_2.[108] Ohzuku et. al. has shown that increasing the temperature of Li-excess materials during cycling also extends its discharge capacity;[57] in particular, its capacity below 3.6V. $Li[Li_{1/5}Ni_{1/5}Mn_{3/5}]O_2$ was shown to achieve a discharge capacity of 350 mAh g^{-1} at 85°C, which is greater than its theoretical value (315.2 mAh g^{-1}) considering the full reduction of all Ni^{4+} to Ni^{2+} and Mn^{4+} to Mn^{3+}.

The XPS spectra shown in Figure 3.11 clearly demonstrate that Mn^{4+} is reduced at the surface of discharged Li-excess cathodes. Furthermore, the magnitude of its reduction is proportional to the degree of capacity that occurred below 3.6V during discharge.

Several groups have shown, however, that Mn reduction cannot fully account for the observed capacities and that an O^{2-} redox reaction clearly occurs. Oxygen radicals have been shown to react with carbonate-based electrolytes, such as EC, to form semi-reversible products such as Li_2CO_3.[76, 101] The C1s spectra in Figure 3.9, demonstrate the formation of electrolyte decomposition products by the presence of carbonate and ether groups. Furthermore, the O1s spectra in Figure 10 imply that more of these products, namely Li_2CO_3, are formed when larger discharge capacities and voltage fading below 3.6V are observed. Since the degree of electrolyte decomposition and Mn^{4+} reduction increase with larger voltage fade and capacities below 3.6V, it is likely that Mn^{4+} reduction is a result of reaction with electrolyte. In this way, $Mn^{4+/3+}$ may not be a truly redox active process that contributes to reversible capacity. Instead, Mn^{4+} reduction may be a deleterious reaction arising from the distinct interaction of the particle surface with electrolyte. As we have shown, a lower average valence of Mn at the surface corresponds to greater voltage decay. It is possible that Mn^{3+} disproportionation to Mn^{2+} and Mn^{4+} into electrolyte contributes to that fading.

3.4 Conclusions

Li-excess $Li[Li_{2/12}Ni_{3/12}Mn_{7/12}]O_2$ was prepared by three distinct synthetic approaches. Each method led to near identical bulk stoichiometry and crystallinity, as determined by ICP-MS and XRD. Their surface areas and particle morphologies were quite different, however, which in turn resulted in significantly different electrochemical characteristics. The relatively homogenous, micron-sized secondary particles of CCP material led to better Coulombic efficiency and enhanced discharge capacity below 3.6V.

The degree of Mn activity was shown to increase in order of HCP, SG, and CCP. XPS results specifically showed that Mn valence was reduced and a greater extent of Li_2CO_3 was formed in that same order. This suggests that Mn^{4+} reduction as well as electrolyte reduction is specifically associated with the voltage component below 3.6V in $Li[Li_{2/12}Ni_{3/12}Mn_{7/12}]O_2$. Insight is provided into how the activity of Mn is affected by $Li[Li_{2/12}Ni_{3/12}Mn_{7/12}]O_2$ possessing various surface compositions and morphologies. We distinguish the processes that may contribute to capacity and voltage fading based upon surface analyses. We show that optimization of the Li-excess surface is a crucial parameter in improving the electrochemical performance of this class of material.

Chapter 3, in full, is a reprint of the article, "Effect of Morphology and Manganese Valence on the Voltage Fade and Capacity Retention of $Li[Li_{2/12}Ni_{i3/12}Mn_{7/12}]O_2$," as it appears in ACS Applied Materials & Interfaces, Verde, M. G.; Liu, H.; Carroll, K. J.; Baggetto, L.; Veith, G. M.; Meng, Y. S., 2014, 6 (21), 18868-18877. The dissertation author was the primary investigator and author of this paper.

Chapter 4

Elucidating the Phase Transformation of $Li_4Ti_5O_{12}$ Lithiation at the Nanoscale Using c-AFM

This chapter describes a novel approach in the characterization of the lithium ion battery anode material, $Li_4Ti_5O_{12}$ (LTO). Lithium titanate's discharge (lithiation) and charge (delithiation) reactions are notoriously difficult to characterize due to the *zero-strain* transition occurring between its end members, $Li_4Ti_5O_{12}$ and $Li_7Ti_5O_{12}$. Interestingly, however, the latter compound is electronically conductive, while the former is not. We take advantage of this critical property difference by using conductive atomic force microscopy (c-AFM) to monitor the phase transition between the two structures at various states of charge. To do so, we perform ex-situ characterization on electrochemically cycled LTO thin-films that are never exposed to air. Our results quantify the extent of reaction between $Li_4Ti_5O_{12}$ and $Li_7Ti_5O_{12}$, at the nanoscale, during the first cycle. In addition, we provide direct confirmation of the manner in which the reaction occurs, which proceeds via percolation channels. We complement scanning probe analyses with an x-ray photoelectron spectroscopy (XPS) study that identifies and explains changes in the LTO surface structure and composition, which are observed upon cycling.

4.1 Introduction

Due to the demand for high energy density batteries for mobile electronics and electric vehicles, the quest for high capacity, low voltage anode materials – especially involving Si – has been heavily pursued in recent years.[109] In this respect, $Li_4Ti_5O_{12}$ (LTO) is viewed as an inferior lithium ion battery anode. It exhibits relatively low capacity and high voltage compared to the most commercially available Li-ion anode, graphite (175 vs 372 mAh·g^{-1} and 1.55 V vs ~100 mV Li/Li$^+$).[110] Nevertheless, the same properties resulting in undesirably low energy densities are attractive as well. The high redox potential of LTO lies safely within the electrolyte stability window.[87] This enables cycling without the formation of complex passivation layers, which are a problem for the long-term stability of conventional graphite anode and the popular alternatives such as silicon.[111] The two-phase reaction, which leads to moderate capacity, is also highly facile. It proceeds between two members ($Li_4Ti_5O_{12}$ and $Li_7Ti_5O_{12}$) that possess the same space group, Fd$\bar{3}$m. Even upon intercalation of 3 Li$^+$ per formula unit, there is only a 0.2% volume change, resulting in its description as a *zero-strain* material.[112] The stability, robustness, and safety of LTO have in fact led to its successful commercialization.

A shortcoming of LTO is its inherently low ionic diffusion and electronic conductivity.[113-114] $Li_4Ti_5O_{12}$ is considered to be an insulator, with experimentally reported band gaps typically between 3.0 and 4.0 eV.[115-116] In order to circumvent this problem, several strategies have been implemented. Coatings, such as carbon, have been applied to improve conductivity.[117] LTO nanostructures have been synthesized to reduce Li$^+$ diffusion lengths.[118] Doping with a host of cations has been performed to decrease its

band gap.[119] By applying these treatments, incredible reversible rates of up to 100C (full charge or discharge in almost 30 seconds) have been reported.[120-121] Song et al. showed that interestingly enough, however, pristine LTO could be cycled fairly well without any form of modification.[122] Kim et al. used an array of electrochemical and spectroscopic techniques to propose a mechanism responsible for this.[123] Their hypotheses ultimately rest on the fact that LTO's lithiated phase, $Li_7Ti_5O_{12}$, is highly conductive. If a small network of this phase can form upon initial discharge, it may enable an electronic pathway for further lithiation. Indeed, only a small amount of lithiation is required, as Young et al. have shown that at less than 5% capacity, LTO's bulk conductivity dramatically increases from about 10^{-7} to 10^{-1} $S \cdot cm^{-1}$.[124]

Understanding exactly how the phase transformation between $Li_4Ti_5O_{12}$ and $Li_7Ti_5O_{12}$ proceeds and what factors promote it, however, is still relatively ill-defined. Because the lattice parameters of both structures are near identical, few diffraction techniques are able to physically differentiate them.[125-126] Though rapid changes in bulk conductivity and light absorption have been observed upon minor lithiation, the exact mechanism that enables this is still not clear. This study aims to exploit the most significant property difference between the two species – their difference in electronic conductivity – in order to more fully explain the metal-insulator transition occurring within the system. Conductive atomic force microscopy (c-AFM) affords the possibility to directly visualize the discrete presence of each species, for the first time, at the nanoscale. We provide comprehensive current and topography maps of LTO, at various states of charge, to demonstrate where the transition between these two phases occurs, and what features promote it. We also perform x-ray photoelectron spectroscopy (XPS),

at the same states of charge, to more fully describe changes in surface morphology and composition. The unique application of the SPM methods presented here is valuable for the future optimization of this material, and others like it.

4.2 Materials and methods

4.2.1 Computation

First principles calculations were carried out to determine the band gaps of LTO and its lithiated phase. Those calculations were based on the spin-polarized generalized Gradient Approximation (GGA)[127] using the Perdew-Burke-Ernzerhof (PBE) exchange-correlation, implemented with Density Functional Theory (DFT).[128] We used a plane-wave basis set and the Projector Augmented Wave (PAW) method to replace the interaction potentials of the core electrons, as parameterized in the Vienna Ab-initio Simulation Packages (VASP).[129-130] In all calculations, Li ($2s^1$), Ti ($3p^6$ $3d^3$ $4s^1$), and O ($2s^2$ $2p^4$) were treated as the valence electron configurations. A gamma point mesh with 9 x 9 x 3 k-points was specified in the Brillouin zone and periodic boundary conditions were utilized on the model systems. All the atoms were fully relaxed to simulate the optimized structure of each lattice model, with a cutoff energy of 368 eV on a plane wave basis set. The calculated lattice constant for $Li_4Ti_5O_{12}$ was found to be 8.43 Å in this work; this value shows only a small discrepancy from the experimentally measured value of 8.35 Å (Table S1), with an error of 0.96%.

4.2.2 Synthesis

$Li_4Ti_5O_{12}$ powder was synthesized by ball milling the stoichiometric amounts of Li_2CO_3 (Mallinckrodt − 99.5+%) and TiO_2 (Aldrich − Anatase 99.9+%, which was pressed into a 2'' diameter disk and then fired in air at 950 °C for 10 hr. To ensure O_2 recovery upon cooling, the disk was cooled slowly at 0.5 °C·min^{-1} to 700 °C, which was held at 700 °C for 20 hr, and finally cooled down at 10 °C·min^{-1} to room temperature. The dense pellet was subsequently bound to a Cu plate and used as a target for magnetron sputtering. LTO films were grown by means of r.f. magnetron sputtering in an Ar atmosphere (Air Liquide − Research Grade), at an applied RF power of 80 W, at a pressure of 5 mtorr, where deposition was performed once the base pressure in the chamber reached 10^{-6} torr. The films were grown on 1 cm Al_2O_3 disks (Valley Design) coated with 0.25 µm of Pt (Refining Systems, Las Vegas Nevada, USA − 99.99%) on both sides, which acted as the negative electrode current collector. Sputtering of the Pt was performed in direct current mode using 25 W and 15 mtorr Ar pressure. The as-deposited LTO films, with a typical thickness of 800 nm, were annealed in air at 700 °C for 1hr to develop the spinel structure

4.2.3 Electrochemical cells

LTO thin-films were assembled into standard Swagelok cells, in an Ar-filled glove box. Li foil (0.75 mm Alfa Aesar − 99.99%) was used as anode, two-sheets of Celgard 2500 served as separator, and the electrolyte was composed of 1.2 M $LiPF_6$ in ethylene carbonate/ethyl methyl carbonate. A Maccor Battery Tester was used to galvanostatically cycle cells at a current of 4 µA·cm^{-2}, between 1.0 and 2.0 V. Cells used

for further analysis were stopped at various points during the first cycle and described by the following: 1) LTO prior to cycling (pristine); 2) LTO discharged to 50% of the initial discharge capacity (50% dis); 3) LTO discharged to 1.5 V into the initial discharge (1.5V dis); 4) LTO discharged to 1.0 V into the initial discharge (1.0V dis); 5) LTO charged to 50% of the initial charge capacity, following discharge to 1.0V (50% chg); 6) LTO charged to 2.0 V into the initial charge, following discharge to 1.0V (chg 2.0V). The pristine sample used before cycling was assembled into a Swagelok cell and allowed to equilibrate for 24 hrs before disassembly. All other cells were disassembled immediately following their electrochemical exit condition. Following disassembly in a glove box, LTO thin-films were briefly washed in dimethyl carbonate (Aldirch – 99% Anhydrous) to remove residual electrolyte. They were left to dry within the glove box before transporting within a sealed, Ar-filled container.

4.2.4 GIXRD and SEM

The focused ion beam (FIB) cross section of LTO was fabricated with an FEI Scios, using a 1.0 nA beam current, at 30 kV. The scanning electron microscopy (SEM) image was collected using a 0.1 nA current, at 5 kV. The grazing incidence x-ray diffraction (GIXRD) pattern was collected using a Rigaku SmartLab x-ray diffractometer, utilizing the Parallel Beam/Parallel Slit Analyzer mode. The incident angel was 0.5° and the incident slit was 0.5 mm. The data was collected from 15-80° 2θ, with a 0.05° step at $1°\cdot min^{-1}$.

4.2.5 AFM

Atomic force microscopy was performed using an Asylum Research Cypher S, housed within an Ar-filled glove box. Pt-coated tips (Nanosensors) with a radius of curvature of 20-50 nm at the apex were used for conductivity (c-AFM) measurements. LTO thin-films were transported in sealed Ar-filled transfer chambers between glove boxes and were never exposed to air. Inside the glove box the thin-films were mounted onto two-sided Cu-clad circuit board using silver paste. The paste was applied to both the bottom of the thin-film, as well as a portion of the side and top, which ensured electrical contact throughout the entire film. These mounted thin-films are shown in Figure 4.4. This figure also demonstrates the port connecting the circuit board and thin-film to the AFM tip. A fixed voltage of 0.4 V was applied between the tip and sample during scans. The current was measured using a 10^6 V·A^{-1} amplifier gain. Before plotting, height images were flattened using WSxM software (5.0 Develop 4.3).[131]

4.2.6 XPS

A PHI 3056 spectrometer possessing a hemispherical detector 54.7° off normal and a dual Mg and Al anode source, operating at 15 kV and 350 W, was used for all x-ray photoelectron spectroscopy (XPS) analyses. LTO thin-films were transferred from an Ar-filled glove box to custom airtight chambers for direct transfer to the spectrometer, without exposure to air. The XPS chamber was maintained at $<10^{-8}$ Torr during measurement. High-resolution scans made use of the Al source, using a pass energy of 23.5 eV and a step size of either 0.05 or 0.075 eV. Each scan was preceded by a high-resolution C 1s scan, to account for charge build up. XPS processing was perfomed using

CasaXPS software. The main C 1s peak was calibrated to carbon black, 284.6 eV, as was

the following high-resolution scan. Peaks were deconvoluted using Gaussian-Lorentzian

line shapes and Shirley background subtractions.
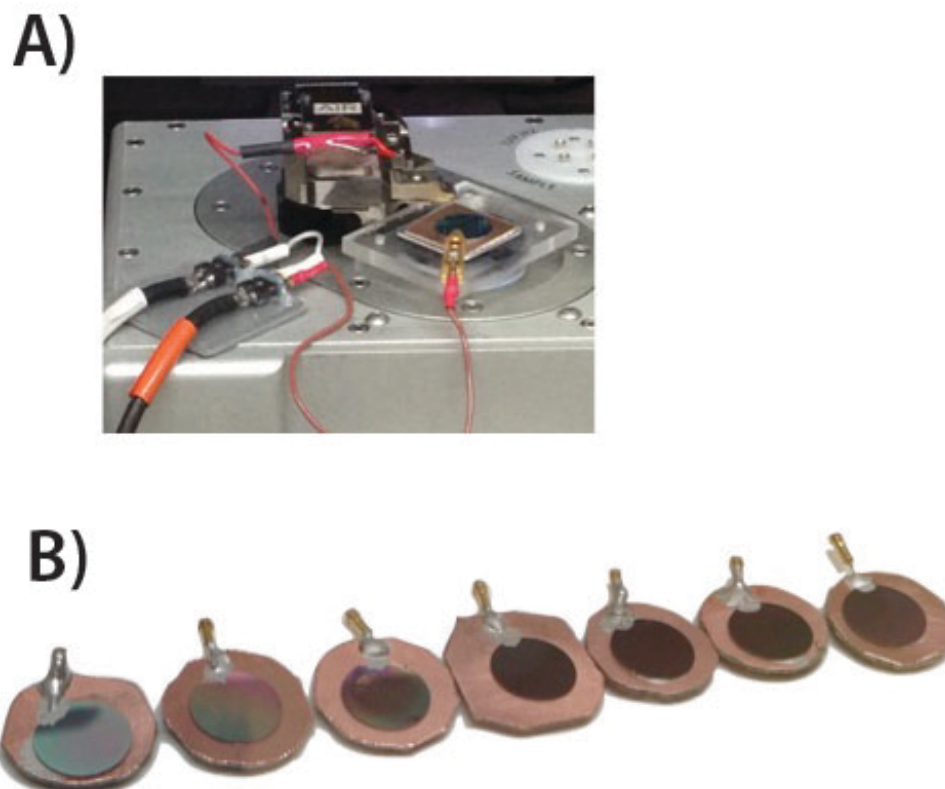
Figure 4.1 LTO thin-films used for SPM analyses. (A) Electrical connections made for c-AFM measurement. (B) LTO thin-films mounted onto Cu-clad circuit board; from left to right depicts the following: pristine without exposure to electrolyte, pristine assembled into a Swagelok cell and soaked 24 hrs, discharged 50%, discharged to 1.5 V, discharged to 1.0 V, charged to 50%, charged to 2.0 V.

4.3 Results and discussion

4.3.1 LTO structure

As described previously, the crystal structures of $Li_4Ti_5O_{12}$ and its lithiated form, $Li_7Ti_5O_{12}$, are highly similar – both being defined by space group $Fd\bar{3}m$. Figure 4.2a depicts the optimized lattice models of each. $Li_4Ti_5O_{12}$ consists of tetrahedral 8a and octahedral 16d sites, coordinated by oxygen in 32e sites. Ti exists solely in 16d sites. While Li occupies all 8a sites, it also shares ⅕ of the 16d sites with Ti. To highlight this and its spinel structure, the chemical formula is often alternatively represented as $Li[Li_{1/3}Ti_{5/3}]O_4$. Upon lithiation, the 16d sites are unchanged. The remaining Li in $Li_7Ti_5O_{12}$, however, adopt an octahedral geometry in newly formed 16c sites.

The valence of Ti in $Li_4Ti_5O_{12}$ exists solely in the 4+ state. This results in an empty t_{2g} band (no d-orbital electrons), which forms the material's LUMO. The HOMO derives from the filled 2p orbitals of oxygen. The DFT band structure calculation shown in Figure 4.2b reveals that the band gap between these two is 2.3 eV. Though lower than experimentally reported values, it is consistent with the computational results found in literature, which supports that the material is an insulator.[132-133] Upon lithiation, 3 Ti^{4+} per formula unit are reduced to Ti^{3+}, as represented in the following two-phase reaction equation:

$$Li_4Ti_5^{4+}O_{12} + 3Li^+ + 3e^- \xrightleftharpoons[charge]{discharge} Li_7[Ti_2^{4+}Ti_3^{3+}]O_{12}$$
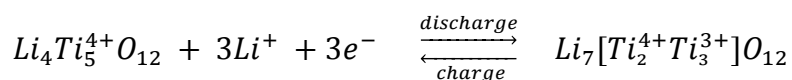
The equation implies that two more Li^+ can be theoretically inserted, fully reducing Ti^{4+} to Ti^{3+}, while maintaining charge balance. This is discussed further, in following sections.

The additional electrons acquired upon discharge inserts 1e$^-$ per previously unoccupied t_{2g}, which essentially removes the band gap. Figure 4.2b demonstrates that the electronic DOS of $Li_7Ti_5O_{12}$ is continuous across the Fermi level. Because the reaction has no intermediates and proceeds directly between an insulating ($Li_4Ti_5O_{12}$) and conducting phase ($Li_7Ti_5O_{12}$), we can clearly observe where that reaction occurs across the electrode, using c-AFM. This concept is illustrated in Figure 4.2c.
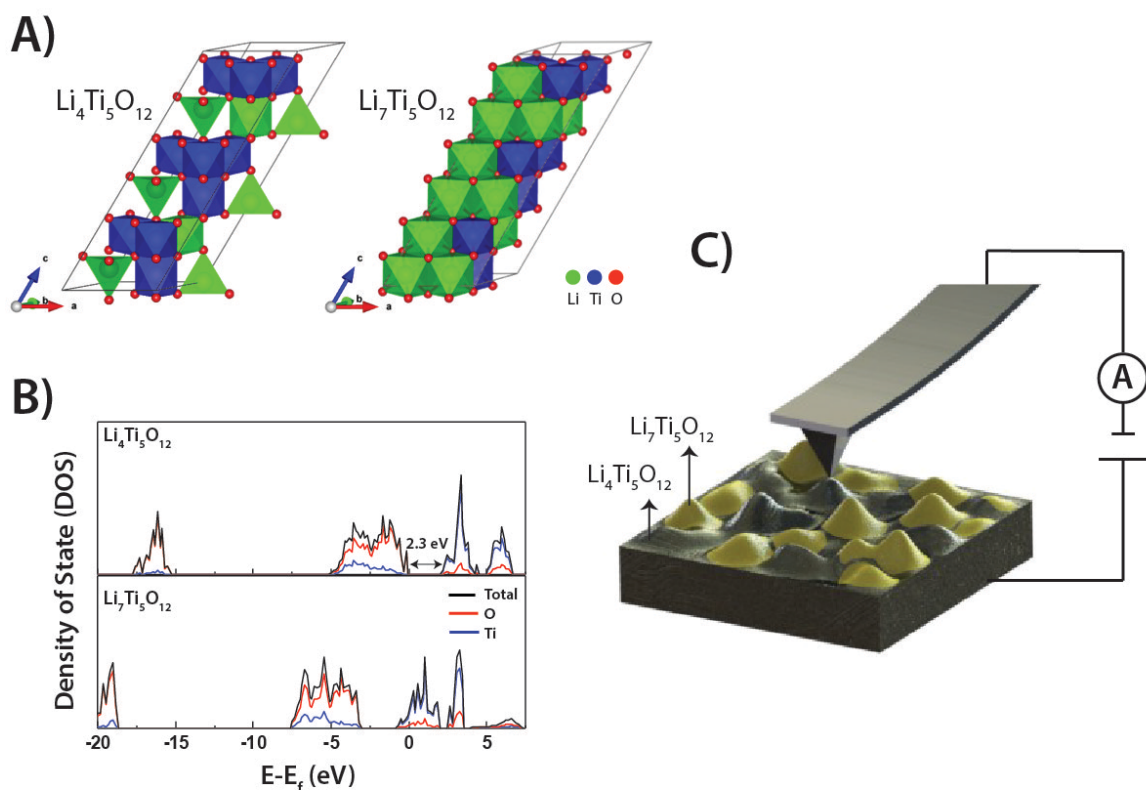
Figure 4.2 Structure and electronic properties of LTO. (A) Structurally optimized $Li_4Ti_5O_{12}$ and $Li_7Ti_5O_{12}$ lattices. (B) Density of states (DOS) of $Li_4Ti_5O_{12}$ and $Li_7Ti_5O_{12}$, where the Fermi energy is normalized to 0 eV. (C) Illustration of c-AFM capability to detect the presence of each phase due to their unique conductivities.

4.3.2 Thin-film characteristics

The common use of conductive additives in LTO composite electrodes heavily influences the manner in which its electrochemical reaction occurs. This is evidenced by the great deal of research dedicated to creating LTO-carbon composites.[134-136] In order to determine how LTO's fundamental mechanism proceeds, therefore, we made use of thin-films that possessed only the pristine material. The thin-films prepared by RF magnetron sputtering are shown in Figure 4.3c. A thickness of about 800 nm was measured. LTO was grown on Al_2O_3 disks, which were coated on all sides by a thin layer, roughly 225 nm, of Pt. This layer ensured good electrical contact for use in batteries as well as for c-AFM analysis. Figure 2d illustrates the particle size distribution of deposited LTO, which was $20 - 100$ nm on average. The film was highly crystalline, as demonstrated by the GIXRD in Figure 4.2a. Some LTO peaks are quite large, such as the (400) and (511) indices, due to overlapping contributions from Al_2O_3 substrate. A three-phase fit, incorporating all layers, was performed in order to confirm their structures and lattice parameters. LTO, Pt, and Al_2O_3 were fit to space groups $Fd\bar{3}m$, $Fm\bar{3}m$, and $R\bar{3}c$, respectively. The low residual, resulting in a conventional Rietveld factor (R_{wp}) of 7.18, confirms the purity of the film. The LTO lattice parameter was determined to be 8.352, which is in good agreement with the values reported in literature.[137] A full list of refinement results is provided in Table 4.1.

Figure 4.2b highlights the material's first electrochemical cycle and demonstrate good reversibility over the first 10 cycles. The voltage response is the result of applying a constant current of -4 $\mu A \cdot cm^{-2}$ to 1.0 V upon discharge and 4 $\mu A \cdot cm^{-2}$ to 2.0 V upon charge. Given that the average capacity upon cycling was around 30 $\mu Ah \cdot cm^{-2}$, the

current corresponds to a rate of roughly C/7.5. The flat redox potential at 1.55 V vs Li/Li$^+$ is indicative of the two-phase reaction between $Li_4Ti_5O_{12}$ and $Li_7Ti_5O_{12}$. Though no significant redox feature exists outside the plateau, a nontrivial amount of capacity is shown to exist outside the voltage window of 1.4 and 1.6 V, corresponding to 9.7 μAh or roughly 20% of the initial discharge. This behavior is typical when cycling LTO thin-films and is likely due the relatively high fraction of LTO in contact with electrolyte.[138] This concept is expanded upon in following sections of this paper. The relatively large capacity outside of the plateau is not reversible, as highlighted in Figure 4.3. The capacity retention of the first cycle is only 58.9%, but immediately improves upon subsequent cycles, gradually increasing to 93.5% by the 10th cycle. The amount of capacity outside of the 1.4 − 1.6 V window also drastically decreases after the first cycle, to 4.3 μAh during the 2nd discharge. In order to explore the unique changes occurring in this system during the first cycle, we analyze the thin-films at the points indicated along the voltage profile in Figure 4.2b. The samples characterized specifically correspond to the following: 1) pristine LTO, assembled into a battery, but not cycled; 2) LTO discharged to 50% of the initial discharge capacity; 3) LTO immediately following the voltage plateau, discharged to 1.5 V; 4) LTO fully discharged to 1.0 V; 5) LTO charged to 50% of the 1st charge capacity; 6) LTO fully charged to 2.0 V. The exact thin-films used are represented in Figure 4.4.
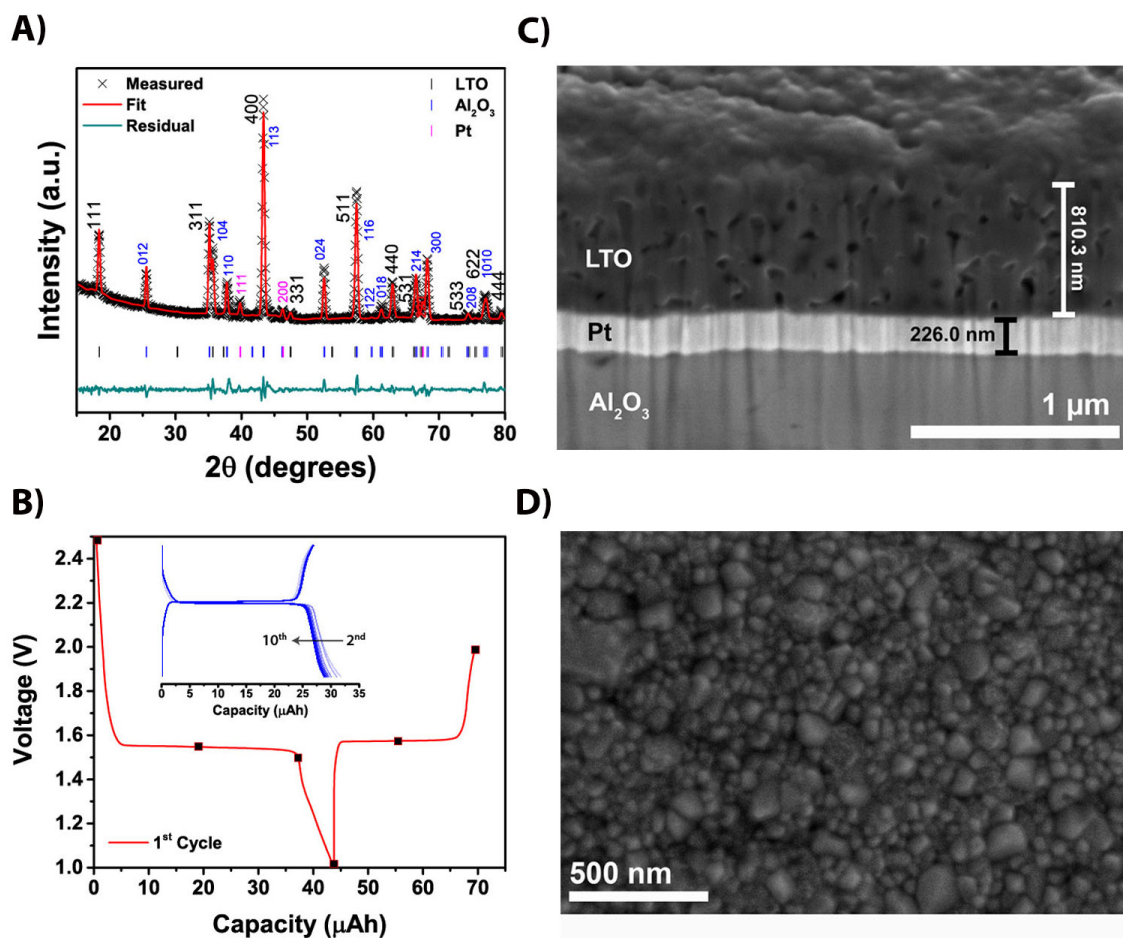
Figure 4.3 LTO thin-film physical and electrochemical characteristics. (A) XRD and Rietveld refinement of LTO thin film. (B) Electrochemical profile of 1st cycle, squares indicating points where samples were characterized, and first 10 cycles – inset. (C) SEM cross-section of LTO thin-films and (D) top SEM image of the same thin-film.
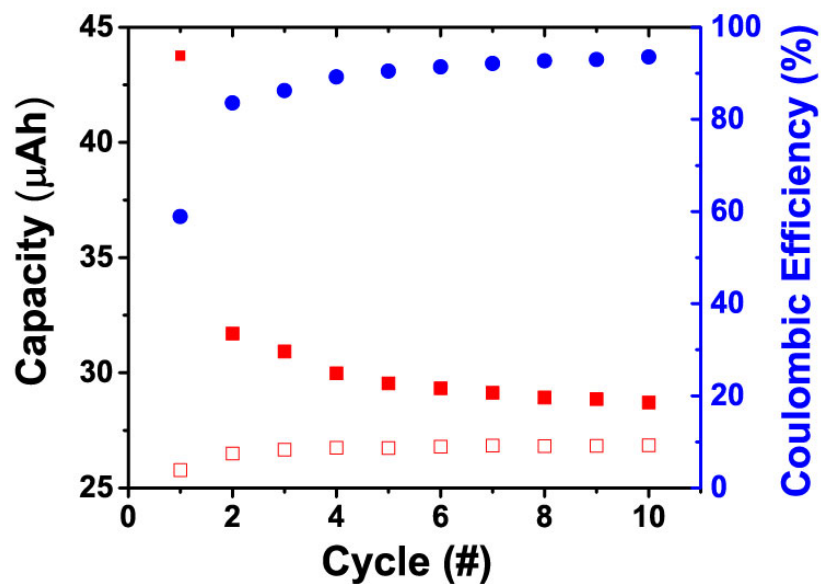
Figure 4.4 Electrochemical retention of LTO thin-film. Charge (solid red squares) and discharge (open red squares) capacities of the first 10 cycles of LTO thin-films; the right axis (blue circles) corresponds to the resulting current efficiency.

Table 4.1 Rietveld refinement parameters of the pristine LTO thin-film.

Phase	a,b (Å)	c (Å)	c (Å)	Fraction (%)	R_{wp}	R_B
LTO	8.352(1)	8.352(1)	8.350(2)	36.51	7.18	3.754
Pt	3.922(3)	3.922(3)	8.353(3)	0.12	7.18	5.264
Al_2O_3	4.761(6)	13.007(0)	8.354(0)	63.38	7.18	5.851

4.3.3 Atomic force microscopy

AFM topography images of the pristine sample soaked in electrolyte correlate well to the SEM images of LTO that were not. This indicates that mere exposure to electrolyte has little or no effect on the material's morphology and suggests no major reactions occur at open-circuit. 2D height images and line profiles of each sample are presented in Figure 4.5. The average maximum height of features across multiple images of the pristine sample was 72.8 nm and it possessed a root-mean-square (RMS) surface roughness of 11.1 nm. Upon discharging to 50% capacity, these values did not change appreciably, with an average maximum of 76.5 nm and surface roughness of 11.2 nm. A summary of surface dimensions for all samples is provided in Table 4.2. While the morphology did not change upon initial discharge, the measured current did. Figure 4.6 depicts the current response of all samples when a potential of 0.4 V was applied. While no current is observed in the pristine material, current is measured within an array of individual grains after discharging to 50%. After discharging just past the entire plateau, to 1.5 V, the magnitude and distribution of current increased by two-fold. The total current measured in each sample is more quantitatively represented by histograms, fit to normal distributions, shown in Figure 4.7. Figure 4.6c demonstrates that immediately following the two-phase reaction, nearly all grains in the LTO film are conductive. This suggests that the formation of the conductive phase, $Li_7Ti_5O_{12}$, has reached completion.

Interestingly, when discharging beyond 1.5 V to the typical LTO cutoff voltage of 1.0 V, the surface morphology is shown to dramatically change. The size of the average particles increase, and the overall conductivity decreases. Figure 4.6d demonstrates that all grains exhibit lower conductivity overall, but very large grains show none. The

average current measured in samples discharged to 1.5 and 1.0 V is 0.58 and 0.32 μA, respectively. The average RMS surface roughness of samples discharged to 1.0 V increased significantly to 16.4 nm. This change in surface morphology is not completely irreversible, however, as subsequently charging to 50% capacity shows reduced grain sizes, with an intermediate RMS surface roughness of 13.5 nm. Furthermore, the RMS surface roughness of LTO charged completely to 2.0 V nearly reaches its original value, at 12.1 nm. The conductivity map of LTO charged 50% is also fairly similar to when it was discharged 50%. The average current measured in the former is 0.12 μA and the latter, 0.14 μA. As suggested by the poor first cycle capacity retention, however, some partial irreversibility is clearly present. While the average current of samples discharged and charged to 50% were fairly similar, their RMS surface roughnesses were not.

The difference in surface morphology, and the structural evidence of irreversibility, is more clearly depicted in the deflection images shown in Figure 4.8. After discharging to 1.0 V, and subsequently charging to 50% capacity, the morphology of grains are less defined. The deflection image in Figure 4.8e reveals a number of more flattened or fused grains, almost as if a film covers them. The corresponding current image in Figure 4.8e shows only partial current in those regions. The deflection image in 4.8f shows that after full charge to 2.0 V, the surface morphology of LTO contains a large proportion of well-defined flattened regions. While the current in this sample is extremely low, some exists. Figure 4.7 shows that this current is above the threshold of noise, compared to the pristine signal in Figure 4.7a. In addition, the current map in Figure 4.8f shows that the large flattened morphologies are where the small current remains. The fact that some current exists in the fully charged state suggests that a semi-

permanent conductive percolation network may form upon the initial charge, thus reducing the activation potential for subsequent cycles. Indeed the electrochemical efficiency is shown to improve upon cycling; an embedded conductive matrix that increases over time may be partially responsible for this.

Kim et al. hypothesized that within LTO possessing no conductive additive, $Li_7Ti_5O_{12}$ phase first forms in the vicinity of immediate contact with the current collector.[123] Upon further discharge, this phase was thought to evenly propagate upward, through all particles, towards the interface with electrolyte. Our data (Figure 4.8) shows, however, that this is not the case. In the sample discharged 50% (Figure 4.8b) we strictly measure current within discrete grains, not evenly across the surface. This suggests that the transition of $Li_4Ti_5O_{12}$ to $Li_7Ti_5O_{12}$ proceeds via a limited number of narrow percolation channels that connect current collector and electrolyte. Figure 4.9 visually depicts the difference. In fact, there are a number of regions with near-identical grains adjacent to one another, which exhibit current in one and not the other. Furthermore, the particles themselves are very well defined in the current images of Figure 4.8. This is due to the fact that lower current is measured within grain boundaries, suggesting the phase transition does not propagate laterally across grains. This may be due to lower LTO crystallinity connecting these grain interfaces.
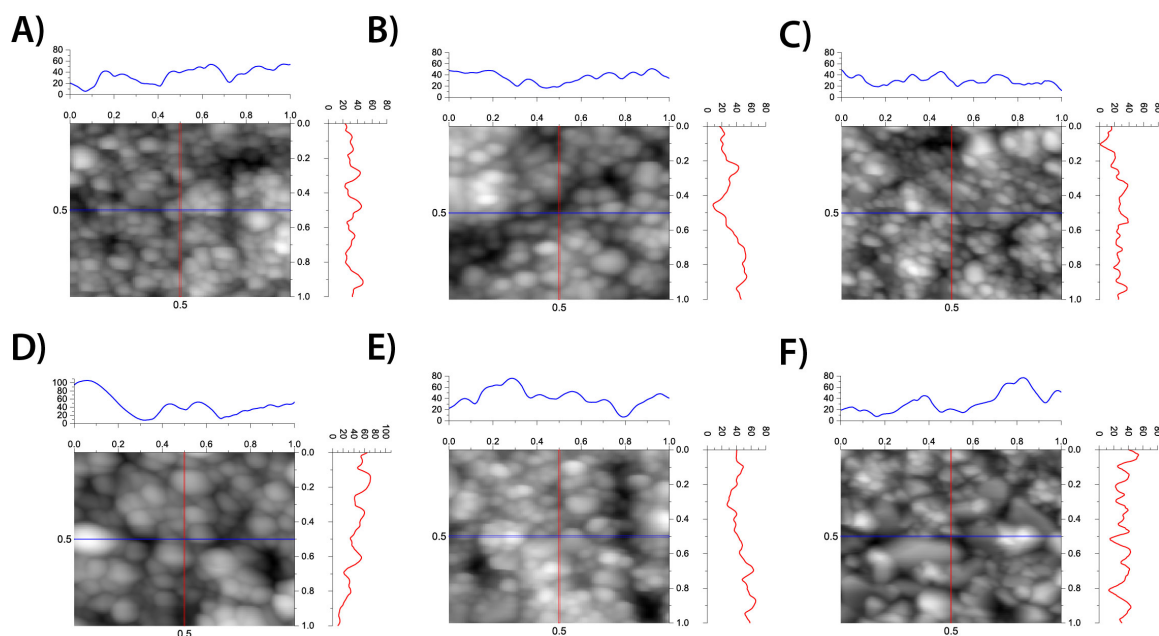
Figure 4.5 Height images and cross-section profiles of LTO thin-films. (A) pristine LTO, (B) discharged 50%, (C) discharged to 1.5V, (D) discharged to 1.0V, (E) charged 50%, and (F) charged to 2.0V.
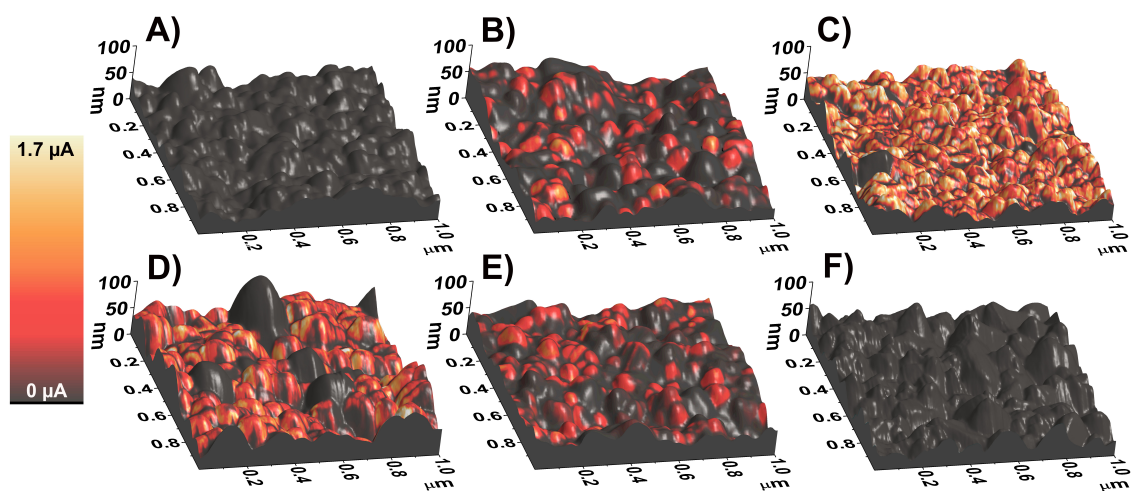
Figure 4.6 3D topographical AFM images of LTO thin-films cycled to various states of charge. They correspond to (A) pristine LTO, (B) LTO discharged to 50% capacity, (C) LTO discharged to 1.5V, (D) LTO discharged to 1.0V, (E) LTO charged to 50% capacity, and (F) LTO charged to 2.0V. The color scheme represents the current detected.
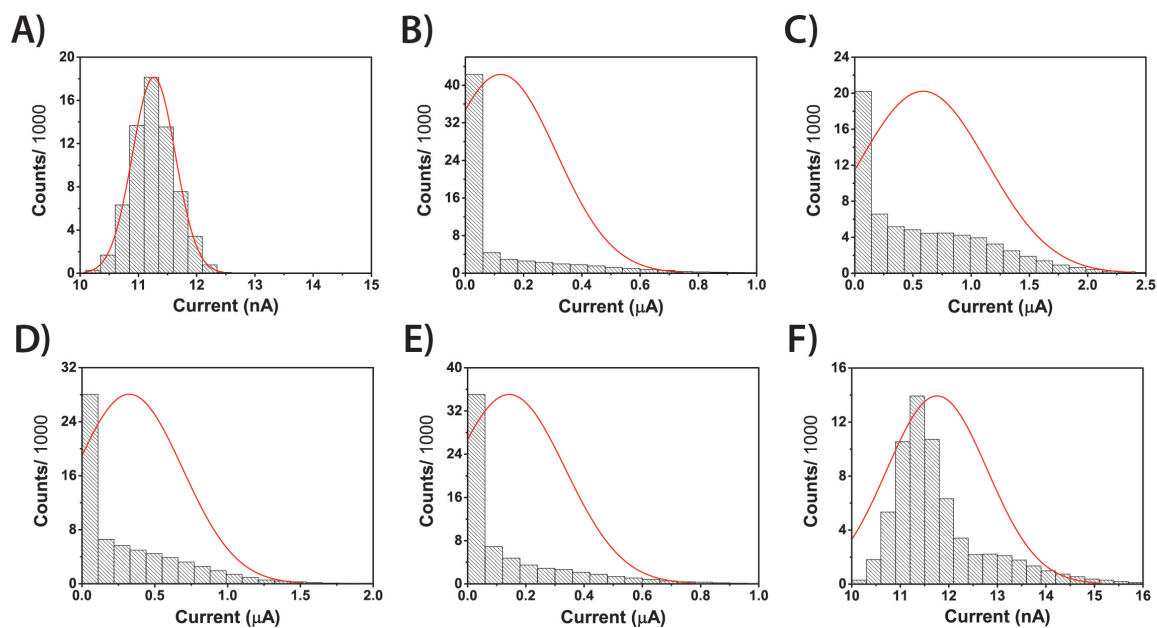
Figure 4.7 The total current, fit to a normal distribution (red line), of LTO thin-films. They correspond to (A) pristine LTO, (B) discharged 50%, (C) discharged to 1.5V, (D) discharged to 1.0V, (E) charged 50%, and (F) charged to 2.0V.
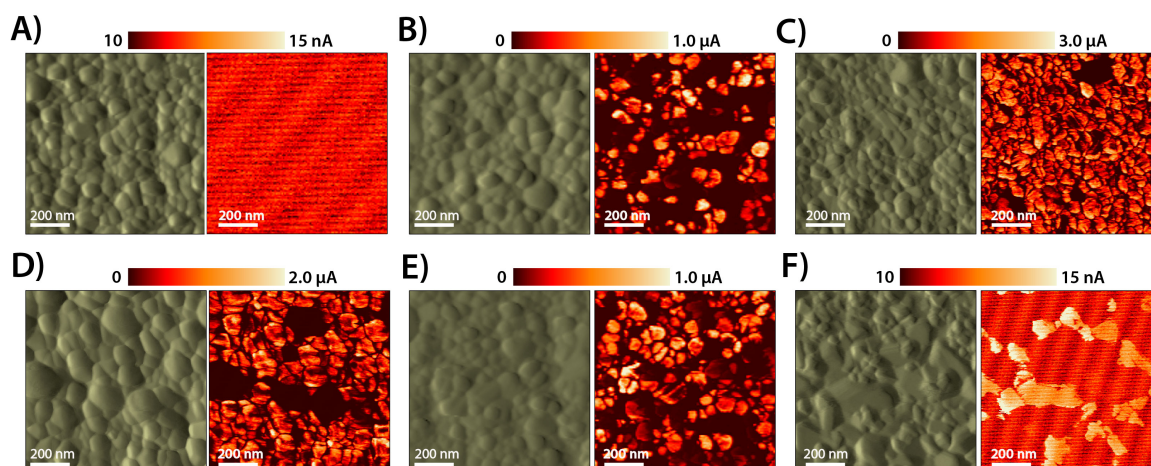
Figure 4.8 AFM deflection (left) and current (right) images of LTO thin-films. They correspond to (A) pristine LTO, (B) discharged 50%, (C) discharged to 1.5V, (D) discharged to 1.0V, (E) charged 50%, and (F) charged to 2.0V.

Figure 4.9 Illustration differentiating how the transition between $Li_4Ti_5O_{12}$ (black) and $Li_7Ti_5O_{12}$ (yellow) may propagate through an electrode. Our results confirm only the transition via a percolation network (right).

Table 4.2 Average LTO thin-film parameters at the states of charge indicated. Parameters include average root-mean-square surface roughness (<RMS>), average maximum height (<Max Height>), and average current resulting from the applied bias of 0.4V (<Current>).

LTO	<RMS> (nm)	<Max Height> (nm)	<Current> (μA)
Pristine	11.1	72.8	1.1e-2
Dis 50%	11.2	76.5	0.12
Dis 1.5V	10.8	66.1	0.58
Dis 1.0V	16.4	106.2	0.32
Chg 50%	13.4	78.7	0.14
Chg 2.0V	12.1	77.0	1.2e-2

4.3.4 Surface characterization

To provide a more robust explanation for the apparent grain size expansion upon discharge to 1.0 V, and flattening upon subsequent charge, we performed XPS analysis on thin-films cycled to the same points. Figure 4.10 shows high-resolution scans of the C1s, O1s, and Ti2p regions. The single peak centered at 458.0 eV corresponds well to the $2p_{3/2}$ peak of Ti^{4+} in LTO, as well as in TiO_2.[139-140] Upon discharge, a second peak at 455.9 eV forms, which corresponds to the Ti^{3+} found in Ti_2O_3.[141] This peak reaches a maximum relative to the Ti^{4+} peak, in the LTO sample discharged to 1.0 V. The lower binding energy peak correlates to the formation of Ti^{3+} due to reduction of Ti^{4+} upon lithiation. LTO is fully discharged at 1.0 V, which is why the peak at 455.9 eV is largest in that sample. The relative intensity of the Ti^{3+} peak decreases upon charge and completely disappears at 2.0 V, indicating that the reaction is fully reversible. The peak in the O1s spectra at 529.7 eV corresponds to O^{2-} in the LTO lattice.[142] Upon discharge, a peak at 531.5 eV grows relative to it, and reaches maximum at 1.0 V. This higher binding energy peak results from the contributions of several species, including CO_3^{2-}, $-CO_2-$ and $Li_xPO_xF_z$, all of which originate from the decomposition of electrolyte. The formation of decomposition products, Li_2CO_3 and/or $LiCO_3R$, are also shown to significantly occur in the sample discharged to 1.0 V, as suggested by the shift in the C1s satellite peak near 289.5 eV.[143]

The fact that we observe these species is significant because LTO is excessively championed to form no passivation or solid electrolyte interface (SEI) layers, due to its high redox potential. This is clearly not the case, however. LTO is known to have major gassing issues, which result from its interaction with alkyl carbonated-based solvents.[144]

He et al have also reported that LTO with very high surface areas can exhibit SEI.[145] The nature of working with thin-films is such that a disproportionately large percent of the active mass is in direct contact with electrolyte. Any reaction with electrolyte will be amplified, therefore, as the thin-film/electrolyte interface is quite large. The formation of these electrolyte decomposition products may be responsible for the material's extended 1st cycle discharge capacity. A passivation layer may form upon initial discharge to create a relatively stable SEI; since subsequent cycles show markedly improved capacity retention, the reduction of electrolyte does not appear to occur continuously.

The poor first cycle retention suggests that the decrease in the higher binding energy O1s side peak upon charge, does not proceed via the oxidation of these species. Instead, they may be chemically consumed in further side reactions. Figure 4.11 shows that the peaks in the P2p and F1s spectra – corresponding to $Li_xPO_yF_z$ at 133.7 eV and LiF at 685.1 eV – both increase significantly upon charge. Figure 4.11 also depicts the elemental compositions derived from the XPS survey scans. This plot shows that the degree of F and P increase significantly upon charge, from 6.3 to 10.7% (F) and 0.8 to 1.9% (P) in samples charged to 50% and 2.0V, respectively. The full percent abundance of all species derived from component fitting of the high-resolution scans, is provided in Table 4.3. These results complement the morphological changes observed using AFM.

When discharged to 1.0 V, an SEI is shown to form, which likely contributes to the increased grain sizes observed. Kitta et al also observed changes in LTO morphology upon cycling, which they attributed to surface restructuring into Li_2TiO_3 due to reaction with electrolyte.[146] It is possible that reduction of electrolyte with the relatively high surface area LTO leads to volume expansion, due to the formation of an overlithated

phase such as this. Table 4.3 shows that a higher concentration of Li exists at the surface of LTO discharged to 1.0 V compared to 1.5 V, suggesting the phase may form at low voltage. Where the extent of this reaction occurs most, leads to either delamination of the grain from current collector or the formation of a nonconductive species, as larger particles clearly show no conductivity. Though the particles decrease in size upon charge, they also merge to an extent or become flatter. This may be due to the continued formation of decomposition products, from carbonate-based species, to fluorinated ones. The increasing appearance of merged LTO grains upon charge may result from the fact that the surface has been coated with a significant amount of LiF – from 2.7% when discharged to 1.5 V, to 10.7% at full 2.0 V charge. Our observation of these changes in surface composition should contribute to the bigger picture of how gassing may occur in this system.

Table 4.3 Atomic surface concentrations for C, O, F and P in the various surface groups. For the pristine material, the O=C- signal overlaps with the response expected for –OH surface groups.

Sample	C-R (284.8 eV)	C-O (286 eV)	$LiCO_2R$ (288 eV)	CO_3^{2-} (289.5 eV)	O^{2-}	$-CO_2$-, CO_3^{2-} $Li_xPO_yF_z$	O-C	LiF	$Li_xPO_yF_z$	P	Li
Pristine	18.4	3.5	2.1	N/A	41.7	4.4	2.6	N/A	N/A	N/A	12.9
Dis 50%	27.4	3.6	1.1	3.5	17.9	17.8	2.5	2.4	1.4	0.6	15.7
Dis 1.5V	22.7	2.5	0.6	4.1	19.5	19.7	3.5	3.5	0.4	0.8	15.9
Dis 1.0V	28.0	1.7	0.7	4.5	15.3	19.8	3.0	2.7	0.5	0.8	17.9
Chg 50%	19.3	3.3	1.1	3.6	16.7	19.3	3.5	6.3	1.0	0.8	19.0
Chg 2.0V	21.8	2.2	1.6	1.6	19.9	13.1	3.6	10.7	1.5	1.9	14.5
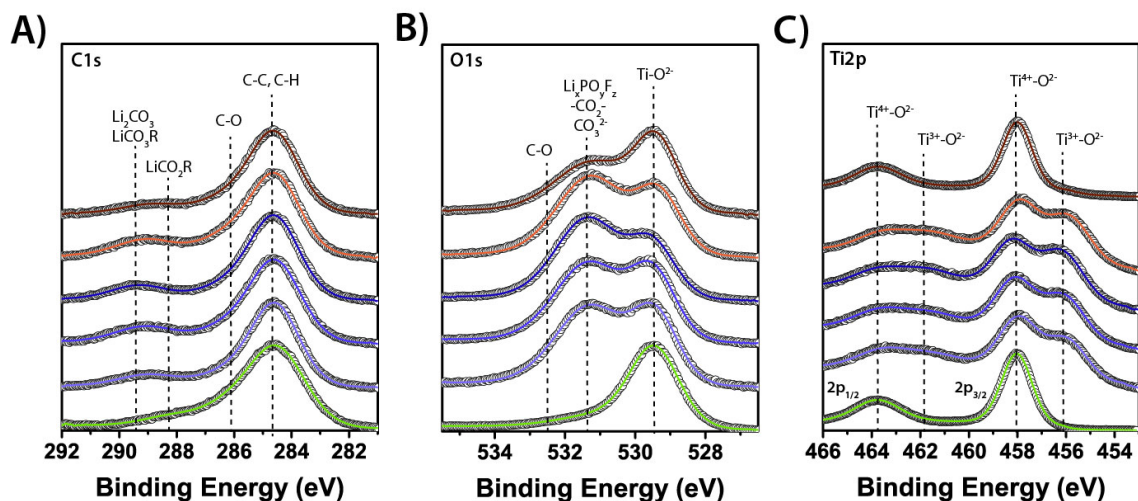
Figure 4.10 Normalized high-resolution C1s (A), O1s (B), and Ti2p (C) XPS spectra of the LTO thin-films discharged and then charged. From bottom to top they correspond to pristine (green), discharged 50% (light blue), discharged to 1.5V (blue), discharged to 1.0V (dark blue), charged 50% (red), and charged to 2.0V (dark red).
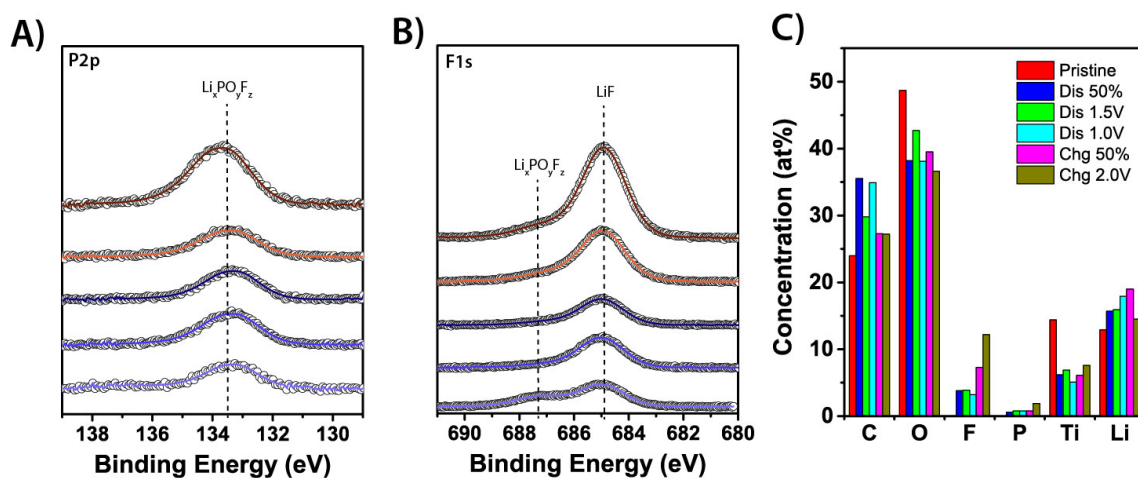
Figure 4.11 Non-normalized high-resolution (A) P2p and (B) F1s XPS spectra of LTO thin-films discharged and then charged. From bottom to top, they correspond to samples discharged 50% (light blue), discharged to 1.5V (blue), discharged to 1.0V (dark blue), charged 50% (red), and charged to 2.0V (dark red). (C) Elemental surface compositions of LTO obtained from XPS survey scans.

4.4 Conclusions

This work applies c-AFM, in a novel manner to directly visualize at the nanoscale, for the first time, the phase transformation between $Li_4Ti_5O_{12}$ and $Li_7Ti_5O_{12}$. The structure and band-gap of each material was confirmed using DFT calculations. $Li_4Ti_5O_{12}$ is an insulator, while $Li_7Ti_5O_{12}$ is a conductor. By cycling LTO to various states of charge and measuring the local current in response to a fixed bias, we were able to determine exactly where each phase existed at those states of charge. For ease of analysis with AFM and to avoid contribution of conductive additives, which are common and have a significant influence on the mechanism, we used thin-film LTO in our analysis. These 800 nm thick films were determined to be phase pure by grazing incidence XRD Rietveld analysis; the electrochemistry also suggested as much. As opposed to prevailing theories, we determined that the transition of $Li_4Ti_5O_{12}$ to $Li_7Ti_5O_{12}$ proceeds via percolation channels within single grains. The reaction does not appear to propagate laterally, across grain boundaries. It also does not form evenly throughout the electrode. Upon discharge beyond the 1.55 V redox plateau, to 1.0 V, significant changes in surface morphology and conductivity occurred. We demonstrated that this was related to the interaction of LTO and electrolyte from 1.5 to 1.0 V. Continued reaction with electrolyte was determined to occur upon charge, which may provide insight into the mechanisms of the well known, but poorly understood, and highly deleterious, gassing mechanism of LTO. The use of c-AFM described here may be used towards the future optimization of morphologies that preferentially enable desired metal-insulator transition, such as the case with LTO, as the process can be clearly identified using this method.

Chapter 4, in full, is a reprint of the article, "Elucidating the Phase Transformation of $Li_4Ti_5O_{12}$ Anode at the Nanoscale Using c-AFM," which is in preparation for submission. The dissertation author was the primary investigator and author of this paper.

Chapter 5

Summary

5.1 Concluding Remarks

A wide variety of battery technologies continue to permeate the market. The reason for this is that no one battery possesses the complete set of characteristics needed to suit every energy storage application. Among the desired characteristics, such as low cost, long cycle life, high power and energy density, and reasonable safety, we are typically forced to choose two. The soluble lead flow battery is extremely inexpensive and can exhibit long cycle life. Its depth of discharge, and therefore energy density, however, is low. Its power density is also low compared to other flow batteries, such as vanadium redox. The Li-ion battery, on the other hand, can exhibit quite high energy and power densities. Their cost is high, however, and safety is an issue, as popular media continues to document cases of their combustion due to shorting or thermal runaway. $Li_4Ti_5O_{12}$ presents a much more safe and stable alternative to conventional anodes such as graphite, but it comes at the cost of much coveted energy density. Li-excess cathode materials offer the opposite benefits – high energy density, but poor rate capability and retention. Because no one battery can answer all our needs, we instead aim to match them with applications that do not as heavily require their corresponding deficiency. Energy density is not critical for grid storage applications, for example, hence providing a good market for flow batteries.

This thesis provides an in-depth analysis of the diverse phenomena resulting in several of these systems. It also provides a cautionary tale to not approach battery research with overgeneralized assumptions regarding their electrochemistry. For example, nanostructured electrodes are often thought to possess advantageous electrochemical properties. Nanoengineered particle morphologies may indeed promote faster reaction kinetics due to decreased diffusion distances and higher surface energies. In the case of the soluble lead flow battery, for example, the formation of nanoscale PbO_2 morphologies greatly enhances its dissolution upon discharge – improving its reversibility and long-term cycle life. In the case of Li-excess cathode material, however, nanoscale morphologies also promote deleterious side reactions with electrolyte that degrade cycle life. The formation and stability of SEI layers within Li-ion batteries are still relatively poorly understood. The work presented here shows that even LTO – an anode believed to form no SEI – undergoes significant reaction with electrolyte upon cycling when a very high surface area to bulk ratio exists. Though nanostructured LTO may promote the phase transformation of $Li_4Ti_5O_{12}$ to $Li_7Ti_5O_{12}$ due to relatively large high-energy phase boundaries within very small particles, specific nanoscale morphologies may need to be tailored to mitigate its reaction with electrolyte. Only by providing more comprehensive analyses of nanoscale phenomena, as they pertain to each unique system of study, can we hope to take advantage of their properties.

5.2 Future Perspectives

The work described in this dissertation presents several unanswered questions, which provide direction for further research. Each of the three electrode materials, described in Chapters 2-4, possess some shortcoming that prevents their successful wide-scale commercialization. In the case of the soluble lead flow battery, we engineered an approach to improve cycle life and efficiency by increasing flow rates and the battery's charge potential. The voltage efficiency suffers by doing so, however, as does the system efficiency. The energy required to operate pumps for flow, for example, were not taken into consideration when reporting round-trip energy efficiency. The faster electrolyte is flowed, however, the more electricity the pumps require – resulting in lower energy efficiencies. The low voltage charge potential was the root of the problem. Instead of increasing the overpotential by using either constant voltage charge techniques or high current densities, there may be a way to chemically mitigate the reactions that results in low voltage charging. Additives, for example, may affect the kinetics of PbO_2 deposition and dissolution. In order to select the proper additive to use, we first need to further understand how the Pb^{2+}/PbO_2 reaction proceeds. Positive electrode (lead oxide) deposits at various states of charge may be characterized using XAFS and XPS in order to determine whether intermediate oxides species form. Initial evidence suggests this is the case. By elucidating what deleterious side-reactions occur at the positive electrode, we may be able to propose methods of eliminating them.

In Chapter 3, the effect of particle morphology and surface area on Li-excess capacity retention and surface chemistry was described. It was shown that very small particle sizes and high surface areas lead to accelerated capacity fading. Voltage decay is

also a major issue associated with the material. We correlated this voltage drop to the second of two reactions occurring during discharge, which involves Mn and/or O reduction. The surface of Li-excess certainly exhibits a greater extent of Mn^{3+} in materials that have larger drops in voltage. It is not clear, however, whether Mn^{3+} originates from electrochemical redox within the electrode or from chemical reaction with the electrolyte. Determining what the case may be is important to more thoroughly identify what reactions contribute to the poor retention issues of Li-excess. Varying the composition of electrolyte and characterizing the surface of Li-excess using XPS, may be able to suggest how much of the reaction originates from interaction with electrolyte. Understanding the complex surface reactions occurring in this material is essential to improving its long-term stability.

Chapter 4 described how the phase propagation between $Li_4Ti_5O_{12}$ and $Li_7Ti_5O_{12}$ occurred during LTO's first cycle. The formation of an electronically conductive $Li_7Ti_5O_{12}$ percolation network was shown to provide an electronic pathway for non-conductive $Li_4Ti_5O_{12}$ to discharge, without the use of commonly employed conductive additives. A method that other researchers have employed to improve the initial conductivity of $Li_4Ti_5O_{12}$ is through the use of dopants. Computational results have suggested that introducing small amounts of transition metal ions ($< 5\%$) can reduce LTO's band gap. It would be worthwhile to know whether modifying LTO in this manner changes the way the conductive $Li_7Ti_5O_{12}$ phase is formed. Determining whether this is the case may provide insight into how a combination of particle morphologies and dopants may be used to completely remove conductive additive and binders from larger scale commercial electrodes.

References

1.   White, L. A. Energy And The Evolution Of Culture. *American Anthropologist* **1947,** *45* (3), 335-356.

2.   Dimitriev, O. P. Global Energy Consumption Rates: Where is the Limit? *Sustainable Energy* **2013,** *1* (1), 1-6.

3.   U.S. Energy Information Administration, I. S. A. *International Energy Outlook 2014*; DOE/EIA-0484(2014); EIA Analysis & Projections, September 9, 2014, 2014; pp 1-57.

4.   U.S. Energy Information Administration, I. S. A. International Energy Statistics. http://www.eia.gov/cfapps/ipdbproject/IEDIndex3.cfm?tid=44&pid=44&aid=2 (accessed August 20, 2015).

5.   Hubbert, M. K. Energy from Fossil Fuels. *Science* **1949,** *109* (2823), 103-109.

6.   Vesborg, P. C. K.; Jaramillo, T. F. Addressing the terawatt challenge: scalability in the supply of chemical elements for renewable energy. *RSC Advances* **2012,** *2* (21), 7933-7947.

7.   Dubal, D. P.; Ayyad, O.; Ruiz, V.; Gomez-Romero, P. Hybrid energy storage: the merging of battery and supercapacitor chemistries. *Chem. Soc. Rev.* **2015**.

8.   Diaz-Gonzalez, F.; Sumper, A.; Gomis-Bellmunt, O.; Villafiífila-Robles, R. A review of energy storage technologies for wind power applications. *Renewable and Sustainable Energy Reviews* **2012,** *16* (4), 2154-2171.

9.   Girishkumar, G.; McCloskey, B.; Luntz, A. C.; Swanson, S.; Wilcke, W. Lithium - Air Battery: Promise and Challenges. *Journal of Physical Chemistry Letters* **2010,** *1* (14), 2193-2203.

10.   Winter, M.; Brodd, R. J. What are batteries, fuel cells, and supercapacitors? (vol 104, pg 4245, 2003). *Chem. Rev. (Washington, DC, U. S.)* **2005,** *105* (3), 1021-1021.

11.   Song, M.-K.; Park, S.; Alamgir, F. M.; Cho, J.; Liu, M. Nanostructured electrodes for lithium-ion and lithium-air batteries: the latest developments, challenges, and perspectives. *Materials Science and Engineering: R: Reports* **2011,** *72* (11), 203-252.

12.   Tang, Y.; Zhang, Y.; Li, W.; Ma, B.; Chen, X. Rational material design for ultrafast rechargeable lithium-ion batteries. *Chem. Soc. Rev.* **2015**.

13.   Peterson, S. B.; Michalek, J. J. Cost-effectiveness of plug-in hybrid electric vehicle battery capacity and charging infrastructure investment for reducing US gasoline consumption. *Energy Policy* **2013,** *52*, 429-438.

14.   Hadjipaschalis, I.; Poullikkas, A.; Efthimiou, V. Overview of current and future energy storage technologies for electric power applications. *Renewable & Sustainable Energy Reviews* **2009,** *13* (6-7), 1513-1522.

15.   Soloveichik, G. L. Battery Technologies for Large-Scale Stationary Energy Storage. In *Annual Review of Chemical and Biomolecular Engineering, Vol 2*, Prausnitz, J. M., Ed. Annual Reviews: Palo Alto, 2011; Vol. 2, pp 503-527.

16.   Dunn, B.; Kamath, H.; Tarascon, J.-M. Electrical Energy Storage for the Grid: A Battery of Choices. *Science* **2011,** *334* (6058), 928-935.

17.   Alotto, P.; Guarnieri, M.; Moro, F. Redox flow batteries for the storage of renewable energy: A review. *Renewable and Sustainable Energy Reviews* **2014,** *29*, 325-335.

18.   Bailey, M. R.; Donne, S. W. Detection of Soluble Mn(III) Species during Cycling of Alkaline gamma-MnO2 and the Influence of Barium Hydroxide Inclusion. *J. Electrochem. Soc.* **2012,** *159* (12), A2010-A2015.

19.   Arico, A. S.; Bruce, P.; Scrosati, B.; Tarascon, J.-M.; van Schalkwijk, W. Nanostructured materials for advanced energy conversion and storage devices. *Nat Mater* **2005,** *4* (5), 366-377.

20.   Mizushima, K.; Jones, P. C.; Wiseman, P. J.; Goodenough, J. B. LixCoO2 (0<x<-1): A new cathode material for batteries of high energy density. *Mater. Res. Bull.* **1980,** *15* (6), 783-789.

21.   Yoshino, A. The Birth of the Lithium-Ion Battery. *Angewandte Chemie International Edition* **2012**, n/a-n/a.

22.   Steiger, J.; Richter, G.; Wenk, M.; Kramer, D.; Monig, R. Comparison of the growth of lithium filaments and dendrites under different conditions. *Electrochem. Commun.* **2015,** *50* (0), 11-14.

23.   Xu, K. Nonaqueous liquid electrolytes for lithium-based rechargeable batteries. *Chem. Rev. (Washington, DC, U. S.)* **2004,** *104* (10), 4303-4417.

24.   Owejan, J. E.; Owejan, J. P.; DeCaluwe, S. C.; Dura, J. A. Solid Electrolyte Interphase in Li-Ion Batteries: Evolving Structures Measured In situ by Neutron Reflectometry. *Chem. Mater.* **2012,** *24* (11), 2133-2140.

25.   de Leon, C. P.; Frias-Ferrer, A.; Gonzalez-Garcia, J.; Szanto, D. A.; Walsh, F. C. Redox flow cells for energy conversion. *J. Power Sources* **2006,** *160* (1), 716-732.

26.   Arora, P.; Zhang, Z. Battery Separators. *Chem. Rev. (Washington, DC, U. S.)* **2004,** *104* (10), 4419-4462.

27.   Zhang, C. P.; Sharkh, S. M.; Li, X.; Walsh, F. C.; Zhang, C. N.; Jiang, J. C. The performance of a soluble lead-acid flow battery and its comparison to a static lead-acid battery. *Energy Conversion and Management* **2011,** *52* (12), 3391-3398.

28.   Gernon, M. D.; Wu, M.; Buszta, T.; Janney, P. Environmental benefits of methanesulfonic acid: Comparative properties and advantages. *Green Chem.* **1999,** *1* (3), 127-140.

29.   Hazza, A.; Pletcher, D.; Wills, R. A novel flow battery: A lead acid battery based on an electrolyte with soluble lead(II) - Part I. Preliminary studies. *Phys. Chem. Chem. Phys.* **2004,** *6* (8), 1773-1778.

30.   Pletcher, D.; Wills, R. A novel flow battery: A lead acid battery based on an electrolyte with soluble lead(II) - Part II. Flow cell studies. *Phys. Chem. Chem. Phys.* **2004,** *6* (8), 1779-1785.

31.   Hazza, A.; Pletcher, D.; Wills, R. A novel flow battery - A lead acid battery based on an electrolyte with soluble lead(II) - IV. The influence of additives. *J. Power Sources* **2005,** *149*, 103-111.

32.   Pletcher, D.; Wills, R. A novel flow battery - A lead acid battery based on an electrolyte with soluble lead(II) - III. The influence of conditions on battery performance. *J. Power Sources* **2005,** *149*, 96-102.

33.   Pletcher, D.; Zhou, H.; Kear, G.; Low, C. T. J.; Walsh, F. C.; Wills, R. G. A. A novel flow battery - A lead-acid battery based on an electrolyte with soluble lead(II) V. Studies of the lead negative electrode. *J. Power Sources* **2008,** *180* (1), 621-629.

34.   Pletcher, D.; Zhou, H.; Kear, G.; Low, C. T. J.; Walsh, F. C.; Wills, R. G. A. A novel flow battery - A lead-acid battery based on an electrolyte with soluble lead(II) Part VI. Studies of the lead dioxide positive electrode. *J. Power Sources* **2008,** *180* (1), 630-634.

35.   Li, X. H.; Pletcher, D.; Walsh, F. C. A novel flow battery: A lead acid battery based on an electrolyte with soluble lead(II) Part VII. Further studies of the lead dioxide positive electrode. *Electrochim. Acta* **2009,** *54* (20), 4688-4695.

36.   Collins, J.; Kear, G.; Li, X. H.; Low, C. T. J.; Pletcher, D.; Tangirala, R.; Stratton-Campbell, D.; Walsh, F. C.; Zhang, C. P. A novel flow battery: A lead acid battery based on an electrolyte with soluble lead(II) Part VIII. The cycling of a 10 cm x 10 cm flow cell. *J. Power Sources* **2010,** *195* (6), 1731-1738.

37.   Collins, J.; Li, X. H.; Pletcher, D.; Tangirala, R.; Stratton-Campbell, D.; Walsh, F. C.; Zhang, C. P. A novel flow battery: A lead acid battery based on an electrolyte with soluble lead(II). Part IX: Electrode and electrolyte conditioning with hydrogen peroxide. *J. Power Sources* **2010,** *195* (9), 2975-2978.

38.   Wills, R. G. A.; Collins, J.; Stratton-Campbell, D.; Low, C. T. J.; Pletcher, D.; Walsh, F. C. Developments in the soluble lead-acid flow battery. *J. Appl. Electrochem.* **2010,** *40* (5), 955-965.

39.   Skyllas-Kazacos, M.; Chakrabarti, M. H.; Hajimolana, S. A.; Mjalli, F. S.; Saleem, M. Progress in Flow Battery Research and Development. *J. Electrochem. Soc.* **2011,** *158* (8), R55-R79.

40.   Velichenko, A. B.; Amadelli, R.; Gruzdeva, E. V.; Luk'yanenko, T. V.; Danilov, F. I. Electrodeposition of lead dioxide from methanesulfonate solutions. *J. Power Sources* **2009,** *191* (1), 103-110.

41.   Oury, A.; Kirchev, A.; Bultel, Y. Oxygen evolution on alpha-lead dioxide electrodes in methanesulfonic acid. *Electrochim. Acta* **2012,** *63* (0), 28-36.

42.   Oury, A.; Kirchev, A.; Bultel, Y.; Chainet, E. PbO2/Pb2+ cycling in methanesulfonic acid and mechanisms associated for soluble lead-acid flow battery applications. *Electrochim. Acta* **2012,** *71*, 140-149.

43.   Ruetschi, P. Influence of Crystal Structure and Interparticle Contact on the Capacity of PbO2 Electrodes *J. Electrochem. Soc.* **1992,** *139* (5), 1347-1351.

44.   Shah, A. A.; Li, X.; Wills, R. G. A.; Walsh, F. C. A Mathematical Model for the Soluble Lead-Acid Flow Battery. *J. Electrochem. Soc.* **2010,** *157* (5), A589-A599.

45.   Sires, I.; Low, C. T. J.; Ponce-de-Leon, C.; Walsh, F. C. The characterisation of PbO2-coated electrodes prepared from aqueous methanesulfonic acid under controlled deposition conditions. *Electrochim. Acta* **2010,** *55* (6), 2163-2172.

46.   Munichandraiah, N. Physicochemical Properties of Electrodeposited Beta-Lead Dioxide - Effect of Deposition Current Density. *J. Appl. Electrochem.* **1992,** *22* (9), 825-829.

47.   Larson, A. C.; Dreele, R. B. General Structure Analysis System (GSAS). Los Alamos National Laboratory 2000; pp 86-748.

48.   Peng, H. Y.; Chen, H. Y.; Li, W. S.; Hu, S. J.; Li, H.; Nan, J. M.; Xu, Z. H. A study on the reversibility of Pb(II)/PbO2 conversion for the application of flow liquid battery. *J. Power Sources* **2007,** *168* (1), 105-109.

49.   Oury, A.; Kirchev, A.; Bultel, Y. Potential Response of Lead Dioxide/Lead(II) Galvanostatic Cycling in Methanesulfonic Acid: A Morphologico-Kinetics Interpretation. *J. Electrochem. Soc.* **2013,** *160* (1), A148-A154.

50.	Milchev, A.; Kruijt, W. S.; Sluyters-Rehbach, M.; Sluyters, J. H. Distribution of the nucleation rate in the vicinity of a growing spherical cluster: Part 1. Theory and simulation results. *J. Electroanal. Chem.* **1993,** *362* ((1-2)), 21-31.

51.	Paunovic, M.; Schlesinger, M. *Fundamentals of Electrochemical Deposition, 2nd Edition*. Wiley-Interscience: New Jersey, 2006.

52.	Seiter, H.; Fischer, H.; Albert, L. Electrochemical and morphological studies on the mechanism of electrocrystallization far from the initial state. *Electrochim. Acta* **1960,** *2* (Copyright (C) 2012 American Chemical Society (ACS). All Rights Reserved.), 97-120.

53.	Wang, H.; Brandl, D. W.; Le, F.; Nordlander, P.; Halas, N. J. Nanorice: A Hybrid Plasmonic Nanostructure. *Nano Lett.* **2006,** *6* (4), 827-832.

54.	Bard, A. J.; Parsons, R.; Jordan, J. *Standard Potentials in Aqueous Solutions*. Marcel Dekker: New York, 1985.

55.	Chen, B. M.; Guo, Z. C.; Yang, X. W.; Cao, Y. D. Morphology of alpha-lead dioxide electrodeposited on aluminum substrate electrode. *Transactions of Nonferrous Metals Society of China* **2010,** *20* (1), 97-103.

56.	Fergus, J. W. Recent developments in cathode materials for lithium ion batteries. *J. Power Sources* **2010,** *195* (4), 939-954.

57.	Ohzuku, T.; Nagayama, M.; Tsuji, K.; Ariyoshi, K. High-capacity lithium insertion materials of lithium nickel manganese oxides for advanced lithium-ion batteries: toward rechargeable capacity more than 300 mAh g^{-1}. *J. Mater. Chem.* **2011,** *21* (27), 10179-10188.

58.	Song, B.; Liu, Z.; Lai, M. O.; Lu, L. Structural evolution and the capacity fade mechanism upon long-term cycling in Li-rich cathode material. *Phys. Chem. Chem. Phys.* **2012,** *14* (37), 12875-12883.

59.	van Bommel, A.; Krause, L. J.; Dahn, J. R. Investigation of the Irreversible Capacity Loss in the Lithium-Rich Oxide $Li[Li_{1/5}Ni_{1/5}Mn_{3/5}]O_2$. *J. Electrochem. Soc.* **2011,** *158* (6), A731-A735.

60.   Ito, A.; Li, D.; Ohsawa, Y.; Sato, Y. A new approach to improve the high-voltage cyclic performance of Li-rich layered cathode material by electrochemical pre-treatment. *J. Power Sources* **2008,** *183* (1), 344-346.

61.   Mohanty, D.; Kalnaus, S.; Meisner, R. A.; Rhodes, K. J.; Li, J.; Payzant, E. A.; Wood Iii, D. L.; Daniel, C. Structural Transformation of a Lithium-rich $Li_{1.2}Co_{0.1}Mn_{0.55}Ni_{0.15}O_2$ Cathode During High Voltage Cycling Resolved by In Situ X-ray Diffraction. *J. Power Sources* **2013,** *229* (0), 239-248.

62.   Bettge, M.; Li, Y.; Gallagher, K.; Zhu, Y.; Wu, Q. L.; Lu, W. Q.; Bloom, I.; Abraham, D. P. Voltage Fade of Layered Oxides: Its Measurement and Impact on Energy Density. *J. Electrochem. Soc.* **2013,** *160* (11), A2046-A2055.

63.   Lu, Z. H.; MacNeil, D. D.; Dahn, J. R. Layered Cathode Materials $LiNi_xLi_{(1/3-2x/3)}Mn_{(2/3-x/3)}O_2$ for Lithium-ion Batteries. *Electrochemical and Solid State Letters* **2001,** *4* (11), A191-A194.

64.   Lu, Z. H.; Beaulieu, L. Y.; Donaberger, R. A.; Thomas, C. L.; Dahn, J. R. Synthesis, Structure, and Electrochemical Behavior of $LiNi_xLi_{1/3-2x/3}Mn_{2/3-x/3}O_2$. *J. Electrochem. Soc.* **2002,** *149* (6), A778-A791.

65.   Thackeray, M. M.; Kang, S. H.; Johnson, C. S.; Vaughey, J. T.; Benedek, R.; Hackney, S. A. Li_2MnO_3-stabilized $LiMO_2$ (M = Mn, Ni, Co) electrodes for lithium-ion batteries. *J. Mater. Chem.* **2007,** *17* (30), 3112-3125.

66.   Yu, H.; Kim, H.; Wang, Y.; He, P.; Asakura, D.; Nakamura, Y.; Zhou, H. High-energy 'composite' layered manganese-rich cathode materials via controlling Li_2MnO_3 phase activation for lithium-ion batteries. *Phys. Chem. Chem. Phys.* **2012,** *14* (18), 6584-6595.

67.   Jarvis, K. A.; Deng, Z.; Allard, L. F.; Manthiram, A.; Ferreira, P. J. Atomic Structure of a Lithium-Rich Layered Oxide Material for Lithium-Ion Batteries: Evidence of a Solid Solution. *Chem. Mater.* **2011,** *23* (16), 3614-3621.

68.   Park, Y. J.; Kim, M. G.; Hong, Y.-S.; Wu, X.; Ryu, K. S.; Chang, S. H. Electrochemical behavior of Li intercalation processes into a $Li[Ni_xLi_{(1/3-2x/3)}Mn_{(2/3-x/3)}]O_2$ cathode. *Solid State Commun.* **2003,** *127* (7), 509-514.

69.   Koga, H.; Croguennec, L.; Ménétrier, M.; Mannessiez, P.; Weill, F.; Delmas, C.; Belin, S. Operando X-ray Absorption Study of the Redox Processes Involved upon Cycling of the Li-Rich Layered Oxide $Li_{1.20}Mn_{0.54}Co_{0.13}Ni_{0.13}O_2$ in Li Ion Batteries. *The Journal of Physical Chemistry C* **2014,** *118* (11), 5700-5709.

70.   Yabuuchi, N.; Yoshii, K.; Myung, S.-T.; Nakai, I.; Komaba, S. Detailed Studies of a High-Capacity Electrode Material for Rechargeable Batteries, Li_2MnO_3-$LiCo_{1/3}Ni_{1/3}Mn_{1/3}O_2$. *J. Am. Chem. Soc.* **2011,** *133* (12), 4404-4419.

71.   Yu, D. Y. W.; Yanagida, K. Structural Analysis of Li_2MnO_3 and Related Li-Mn-O Materials. *J. Electrochem. Soc.* **2011,** *158* (9), A1015-A1022.

72.   Ito, A.; Sato, Y.; Sanada, T.; Hatano, M.; Horie, H.; Ohsawa, Y. In situ X-ray absorption spectroscopic study of Li-rich layered cathode material $Li[Ni_{0.17}Li_{0.2}Co_{0.07}Mn_{0.56}]O_2$. *J. Power Sources* **2011,** *196* (16), 6828-6834.

73.   Carroll, K. J.; Qian, D.; Fell, C.; Calvin, S.; Veith, G. M.; Chi, M.; Baggetto, L.; Meng, Y. S. Probing the electrode/electrolyte interface in the lithium excess layered oxide $Li_{1.2}Ni_{0.2}Mn_{0.6}O_2$. *Phys. Chem. Chem. Phys.* **2013,** *15* (26), 11128-11138.

74.   Fell, C. R.; Carroll, K. J.; Chi, M. F.; Meng, Y. S. Synthesis-Structure-Property Relations in Layered, "Li-excess" Oxides Electrode Materials Li $Li_{1/3-2x/3}Ni_xMn_{2/3-x/3}$ O_2 (x=1/3, 1/4, and 1/5). *J. Electrochem. Soc.* **2010,** *157* (11), A1202-A1211.

75.   Armstrong, A. R.; Holzapfel, M.; Novak, P.; Johnson, C. S.; Kang, S. H.; Thackeray, M. M.; Bruce, P. G. Demonstrating oxygen loss and associated structural reorganization in the lithium battery cathode $LiNi_{0.2}Li_{0.2}Mn_{0.6}O_2$. *J. Am. Chem. Soc.* **2006,** *128* (26), 8694-8698.

76.   Hong, J.; Lim, H.-D.; Lee, M.; Kim, S.-W.; Kim, H.; Oh, S.-T.; Chung, G.-C.; Kang, K. Critical Role of Oxygen Evolved from Layered Li-Excess Metal Oxides in Lithium Rechargeable Batteries. *Chem. Mater.* **2012,** *24* (14), 2692-2697.

77.   Wang, C.-C.; Jarvis, K. A.; Ferreira, P. J.; Manthiram, A. Effect of Synthesis Conditions on the First Charge and Reversible Capacities of Lithium-Rich Layered Oxide Cathodes. *Chem. Mater.* **2013,** *25* (15), 3267-3275.

78.   Park, S. H.; Kang, S. H.; Belharouak, I.; Sun, Y. K.; Amine, K. Physical and electrochemical properties of spherical $Li_{1+x}(Ni_{1/3}Co_{1/3}Mn_{1/3})O_2$ cathode materials. *J. Power Sources* **2008,** *177* (1), 177-183.

79.   van Bommel, A.; Dahn, J. R. Analysis of the Growth Mechanism of Coprecipitated Spherical and Dense Nickel, Manganese, and Cobalt-Containing Hydroxides in the Presence of Aqueous Ammonia. *Chem. Mater.* **2009,** *21* (8), 1500-1503.

80.   Liu, H.; Wu, Y. P.; Rahm, E.; Holze, R.; Wu, H. Q. Cathode materials for lithium ion batteries prepared by sol-gel methods. *J. Solid State Electrochem.* **2004,** *8* (7), 450-466.

81.   Zhang, S.; Deng, C.; Fu, B. L.; Yang, S. Y.; Ma, L. Synthetic optimization of spherical $LiNi_{1/3}Mn_{1/3}Co_{1/3}O_2$ prepared by a carbonate co-precipitation method. *Powder Technol.* **2010,** *198* (3), 373-380.

82.   Wang, T.; Liu, Z.-H.; Fan, L.; Han, Y.; Tang, X. Synthesis optimization of $Li_{1+x}[Mn_{0.45}Co_{0.40}Ni_{0.15}]O_2$ with different spherical sizes via co-precipitation. *Powder Technol.* **2008,** *187* (2), 124-129.

83.   Carvajal, J. FULLPROF: A Program for Rietveld Refinement and Pattern Matching Analysis. *Abstracts of the Satellite Meeting on Powder Diffraction of the XV Congress of the IUCr* **1990**.

84.   Wang, J.; Yao, X.; Zhou, X.; Liu, Z. Synthesis and electrochemical properties of layered lithium transition metal oxides. *J. Mater. Chem.* **2011,** *21* (8), 2544-2549.

85.   Boulineau, A.; Simonin, L.; Colin, J.-F.; Canévet, E.; Daniel, L.; Patoux, S. Evolutions of $Li_{1.2}Mn_{0.61}Ni_{0.18}Mg_{0.01}O_2$ during the Initial Charge/Discharge Cycle Studied by Advanced Electron Microscopy. *Chem. Mater.* **2012,** *24* (18), 3558-3566.

86.   Yu, H.; Zhou, H. High-Energy Cathode Materials Li_2MnO_3-$LiMO_2$) for Lithium-Ion Batteries. *The Journal of Physical Chemistry Letters* **2013,** *4* (8), 1268-1280.

87.   Goodenough, J. B.; Kim, Y. Challenges for Rechargeable Li Batteries. *Chem. Mater.* **2009,** *22* (3), 587-603.

88.   Dedryvère, R.; Gireaud, L.; Grugeon, S.; Laruelle, S.; Tarascon, J. M.; Gonbeau, D. Characterization of lithium alkyl carbonates by X-ray photoelectron spectroscopy: Experimental and theoretical study. *J. Phys. Chem. B* **2005,** *109* (33), 15868-15875.

89.   Philippe, B.; Dedryvère, R.; Gorgoi, M.; Rensmo, H.; Gonbeau, D.; Edström, K. Role of the $LiPF_6$ Salt for the Long-Term Stability of Silicon Electrodes in Li-Ion Batteries - A Photoelectron Spectroscopy Study. *Chem. Mater.* **2013,** *25* (3), 394-404.

90.   Quinlan, R. A.; Lu, Y.-C.; Shao-Horn, Y.; Mansour, A. N. XPS Studies of Surface Chemistry Changes of $LiNi_{0.5}Mn_{0.5}O_2$ Electrodes during High-Voltage Cycling. *J. Electrochem. Soc.* **2013,** *160* (4), A669-A677.

91.   Galakhov, V. R.; Demeter, M.; Bartkowski, S.; Neumann, M.; Ovechkina, N. A.; Kurmaev, E. Z.; Lobachevskaya, N. I.; Mukovskii, Y. M.; Mitchell, J.; Ederer, D. L. Mn 3s exchange splitting in mixed-valence manganites. *Phys. Rev. B* **2002,** *65* (11), 113102.

92.   Carabineiro, S. A. C.; Bastos, S. S. T.; Orfao, J. J. M.; Pereira, M. F. R.; Delgado, J. J.; Figueiredo, J. L. Carbon Monoxide Oxidation Catalysed by Exotemplated Manganese Oxides. *Catal. Lett.* **2010,** *134* (3-4), 217-227.

93.   Allen, G. C.; Harris, S. J.; Jutson, J. A.; Dyke, J. M. A Study of a Number of Mixed Transition-Metal Oxide Spinels Using X-ray Photoelectron Spectroscopy. *Appl. Surf. Sci.* **1989,** *37* (1), 111-134.

94.   Song, J. Y.; Wang, Y. Y.; Wan, C. C. Review of gel-type polymer electrolytes for lithium-ion batteries. *J. Power Sources* **1999,** *77* (2), 183-197.

95.   Cerrato, J. M.; Hochella, M. F.; Knocke, W. R.; Dietrich, A. M.; Cromer, T. F. Use of XPS to Identify the Oxidation State of Mn in Solid Surfaces of Filtration Media Oxide Samples from Drinking Water Treatment Plants. *Environ. Sci. Technol.* **2010,** *44* (15), 5881-5886.

96.   Galakhov, V. R.; Uhlenbrok, S.; Bartkowski, S.; Postinkov, A. V.; Neumann, M.; Finkelstein, L. D.; Kurmaev, E. Z.; Samokhvalov, A. A.; Leonyuk, L. I. X-ray Photoelectron 3s Spectra of Transition Metal Oxides. **1999**.

97.   Tran, N.; Croguennec, L.; Ménétrier, M.; Weill, F.; Biensan, P.; Jordy, C.; Delmas, C. Mechanisms Associated with the "Plateau" Observed at High Voltage for the

Overlithiated $Li_{1.12}(Ni_{0.425}Mn_{0.425}Co_{0.15})_{0.88}O_2$ System. *Chem. Mater.* **2008,** *20* (15), 4815-4825.

98.　　Xu, B.; Fell, C. R.; Chi, M. F.; Meng, Y. S. Identifying surface structural changes in layered Li-excess nickel manganese oxides in high voltage lithium ion batteries: A joint experimental and theoretical study. *Energy Environ. Sci.* **2011,** *4* (6), 2223-2233.

99.　　Fell, C. R.; Chi, M.; Meng, Y. S.; Jones, J. L. In situ X-ray diffraction study of the lithium excess layered oxide compound $Li[Li_{0.2}Ni_{0.2}Mn_{0.6}]O_2$ during electrochemical cycling. *Solid State Ionics* **2012,** *207* (Copyright (C) 2012 American Chemical Society (ACS). All Rights Reserved.), 44-49.

100.　Fell, C. R.; Qian, D.; Carroll, K. J.; Chi, M.; Jones, J. L.; Meng, Y. S. Correlation Between Oxygen Vacancy, Microstrain, and Cation Distribution in Lithium-Excess Layered Oxides During the First Electrochemical Cycle. *Chem. Mater.* **2013,** *25* (9), 1621-1629.

101.　Freunberger, S. A.; Chen, Y.; Peng, Z.; Griffin, J. M.; Hardwick, L. J.; Bardé, F.; Novák, P.; Bruce, P. G. Reactions in the Rechargeable Lithium-O_2 Battery with Alkyl Carbonate Electrolytes. *J. Am. Chem. Soc.* **2011,** *133* (20), 8040-8047.

102.　Koga, H.; Croguennec, L.; Ménétrier, M.; Douhil, K.; Belin, S.; Bourgeois, L.; Suard, E.; Weill, F.; Delmas, C. Reversible Oxygen Participation to the Redox Processes Revealed for $Li_{1.20}Mn_{0.54}Co_{0.13}Ni_{0.13}O_2$. *J. Electrochem. Soc.* **2013,** *160* (6), A786-A792.

103.　Koga, H.; Croguennec, L.; Ménétrier, M.; Mannessiez, P.; Weill, F.; Delmas, C. Different oxygen redox participation for bulk and surface: A possible global explanation for the cycling mechanism of $Li_{1.20}Mn_{0.54}Co_{0.13}Ni_{0.13}O_2$. *J. Power Sources* **2013,** *236* (0), 250-258.

104.　Rana, J.; Stan, M.; Kloepsch, R.; Li, J.; Schumacher, G.; Welter, E.; Zizak, I.; Banhart, J.; Winter, M. Structural Changes in Li_2MnO_3 Cathode Material for Li-Ion Batteries. *Advanced Energy Materials* **2014,** *4* (5), n/a-n/a.

105.　Park, S.-H.; Sato, Y.; Kim, J.-K.; Lee, Y.-S. Powder property and electrochemical characterization of Li_2MnO_3 material. *Mater. Chem. Phys.* **2007,** *102* (2ΓÇô3), 225-230.

106.　Francis Amalraj, S.; Markovsky, B.; Sharon, D.; Talianker, M.; Zinigrad, E.; Persky, R.; Haik, O.; Grinblat, J.; Lampert, J.; Schulz-Dobrick, M.; Garsuch, A.; Burlaka,

L.; Aurbach, D. Study of the electrochemical behavior of the "inactive" Li_2MnO_3. *Electrochim. Acta* **2012,** *78* (0), 32-39.

107. Lim, J.; Moon, J.; Gim, J.; Kim, S.; Kim, K.; Song, J.; Kang, J.; Im, W. B.; Kim, J. Fully activated Li_2MnO_3 nanoparticles by oxidation reaction. *J. Mater. Chem.* **2012,** *22* (23), 11772-11777.

108. Yu, D. Y. W.; Yanagida, K.; Kato, Y.; Nakamura, H. Electrochemical Activities in Li_2MnO_3. *J. Electrochem. Soc.* **2009,** *156* (6), A417-A424.

109. Park, C.-M.; Kim, J.-H.; Kim, H.; Sohn, H.-J. Li-alloy based anode materials for Li secondary batteries. *Chem. Soc. Rev.* **2010,** *39* (8), 3115-3141.

110. Zhu, G. N.; Wang, Y. G.; Xia, Y. Y. Ti-based compounds as anode materials for Li-ion batteries. *Energy Environ. Sci.* **2012,** *5* (5), 6652-6667.

111. Oumellal, Y.; Delpuech, N.; Mazouzi, D.; Dupre, N.; Gaubicher, J.; Moreau, P.; Soudan, P.; Lestriez, B.; Guyomard, D. The failure mechanism of nano-sized Si-based negative electrodes for lithium ion batteries. *J. Mater. Chem.* **2011,** *21* (17), 6201-6208.

112. Ohzuku, T.; Ueda, A.; Yamamoto, N. Zero-Strain Insertion Material of Li[Li1/3Ti5/3]O4 for Rechargeable Lithium Cells. *J. Electrochem. Soc.* **1995,** *142* (5), 1431-1435.

113. Takami, N.; Hoshina, K.; Inagaki, H. Lithium Diffusion in Li4/3Ti5/3O4 Particles during Insertion and Extraction. *J. Electrochem. Soc.* **2011,** *158* (6), A725-A730.

114. Chen, C. H.; Vaughey, J. T.; Jansen, A. N.; Dees, D. W.; Kahaian, A. J.; Goacher, T.; Thackeray, M. M. Studies of Mg-Substituted Li4-xMgxTi5O12 Spinel Electrodes (0≤x≤1) for Lithium Batteries. *J. Electrochem. Soc.* **2001,** *148* (1), A102-A104.

115. Edwards, P. P.; Egdell, R. G.; Fragala, I.; Goodenough, J. B.; Harrison, M. R.; Orchard, A. F.; Scott, E. G. A study of the spinel materials LiTi2O4 and Li43Ti53O4 by photoelectron spectroscopy. *J. Solid State Chem.* **1984,** *54* (2), 127-135.

116. Kostlánová, T.; Dedecek, J.; Krtil, P. The effect of the inner particle structure on the electronic structure of the nano-crystalline Li-Ti-O spinels. *Electrochim. Acta* **2007,** *52* (5), 1847-1856.

117.   Luo, H.; Shen, L.; Rui, K.; Li, H.; Zhang, X. Carbon coated Li4Ti5O12 nanorods as superior anode material for high rate lithium ion batteries. *J. Alloys Compd.* **2013,** *572* (0), 37-42.

118.   Qi, L.; Chen, S.; Xin, Y.; Zhou, Y.; Ma, Y.; Zhou, H. Self-supported Li4Ti5O12 nanosheet arrays for lithium ion batteries with excellent rate capability and ultralong cycle life. *Energy Environ. Sci.* **2013**.

119.   Zhang, Q.; Verde, M. G.; Seo, J. K.; Li, X.; Meng, Y. S. Structural and electrochemical properties of Gd-doped Li4Ti5O12 as anode material with improved rate capability for lithium-ion batteries. *J. Power Sources* **2015,** *280* (0), 355-362.

120.   Liu, J.; Song, K.; van Aken, P. A.; Maier, J.; Yu, Y. Self-Supported Li4Ti5O12-C Nanotube Arrays as High-Rate and Long-Life Anode Materials for Flexible Li-Ion Batteries. *Nano Lett.* **2014,** *14* (5), 2597-2603.

121.   Li, N.; Zhou, G.; Li, F.; Wen, L.; Cheng, H.-M. A Self-Standing and Flexible Electrode of Li4Ti5O12 Nanosheets with a N-Doped Carbon Coating for High Rate Lithium Ion Batteries. *Adv. Funct. Mater.* **2013,** *23* (43), 5429-5435.

122.   Song, M.-S.; Benayad, A.; Choi, Y.-M.; Park, K.-S. Does Li4Ti5O12 need carbon in lithium ion batteries? Carbon-free electrode with exceptionally high electrode capacity. *Chem. Commun. (Cambridge, U. K.)* **2012,** *48* (4), 516-518.

123.   Kim, C.; Norberg, N. S.; Alexander, C. T.; Kostecki, R.; Cabana, J. Mechanism of Phase Propagation During Lithiation in Carbon-Free Li4Ti5O12 Battery Electrodes. *Adv. Funct. Mater.* **2013,** *23* (9), 1214-1222.

124.   Young, D.; Ransil, A.; Amin, R.; Li, Z.; Chiang, Y.-M. Electronic Conductivity in the Li4/3Ti5/3O4–Li7/3Ti5/3O4 System and Variation with State-of-Charge as a Li Battery Anode. *Advanced Energy Materials* **2013**, n/a-n/a.

125.   Scharner, S.; Weppner, W.; Schmid-Beurmann, P. Evidence of two-phase formation upon lithium insertion into the Li1.33Ti1.67O4 spinel. *J. Electrochem. Soc.* **1999,** *146* (3), 857-861.

126.   Kanamura, K.; Umegaki, T.; Naito, H.; Takehara, Z.; Yao, T. Structural and electrochemical characteristics of Li-4/Ti-3(5)/O-3(4) as an anode material for rechargeable lithium batteries. *J. Appl. Electrochem.* **2001,** *31* (1), 73-78.

127. Kresse, G.; Furthmüller, J. Efficient iterative schemes for ab initio total-energy calculations using a plane-wave basis set. *Phys. Rev. B* **1996,** *54* (16), 11169-11186.

128. Perdew, J. P.; Burke, K.; Ernzerhof, M. Generalized Gradient Approximation Made Simple [Phys. Rev. Lett. 77, 3865 (1996)]. *Phys. Rev. Lett.* **1997,** *78* (7), 1396-1396.

129. Blöchl, P. E. Projector augmented-wave method. *Phys. Rev. B* **1994,** *50* (24), 17953-17979.

130. Kresse, G.; Joubert, D. From ultrasoft pseudopotentials to the projector augmented-wave method. *Phys. Rev. B* **1999,** *59* (3), 1758-1775.

131. Horcas, I.; Fernandez, R.; Gpmez-Rodriguez, J. M.; Colchero, J.; Gomez-Herrero, J.; Baro, A. M. WSXM: A software for scanning probe microscopy and a tool for nanotechnology. *Rev. Sci. Instrum.* **2007,** *78* (1), 013705.

132. Song, H.; Yun, S.-W.; Chun, H.-H.; Kim, M.-G.; Chung, K. Y.; Kim, H. S.; Cho, B.-W.; Kim, Y.-T. Anomalous decrease in structural disorder due to charge redistribution in Cr-doped Li4Ti5O12 negative-electrode materials for high-rate Li-ion batteries. *Energy Environ. Sci.* **2012,** *5* (12), 9903-9913.

133. Tsai, P.-c.; Hsu, W.-D.; Lin, S.-k. Atomistic Structure and Ab Initio Electrochemical Properties of Li4Ti5O12 Defect Spinel for Li Ion Batteries. *J. Electrochem. Soc.* **2014,** *161* (3), A439-A444.

134. Guo, X.; Wang, C.; Chen, M.; Wang, J.; Zheng, J. Carbon coating of Li4Ti5O12 using amphiphilic carbonaceous material for improvement of lithium-ion battery performance. *J. Power Sources* **2012,** *214* (0), 107-112.

135. Ding, Z.; Zhao, L.; Suo, L.; Jiao, Y.; Meng, S.; Hu, Y.-S.; Wang, Z.; Chen, L. Towards understanding the effects of carbon and nitrogen-doped carbon coating on the electrochemical performance of Li4Ti5O12 in lithium ion batteries: a combined experimental and theoretical study. *Phys. Chem. Chem. Phys.* **2011,** *13* (33), 15127-15133.

136. Zhang, B.; Huang, Z.-D.; Oh, S. W.; Kim, J.-K. Improved rate capability of carbon coated Li3.9Sn0.1Ti5O12 porous electrodes for Li-ion batteries. *J. Power Sources* **2011,** *196* (24), 10692-10697.

137.   Nakayama, M.; Ishida, Y.; Ikuta, H.; Wakihara, M. Mixed conduction for the spinel type (1-x)Li4/3Ti5/3O4-xLiCrTiO4 system. *Solid State Ionics* **1999,** *117* (3ГÇô4), 265-271.

138.   Deng, J.; Lu, Z.; Belharouak, I.; Amine, K.; Chung, C. Y. Preparation and electrochemical properties of Li4Ti5O12 thin film electrodes by pulsed laser deposition. *J. Power Sources* **2009,** *193* (2), 816-821.

139.   Cai, R.; Jiang, S.; Yu, X.; Zhao, B.; Wang, H.; Shao, Z. A novel method to enhance rate performance of an Al-doped Li4Ti5O12 electrode by post-synthesis treatment in liquid formaldehyde at room temperature. *J. Mater. Chem.* **2012,** *22* (16), 8013-8021.

140.   Bender, H.; Chen, W. D.; Portillo, J.; Van den Hove, L.; Vandervorst, W. AES and XPS analysis of the interaction of Ti with Si and SiO2 during RTA. *Appl. Surf. Sci.* **1989,** *38* (1-4), 37-47.

141.   Bertoncello, R.; Casagrande, A.; Casarin, M.; Glisenti, A.; Lanzoni, E.; Mirenghi, L.; Tondello, E. Tin, Tic and Ti(C, N) film characterization and its relationship to tribological behaviour. *Surf. Interface Anal.* **1992,** *18* (7), 525-531.

142.   Shi, Y.; Wen, L.; Li, F.; Cheng, H.-M. Nanosized Li4Ti5O12/graphene hybrid materials with low polarization for high rate lithium ion batteries. *J. Power Sources* **2011,** *196* (20), 8610-8617.

143.   Appapillai, A. T.; Mansour, A. N.; Cho, J.; Shao-Horn, Y. Microstructure of LiCoO2 with and without "AlPO4" Nanoparticle Coating: Combined STEM and XPS Studies. *Chem. Mater.* **2007,** *19* (23), 5748-5757.

144.   He, Y. B.; Li, B. H.; Liu, M.; Zhang, C.; Lv, W.; Yang, C.; Li, J.; Du, H. D.; Zhang, B. A.; Yang, Q. H.; Kim, J. K.; Kang, F. Y. Gassing in Li4Ti5O12-based batteries and its remedy. *Scientific Reports* **2012,** *2*.

145.   He, Y.-B.; Liu, M.; Huang, Z.-D.; Zhang, B.; Yu, Y.; Li, B.; Kang, F.; Kim, J.-K. Effect of solid electrolyte interface (SEI) film on cyclic performance of Li4Ti5O12 anodes for Li ion batteries. *J. Power Sources* **2013,** *239* (0), 269-276.

146.   Kitta, M.; Akita, T.; Maeda, Y.; Kohyama, M. Study of Surface Reaction of Spinel Li4Ti5O12 during the First Lithium Insertion and Extraction Processes Using

Atomic Force Microscopy and Analytical Transmission Electron Microscopy. *Langmuir* **2012**.